CORROSION BEHAVIOUR OF AZ31 MAGNESIUM ALLOY IN HIGHLY ALKALINE ENVIRONMENTS

by

Somi Doja

B. Tech., Jamia Millia Islamia University, 2015

A THESIS SUBMITTED IN PARTIAL FULFILLMENT OF
THE REQUIREMENTS FOR THE DEGREE OF

MASTER OF APPLIED SCIENCE

in

THE COLLEGE OF GRADUATE STUDIES

(Mechanical Engineering)

THE UNIVERSITY OF BRITISH COLUMBIA
(Okanagan)

April 2017

The undersigned certify that they have read, and recommend to the College of Graduate Studies for acceptance, a thesis entitled:

CORROSION BEHAVIOUR OF AZ31

MAGNESIUM ALLOY IN HIGHLY ALKALINE ENVIRONMENTS

submitted by Somi Doja in partial fulfilment of the requirements of the degree of Master of Applied Science.

Lukas Bichler

Supervisor, Professor (please print name and faculty/school above the line)

Keekyoung Kim

Supervisory Committee Member, Professor (please print name and faculty/school in the line above)

Ray Taheri

Supervisory Committee Member, Professor (please print name and faculty/school in the line above)

Thomas Johnson

University Examiner, Professor (please print name and faculty/school in the line above)

Chen Feng

External Examiner, Professor (please print name and university in the line above)

28-04-2017

(Date Submitted to Grad Studies)

Additional Committee Members include:

(please print name and faculty/school in the line above)

(please print name and faculty/school in the line above)

Abstract

Magnesium (Mg) and its alloys are known for their high chemical reactivity. This property often poses issues related to undesirable corrosion, or degradation of exposed surfaces. The chemical reactivity of Mg can be also exploited, and as a result Mg alloys often find use as anode materials for fuel cells. However, due to a long term immersion of the anodes in highly alkaline environments, the problem of corrosion remains and needs to be evaluated. Therefore, in this research, the corrosion behavior of a commercially available magnesium alloy AZ31 in 45 wt% potassium hydroxide (KOH), a common electrolyte for alkaline fuel cells, was studied.

Immersion tests were performed for a total duration of 20 days to study the growth of corrosion products on the alloy's surface. Scanning Electron Microscopy (SEM), Transmission Electron Microscopy (TEM) and X-ray Diffraction (XRD) were carried out to characterize the structure and chemistry of the corrosion products. Also, electrochemical studies were carried out to study the kinetics of corrosion of the AZ31 alloy. Finally, the effect of adding 2 wt% sodium silicate (Na_2SiO_3) to the KOH electrolyte in order to manipulate the corrosion rate was also examined.

Tafel analysis confirmed that the corrosion potential of the AZ31 sample immersed in the Na_2SiO_3 + KOH solution reduced by 16% with respect to that of sample immersed in pure KOH. Although the AZ31 alloy contains only a trace amount of nickel, SEM-EDS characterization of the corrosion products revealed that they contained high levels of nickel, with XRD analysis confirming the presence of a nickel hydroxide layer. In the case of the sample immersed in Na_2SiO_3 + KOH electrolyte, an additional layer rich in silicates

developed, and likely acted as a barrier for diffusion of ions from surface of the AZ31 sample to the electrolyte. EIS results of modeling the surface corrosion phenomena revealed that a modified Randle's circuit represented the electrochemical processes occurring on the surface of the alloy. Warburg impedance for the sample immersed in Na_2SiO_3 + KOH was relatively high, suggesting a dissolution of ions from the surface into the highly alkaline KOH electrolyte.

Preface

This research thesis on the corrosion behavior of the AZ31 magnesium alloy was written in a partial requirement for the fulfillment of a Master's Degree (MASc) at the University of British Columbia (UBC), Okanagan. It is based on the experiments performed at University of British Columbia, Okanagan, Canada and at the Indian Institute of Technology (IIT), Chennai, India.

Parts of Chapter 4, Section 4.1., 4.2. and 4.5. were presented and published in *2016 Materials Science and Technology (MS&T)* conference proceedings in addition to being published as a refereed journal article: Somi Doja, Lukas Bichler and Simon Fan "Corrosion Behavior of AZ31 Magnesium Alloy in Highly Alkaline Environment" *Acta Metallurgica Sinica (English Letters)* 2017 doi:10.1007/s40195-017-0549-8. I was responsible for performing corrosion tests at UBC and IIT (with the help of local students and technical staff), data collection and analysis. I was also involved in writing the manuscript with guidance from my co-author and guide Dr. Lukas Bichler.

Parts of Chapter 4, Section 4.1, 4.2 and 4.5 were published in the *Corrosion 2017* conference: Somi Doja, Lukas Bichler, Simon Fan "Pitting Corrosion in AZ31 Magnesium Alloy in Potassium-Based Electrolytes". I was responsible for performing corrosion tests at UBC and identifying the effect of sodium silicate addition to the electrolyte on the corrosion behavior of the AZ31 alloy. I was also involved in writing the manuscript with guidance from my co-author and guide Dr. Lukas Bichler.

Table of Contents

Committee……..... **ii**

Abstract..... **iii**

Preface …… **v**

List of Tables ..... **ix**

List of Figures..... **x**

List of Abbreviations ..... **xiii**

List of Elements..... **xiv**

Acknowledgements ..... **xv**

Dedication ..... **xvi**

Chapter 1: INTRODUCTION **1**

Chapter 2: LITERATURE REVIEW **4**

2.1. Corrosion..... 4

2.1.1. Factors affecting corrosion 5

2.1.1.1. Gibbs Free Energy 5

2.1.1.2. Pilling-Bedworth (P/B) ratio..... 6

2.1.2. Corrosion tests..... 7

2.1.2.1. Immersion test..... 7

2.1.2.2. Tafel analysis 8

2.1.2.3. Electrochemical impedance spectroscopy 11

2.2. Magnesium 13

2.2.1. Corrosion behavior of Mg..... 14

2.3. Aqueous corrosion of Mg and alloying elements..... 15

2.3.1. Pourbaix diagram 15

2.3.2. Corrosion behavior of pure Mg and alloying elements in acidic electrolytes..... 17

2.3.3. Corrosion behavior of Mg and pure alloying elements in alkaline electrolytes .. 19

2.4. Magnesium alloys..... 21

2.4.1. AZ series 21
2.4.1.1. Properties of industrial AZ series alloys 23
2.4.1.2. Role of alloying elements on the corrosion behavior of AZ magnesium alloys……..……...25
2.4.2. Review of studies on aqueous corrosion of Mg alloys containing Al, Zn and Mn…….……..27

Chapter 3: EXPERIMENTAL PROCEDURE 28

3.1. Sample preparation for corrosion tests 32
3.2. Corrosion testing 33
3.2.1. Electrolyte preparation 33
3.2.2. Immersion tests 33
3.2.3. Electrochemical studies 35
3.2.3.1. Tafel polarization 38
3.2.3.2. Electrochemical impedance spectroscopy 39
3.3. Characterization of AZ31 samples 40
3.3.1. SEM analysis 40
3.3.2. XRD analysis 41
3.3.3. TEM analysis 41
3.4. ICP-OES analysis 42

Chapter 4: RESULTS AND DISCUSSIONS 43

4.1. Characterization of virgin and in-service AZ31 alloy 43
4.1.1. Virgin AZ31 plate 43
4.1.1.1. Top surface 43
4.1.1.2. Cross section 44
4.1.1.3. TEM analysis 46
4.1.2. KOH crystals 49
4.1.3. In-service AZ31 electrode 50
4.1.3.1. In-Service AZ31 electrode - Top surface 50
4.1.3.2. Cross-section - The cross section of the in-service electrode 56
4.2. Immersion test results 62

4.2.1. Analysis of the filter paper residue 62
4.2.2. Analysis of the AZ31 surface after immersion test 63
4.2.2.1. Analysis of corroded surface after immersion for 10 days 63
4.2.2.2. Analysis of corroded surface after immersion for 20 days 67
4.2.3. Analysis of the cross-section of the AZ31 plate after immersion for 20 days 72
4.2.3.1. Cross section of corroded AZ31 alloy in Electrolyte #1 72
4.2.3.2. Cross section of corroded AZ31 plate immersed in Electrolyte #2 75
4.2.4. Effect of immersion time on the corrosion surface layer 78
4.3. ICP-OES analysis 78
4.4. X-Ray diffraction studies 80
4.5. Electrochemical tests 82
4.5.1. Tafel polarization 82
4.5.2. Electrochemical impedance spectroscopy 84
4.6. Role of Al-Mn precipitates on corrosion 87

Chapter 5: CONCLUSIONS AND FUTURE WORK 88

5.1. Conclusions 88
5.2. Future work 89

Bibliography 90

Appendices 96

Appendix A: Corrosion measurement data for the repeats of polarization test 96
A1: 2nd Repeat of the electrochemical test 96
Appendix B: Additional data from immersion tests 99
B1: Immersion test results 99
B2: Growth of corrosion products on surface of sample immersed in Electrolyte #1 99

List of Tables

Table 2.1: Corrosion characteristics of commonly used alloying elements for Mg in acidic environments. [8] 18
Table 2.2: Corrosion characteristics of commonly used alloying elements for Mg in alkaline environments. [27] 20
Table 3.1: Chemical composition of virgin AZ31 plate (wt%). 29
Table 3.2: Polishing procedure for AZ31 samples. 32
Table 4.1: Composition of constituents of virgin AZ31 plate using SEM-EDS (wt%). 45
Table 4.2: Composition of Al-Mn precipitate from TEM-EDS analysis (wt%)..... 48
Table 4.3: Composition of KOH crystals used (wt%). 49
Table 4.4: Average composition of corrosion products in a pit of in-service AZ31 electrode (wt%). 51
Table 4.5: Chemical analysis of corrosion products on in-service AZ31 electrode (in wt%). 52
Table 4.6: Composition of the central region of the in-service AZ31 electrode (wt%). 56
Table 4.7: Composition of corrosion product layers on in-service AZ31 electrode (wt%).... 60
Table 4.8: Composition of filter paper residue in Electrolyte #1 and Electrolyte #2 (wt%). . 63
Table 4.9: Concentration of elements in the vicinity of the pit in Sample I (1, 20) (wt%). ... 69
Table 4.10: Composition of corroded pit in Sample (2, 20) (wt%). 72
Table 4.11: Concentration of elements in electrolyte prior and post corrosion (after 20 days) obtained from ICP-OES analysis (mg/L). 79
Table 4.12: Passivation parameters for corroded AZ31 alloy obtained from Tafel analysis. 83
Table 4.13: Electrochemical parameters obtained from EIS analysis. 86
Table A1.1: Values of the electrical parameters of the curve-fitted EIS data (Repeat 2)….. 98
Table B1.1: Corrosion rates obtained using immersion tests. 99

List of Figures

Figure 1.1: Scope of research. 3
Figure 2.1: A typical potentiodynamic polarization curve. [15] 10
Figure 2.2: A typical Nyquist plot. [9] 12
Figure 2.3: Pourbaix diagram for Mg in sea water. *(©1974, NACE International, by permission)* [24] 16
Figure 2.4: Mg-Zn-Al ternary phase diagram. *(Reprinted with permission from Elsevier)* [30] 22
Figure 2.5: Al-Mn binary phase diagram. *(Reprinted with permission from ASM International)* [32] 22
Figure 2.6: Effect of Fe and Mn on passivation of Mg alloys. (*Reprinted with permission by SAE © 2017 SAE International*) [45] 26
Figure 3.1: Virgin AZ31 magnesium alloy plate. 29
Figure 3.2: In-service AZ31 magnesium alloy electrode. 30
Figure 3.3: Polishing of metallographic samples: (a) Mark V lab manual polisher, (b) Polished AZ31 sample. 32
Figure 3.4 : Immersion test set-up: (a) Sample prior to immersion test, (b) Suspended sample. 34
Figure 3.5: Surface and cross-section of samples examined after an immersion test. 35
Figure 3.6: PARSTAT 4000 potentiostat. 36
Figure 3.7: Standard three-electrode configuration used for electrochemical experiments. 37
Figure 3.8: VersaStudio basic experimental set-up. 37
Figure 3.9: Experimental set-up for Tafel analysis. 38
Figure 3.10: Extrapolation of potentiodynamic polarization curves. 39
Figure 3.11: Experimental set-up for EIS test. 39
Figure 3.12: X-ray Diffractometer at IIT Chennai, India. 41
Figure 4.1: General microstructure of virgin AZ31 top surface: (a) Low magnification, (b) Al-Mn rich precipitates. 44
Figure 4.2: Cross section of virgin AZ31 plate: (a) General microstructure, (b) Al-Mn precipitates. 44

Figure 4.3: Cavities in etched top surface of virgin AZ31 plate (100x). 46
Figure 4.4: TEM analysis of Al-Mn precipitates: (a) Al-Mn precipitate, (b) SADP of AZ31 matrix, (c) SADP of Al-Mn precipitate obtained from TEM analysis..... 47
Figure 4.5: XRD analysis of virgin AZ31 plate. 49
Figure 4.6: SEM micrograph of in-service AZ31 electrode: (a) General surface overview, (b) Site for area scan of a corrosion pit. 50
Figure 4.7: Surface of in-service AZ31 electrode revealing “clean” and “dirty” corroded regions: (a) Low magnification and (b) High magnification view. 52
Figure 4.8: Pit initiation site in in-service AZ31: (a) Suspected pit initiation site on in-service AZ31 electrode, (b) Linescan results obtained from SEM-EDS analysis. 55
Figure 4.9: Central region of the cross section of in-service AZ31 electrode. 56
Figure 4.10: Cross-section of in-service AZ31 electrode. 57
Figure 4.11: Corrosion products on the surface of in-service AZ31 electrode: (a) Location #1, (b) Location #2. 57
Figure 4.12: SEM-EDS mapping of corrosion products on in-service AZ31 electrode. 58
Figure 4.13: Area scans along the cross section of in-service AZ31 electrode. 59
Figure 4.14: Linescan across the corrosion products on in-service AZ31 electrode’s cross-section. 61
Figure 4.15: Filter paper residue after 20 days of immersion in: (a) Electrolyte #1, (b) Electrolyte #2. 62
Figure 4.16: SEM image of Sample I (1, 10): (a) Low magnification view, (b) Corrosion products attached to the surface, (c) Pits on the surface. 64
Figure 4.17: Elemental mapping on corrosion products on Sample I (1, 10) using SEM-EDS. 65
Figure 4.18: Sample I (2, 10) showing: (a) Distribution of pits, (b) Corrosion products attached to a pit, (c) Micro pit. 66
Figure 4.19: Elemental mapping of a pit region in Sample I (2, 10). 67
Figure 4.20: Corrosion pits in Sample I (1, 20): (a) Macro view of the sample, (b) Large pits and voids. 68
Figure 4.21: SEM-EDS map of a pit on Sample I (1, 20). 68

Figure 4.22: Vicinity of a pit in Sample I (1, 20). 69
Figure 4.23 : Corrosion pits in Sample I (2, 20): (a) Macro view of the sample,
(b) Corrosion pits..... 70
Figure 4.24: SEM-EDS map of pits in Sample I (2, 20).. 71
Figure 4.25: Detailed view of a pit in Sample I (2, 20). 71
Figure 4.26: SEM-EDS map across corrosion products in Sample I (1, 20).. 73
Figure 4.27: Linescan along cross section of Sample I (1, 20): (a) Location of linescan,
(b) Detailed view of linescan location, (c) Inner layer of corrosion products,
(d) Middle layer of corrosion products, (e) Outer layer of corrosion products... 74
Figure 4.28: Elemental mapping of Sample I (2, 20). 76
Figure 4.29: SEM-EDS linescan across the corrosion products of Sample I (2, 20):
(a) Sample cross-section, (b) Linescan location, (c) Inner layer of corrosion products, (d) Middle layer of corrosion products, (e) Outer layer of corrosion products. 77
Figure 4.30: XRD results for AZ31 Sample I (1, 20). 81
Figure 4.31: XRD results for Sample I (2, 20). 82
Figure 4.32: Tafel polarization curve for Sample T (1) and Sample T (2). 83
Figure 4.33: EIS results for Sample E (1) and Sample E (2): (a) Nyquist plot,
(b) Equivalent circuit. 84
Figure 4.34: EIS results: (a) Bode phase plot, (b) Bode impedance plot..... 85
Figure 4.35: Role of Al-Mn precipitates in pitting corrosion of AZ31 alloy. 87
Figure A1.1: Tafel plots for Sample T (1) and Sample T (2)……..... 96
Figure A1.2: Nyquist plots for Sample E (1) and Sample E (2)…….....…. 97
Figure A1.3: Bode (a) magnitude and; (b) phase plots for Sample E (1) and Sample E (2).. 97
Figure B2.1: Cross-section of sample in Electrolyte #1 after immersion for 3, 6, 9, 12,
15 and 18 days……..……..... 100
Figure B2.2: Growth of corrosion products on sample immersed in Electrolyte #1
obtained from SEM-EDS analysis……..... 101

List of Abbreviations

ASM	American Society for Metals
CPR	Corrosion Penetration Rate
EDS	Energy Dispersive Spectroscopy
ICP	Inductively Coupled Plasma
OCP	Open Circuit Potential
OES	Optical Emission Spectroscopy
P/B	Pilling-Bedworth ratio
RO	Reverse Osmosis
SADP	Selected Area Diffraction Pattern
SEM	Scanning Electron Microscope
TEM	Transmission Electron Microscope
XRD	X-Ray Diffraction

List of Elements and Compounds

Al	Aluminum
Ag	Silver
C	Carbon
Ca	Calcium
Cu	Copper
Fe	Iron
H	Hydrogen
K	Potassium
Mg	Magnesium
Mn	Manganese
Na	Sodium
Ni	Nickel
O	Oxygen
Si	Silicon
Zn	Zinc
AgCl	Silver Chloride
KOH	Potassium Hydroxide
KCl	Potassium Chloride
$Mg(OH)_2$	Magnesium Hydroxide
Na_2SiO_3	Sodium Silicate

Acknowledgements

I would like to take this opportunity to express my gratitude to people who have helped me throughout my MASc program at UBC. I would first like to thank my supervisor, Dr. Lukas Bichler at the University of British Columbia, Okanagan. The door to Dr. Bichler's office was always open whenever I ran into trouble or had a query about my research.

I would also like to thank Mr. Simon Fan from ZincNyx Energy Solutions, Vancouver for his support. He was always there to answer any questions and give suggestions about my research.

I would like to thank my colleagues working at UBC who were always ready to help.

I would also like to thank Dr. B.S. Murty at Indian Institute of Technology, Chennai, India for giving me an opportunity to work with him by accommodating me in his lab.

Finally, I am grateful to my parents and my brother for providing me unfailing support and continuous encouragement throughout my years of study. This accomplishment would not have been possible without them. Thank you.

Dedication

To my parents, Mr and Mrs Doja and my brother Faraz Doja

Chapter 1: INTRODUCTION

Elemental magnesium (Mg) metal is widely abundant and is estimated to constitute approximately two percent of the Earth's crust and approximately 13% of sea water. [1] Mg is one of the lightest structural metals, with a density of only 1.74 g/cm^3. [2] Due to its low density, Mg alloys have an excellent strength to weight ratio and thus find use in many automotive, aerospace and consumer electronics applications, where a component weight is a critical design attribute.

Magnesium also has a highly negative electrode potential and thus is highly reactive with many elements on the periodic table. This high reactivity restricts the use of Mg and its alloys, primarily due to galvanic corrosion and coupling, leading to undesirable degradation of the Mg component. However, this property can be utilized for many benefits, including galvanic protection of steel, or the use of Mg alloys as electrodes (anodes) in fuel cells. Fuel cells are energy conversion devices in which energy of a chemical reaction is converted into an electrical energy. Mg-containing fuel cells are environmentally friendly in comparison to the commonly used lead-acid batteries and have a longer life compared to the conventional batteries. [3]

However, a prolonged exposure of Mg alloy electrodes to the harsh fuel cell environments leads to aqueous corrosion of the anodes, which significantly deteriorates the overall performance of the entire fuel cell system. Further, the presence of impurities or the presence of secondary intermetallic particles has an effect on the corrosion susceptibility of the Mg alloy electrodes.

In this work, the corrosion behavior of a commercial grade wrought Mg alloy AZ31 was studied in highly alkaline aqueous solutions. Literature on the aqueous corrosion of AZ31 in chloride- or sulphide-rich environments encountered in the automotive industries is widely available. [4] However, there is a paucity of literature on the corrosion behavior of Mg alloys in alkaline fuel cell environments. Therefore, this research focused on the corrosion behavior of AZ31 in alkaline solutions with a relatively high pH (15) levels. The objectives of this research were to:

i. Characterize in-service AZ31 magnesium alloy electrode exhibiting advanced stage of corrosion damage.

ii. Carry out immersion and electrochemical experiments in order to study the initiation and advancement of corrosion on AZ31 alloy exposed to highly alkaline environments.

iii. Study the effect of adding sodium silicate (Na_2SiO_3) to potassium hydroxide (KOH) electrolyte and its effect on the initiation of corrosion of AZ31 magnesium alloy.

In Chapter 2, a detailed literature review on the understanding of Mg alloy corrosion behavior is presented. In Chapter 3, the experimental approach used for the present research is described, followed by a discussion of the generated results in Chapter 4. Finally, the conclusions of the thesis and suggestions for future work are summarized in Chapter 5. Figure 1.1 provides an overview of the scope of the thesis.

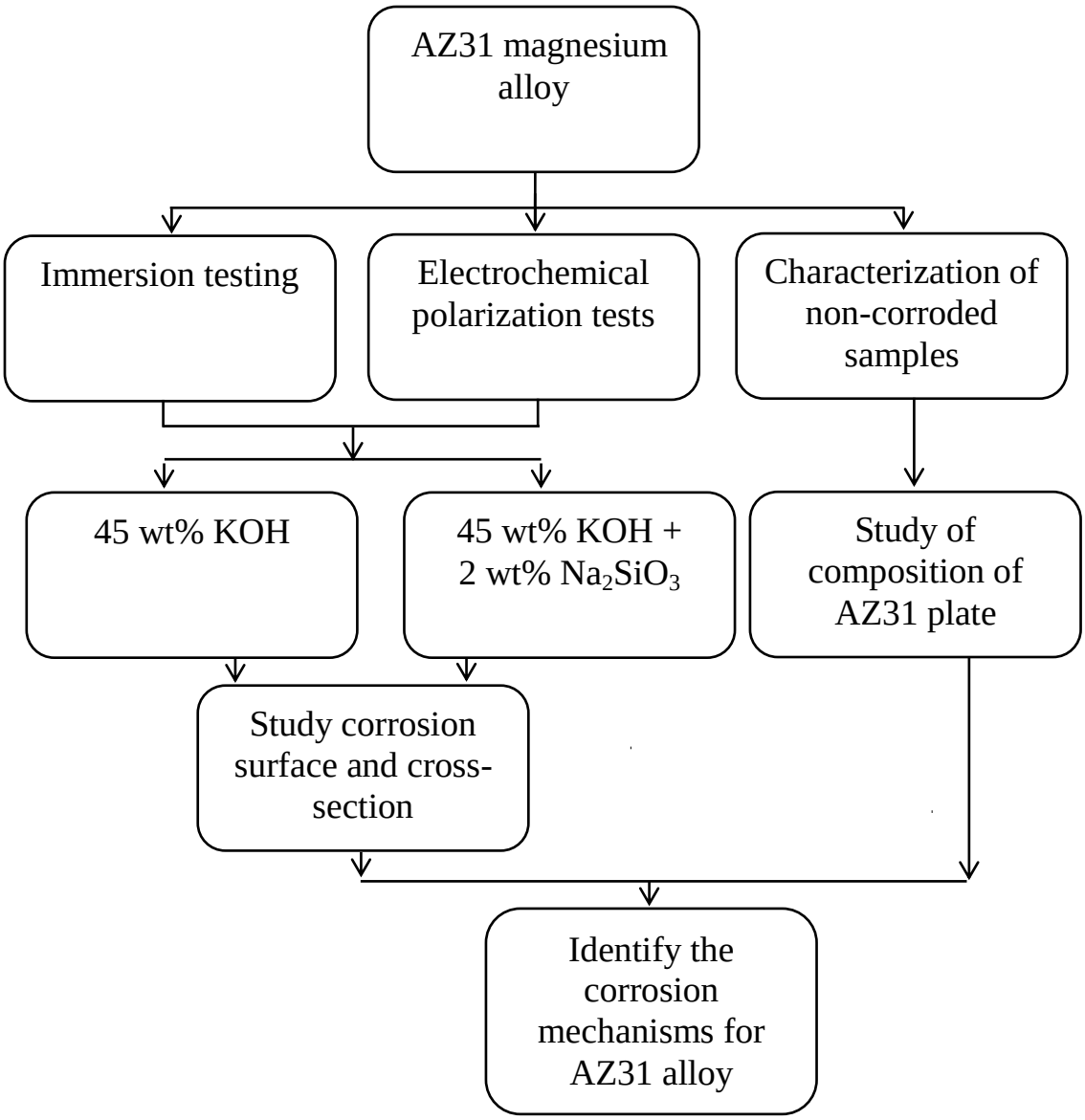

Figure 1.1: Scope of research.

Chapter 2: LITERATURE REVIEW

In this chapter, an overview of the literature pertaining to the fundamental mechanisms of corrosion of metals is presented. Then, a discussion of the corrosion behavior of Mg and its alloys in aqueous environments is provided.

2.1. Corrosion

Corrosion is the destructive attack of a material by chemical reaction with its environment.[5] The chemical reaction requires a transfer (a loss or a gain) of electrons, thus corrosion fundamentally requires the migration of ions or electrons. As a result, corrosion can be seen as an electrochemical process.

In many instances, physical changes of the corroding material involve the degradation of the material's surface, cracking or a loss of integrity. In ceramics and other non-metals, corrosion may not be readily visible, and other processes (such as swelling or decay) may dominate. [5] In the case of metals, corrosion usually involves several steps: [6]

i. **Absorption of chemical species**: The corrosion process is initiated by the absorption of chemical species on the surface of the corroding material. In aqueous environments, the chemical species maybe ions originating from the electrolyte.

ii. **Growth of corrosion products**: After the absorption of ionic species, chemical reactions initiate at the interface between the substrate and the electrolyte, and generally result in the formation of an oxide layer. The growth of the oxide can proceed in two directions: i) inwards (due to the loss of chemical species under the oxidized layer), or ii) outwards (due to the continued deposition of chemical species onto the layer).

The electrochemical reactions happen at two distinct locations, which are required for corrosion to occur: [7]

i. at an anode, where an oxidation reaction occurs, and
ii. at a cathode, where a reduction reaction occurs. The chemical species from the anode may be deposited onto the cathode after gaining electrons.

In the case of corrosion in aqueous environments, the above processes can take place even if the anodic and cathodic components in the galvanic cell are separated by a large distance [8], since the electrolyte acts as a path for the movement of electrons from the anode towards the cathode. As a result, as long as the electrolyte is in contact with both the anodic and cathodic sites, continuous corrosion prevails.

2.1.1. Factors affecting corrosion

The corrosion resistance or susceptibility of a material is largely governed by the Gibb's Free Energy and the nature of the corrosion products forming on the surface of the corroding material. [5] The nature of corrosion products is dependent on the Pilling-Bedworth (P/B) ratio, ambient temperature, ionic species in the electrolyte and the pH of the electrolyte. [9] The relation between these variables is governed by the Nernst equation used to calculate potential of a system. [10] These factors are discussed in the following sections.

2.1.1.1. Gibbs Free Energy

The main driver for corrosion of metals is governed by the ability of the chemical reactions to reduce the Gibb's Free Energy of the system (the system being the metal and the electrolyte). [5] Based on thermodynamic principles, metals seek to attain a minimum Gibb's

Free Energy state. [10] Therefore, any chemical reaction (e.g., the formation of an oxide) leading to the reduction of the Gibb's Free Energy will readily take place. For example, the net reaction for the formation of magnesium hydroxide ($Mg(OH)_2$) due to the exposure of Mg to water (H_2O) is provided in Equation 1. [5]

$$\mathbf{Mg + H2O + \frac{1}{2}O_2 \rightarrow Mg(OH)_2} \quad \textbf{(1)}$$

The Gibbs Free Energy change for Equation 1 is ΔG^0= -596.6 KJ. [5] This relatively large negative value of the Gibbs Free Energy indicates the high tendency of Mg to react with water and oxygen (O_2) and form a surface oxide.

2.1.1.2. Pilling-Bedworth (P/B) ratio

An important factor controlling the rate of degradation of a material during corrosion is the P/B ratio, which represents the ratio of the volume occupied by the corrosion products to that of the base metal. [5] If the P/B ratio significantly deviates from unity (i.e., >>1 or <<1), the volumetric mismatch between the corrosion products and the substrate may attribute to the evolution of high stresses at the corrosion product interface. For example, in the case of $Mg(OH)_2$ formation on the surface of Mg, the P/B ratio is 1.73, which indicates a significant volumetric expansion of the $Mg(OH)_2$ on the surface, leading to high porosity and cracking in the hydroxide layer. [11] Therefore, such corrosion products may offer only limited protection for the substrate and continuous corrosion of the Mg substrate will occur with degradation or cracking of the surface oxide.

2.1.2. Corrosion tests

Evaluation of the degradation behavior of materials in aqueous environments can be achieved by several methods. Ultimately, the aim is to quantify the degradation by measuring the corrosion rate, which represents the amount of a material removed per unit of time. [6] Methods relevant to the present work are discussed in the following sections.

2.1.2.1. Immersion test

In an immersion test, the specimen is completely immersed in an electrolyte for a prescribed period of time. [6] The immersion test is usually performed to study the nature of corrosion products as well as the corrosion penetration rate (CPR). By calculating the loss of weight in the material due to the exposure to an electrolyte, Equation 2 can be used to determine CPR as outlined in ASTM G37-12a standard: [12]

$$CPR = \frac{k\Delta W}{\rho AT} \quad \textbf{(2)}$$

Where:

CPR is the corrosion penetration rate in µm/ year

k= 8.76 x 10^7 is the constant for converting corrosion rate from cm/h to µm/ year

ΔW is the loss of weight in g

ρ is the density in g/cm^3

A is the area exposed to corrosion in cm^2

T is the time in hours

The sample can be immersed in the electrolyte for the entire duration of the immersion test. However, if the corrosion degradation is rapid and a more accurate measurement is required, the sample can be removed from the electrolyte, cleaned, and the weight loss measured, following by a re-immersion back into the electrolyte. [6] This process is repeated for a finite number of cycles, and Equation 2 is used to calculate the intermediate CPR values after each immersion segment.

Although the immersion test is relatively simple to carry out, it has limitations. First, the electrolyte absorbed on the surface of the sample can overestimate the weight of the corrosion products. [13] Another drawback of this method is that the substrate may inadvertently be removed along with the corrosion products when measuring the weight loss.[13] Also, for micro-galvanic corrosion occurring on the surface of a material (e.g., via pitting corrosion), the resultant corrosion rate may not be accurately measured, because of the relatively low weight loss. However, despite the low weight loss in the corroded sample, material failure may still occur. [14] Therefore, results obtained from weight loss measurements may carry a relatively high level of inaccuracy and may not be directly applicable when examining diverse forms of corrosion.

2.1.2.2. Tafel analysis

The corrosion rate can also be estimated by performing tests where the sample of interest is connected to an electrical circuit, such that a flow of electrons (in the sample and the electrolyte) is accelerated. One variation of this approach is called the “Tafel analysis”, where the applied potential is varied above and below the corrosion potential of the sample to obtain a cathodic and an anodic curve. Thereafter, the corrosion potential is inferred as the potential at the intersection of the anodic and cathodic curves (i.e., a point where the cathodic

and anodic current densities are equal). [14] The Tafel plot is a logarithm of the current with respect to the applied potential (shown in Figure 2.1), which can be explained with the help of Butler-Volmer Equation 3. [14]

$$I = I_{corr}\left(e^{\frac{2.303\,(E-E_{corr})}{\beta_a}} - e^{\frac{2.303\,(E_{corr}-E)}{\beta_c}}\right) \quad \textbf{(3)}$$

Where:

I is the measured current in the cell in A

I_{corr} is the corrosion current at corrosion potential in A

E is the electrode potential in V

E_{corr} is the corrosion potential in V

β_a and β_c are the anodic and cathodic Tafel constants (V/decade)

In Equation 3, the first component is the contribution to the corrosion current (for the total current measured) from the anodic reaction, whereas the second component is the contribution from the cathodic reaction. For a case where E =E_{corr}, equal current is generated from both the cathodic and anodic processes and results in a zero net current. In cases where E<< E_{corr}, the contribution from the cathodic reaction is more than from the anode (which can be neglected) and hence the cathodic polarization dominates. Similarly, when E>> E_{corr}, the anodic polarization dominates. Figure 2.1 shows a typical Tafel curve. The cathodic and anodic branches are extrapolated to meet at a point. This point gives the value of corrosion current in the circuit.

Additional data provided by Tafel plot analysis is related to the polarization resistance of the sample. It is calculated mathematically from the slope of the Tafel curve near the corrosion potential via the Stern-Geary equation (Equation 4): [7]

$$I_{corr} = \frac{\beta_a \beta_c}{R_p 2.303 (\beta_a + \beta_c)} \quad \textbf{(4)}$$

Where:

R_p is the polarization resistance in Ωcm^2

β_a and β_c are the anodic and cathodic Tafel constants in V/decade

I_{corr} is the corrosion current density in A/cm^2

Equation 4 provides another method to calculate the corrosion current in a system. However, the accuracy of the equation depends on the existence of a linear Tafel region, as indicated in Figure 2.1 below.

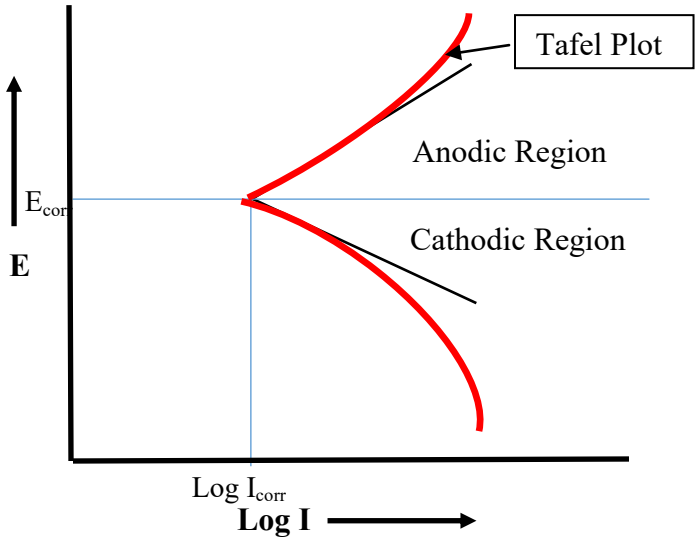

Figure 2.1: A typical potentiodynamic polarization curve. [15]

2.1.2.3. Electrochemical impedance spectroscopy

Electrochemical Impedance Spectroscopy (EIS) is an experimental method used to characterize an electrochemical system. [14] During EIS, an experiment is performed by varying the input potential sinusoidally using a potentiostat. The properties related to the impedance (such as the magnitude and phase difference of the real and imaginary components) of the system are measured against frequency. The elements involved in the corrosion experiment are converted into electrical equivalents. Thus, the components of the corroding system (i.e. the system containing the corrosion products, substrate and the electrolyte) may act as capacitor, inductor or a resistor in an electrical circuit. The resulting circuit analysis enables modeling of the electrochemical processes occurring in the system.

A Nyquist plot shows the relationship between the real and imaginary values of impedance, as illustrated in Figure 2.2. The different points on the semicircle represent different values of responses at varying frequencies. The magnitude of frequency decreases by tracing the curve in the clockwise direction, as indicated in the figure. The imaginary value of the impedance (Z_i) is 0 for starting and end points of the semi-circular region, and such a circuit would be expected to behave as a purely resistive circuit. For non-zero values of imaginary impedance, the circuit would be composed of a capacitive or an inductive reactance, in addition to having resistance. Solution resistance (R_s) and the polarization resistance (R_p) can be directly calculated from the Nyquist plots, as shown in Figure 2.2.

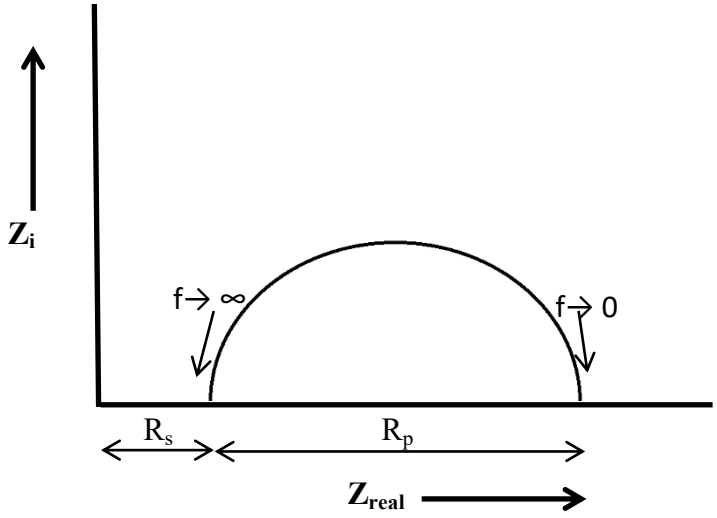

Figure 2.2: A typical Nyquist plot. [9]

One shortcoming of the Nyquist plot analysis is that the quantitative values of frequencies cannot be determined at different impedance values. As a result, Bode plots must be created to extrapolate the relationship between the frequency and the absolute value of the impedance and phase shifts. The value of capacitive and inductive reactance can be calculated using Equation 5 and Equation 6: [16]

$$\mathbf{X_c = \frac{1}{2\Pi fC}} \quad \textbf{(5)}$$

$$\mathbf{X_L = 2\Pi fL} \quad \textbf{(6)}$$

Where:

X_C is the capacitive reactance in Ω

X_L is the inductive reactance in Ω

f is the frequency in Hz

C is the capacitance in F

L is the inductance in the circuit in H

Therefore, with the help of Bode plots, one can determine the nature (i.e., capacitive, inductive or resistive) of a circuit at a particular frequency. Unlike Nyquist plots, Bode plots provide information corresponding to the exact values of frequencies. As a result, with the Nyquist and Bode plots, valuable information pertinent to modeling of corrosion phenomena in diverse systems can be obtained.

2.2. Magnesium

Magnesium is one of the most abundant elements in the Earth's crust. [2] Pure Mg is ductile, malleable and light in weight. [17] Therefore, it has found many applications in the automobile and aeronautical industries. However, despite its many favorable mechanical properties, use of Mg is limited in industrial application due to environmental corrosion issues. [2] [18]

Mg has an electrode potential of -2.37V [19] [20] and has a long shelf life because of a low electrochemical equivalence. [20] Due to these properties, Mg can be used as electrodes (anodes) in batteries. [21] However, being highly reactive, it has a tendency to corrode rapidly.

Alloying Mg with other elements impacts the corrosion behavior of an Mg alloy. In general, pure Mg has a lower corrosion rate than an Mg alloy. [22] However, Mg also has poor corrosion resistance, which makes using Mg and its alloys in anodes a challenge for industrial applications. [19] [22]

2.2.1. Corrosion behavior of Mg

Mg is a highly reactive metal and corrodes easily when exposed to air or moisture, with the primary corrosion product being $Mg(OH)_2$. The standard Reduction-Oxidation (Redox) reactions involved in the corrosion of magnesium are: [23]

$$\mathbf{Mg \rightarrow Mg^{2+} + 2e^-} \qquad \textbf{(anode) (7)}$$

$$\mathbf{2H_2O + 2e^- \rightarrow H_2 + 2\,(OH)^-} \qquad \textbf{(cathode) (8)}$$

As seen in Equation 7 and Equation 8, Mg oxidizes to form divalent Mg cations, while hydrogen gas (H_2) is evolved at the cathode. The Mg cation reacts with hydroxide ions to form $Mg(OH)_2$, as seen in Equation 9 below. [23]

$$\mathbf{Mg^{2+} + 2\,(OH)^- \rightarrow Mg(OH)_2} \qquad \textbf{(9)}$$

It has been observed that the corrosion rate increases at the beginning of the corrosion process until it reaches some critical value and then it stabilizes. [19] [20] However, for Mg, corrosion rate seems to increase with an increase in immersion time. [25] Many scientists have given different explanations to this increase. For example, according to Udhayan and Bhatt [20], this behavior is due to the initial dissolution of Mg and subsequent formation of unstable $Mg(OH)_2$. However, according to Shi, formation of $Mg(OH)_2$ is attributed to the increase in surface roughness of the corroded surface due to the formation of oxides/hydroxides in the beginning of the process. [22]

2.3. Aqueous corrosion of Mg and alloying elements

The behavior of Mg and some elements in acidic and alkaline aqueous solutions is discussed in the following sections.

2.3.1. Pourbaix diagram

Pourbaix diagrams relate the pH of the electrolyte and the electrochemical behavior of a metal in an aqueous environment. [10] A vertical line on the Pourbaix diagram indicates that the chemical reaction is independent of the potential (E,V) of the system, suggesting that no electron transfer occurs in the reaction. On the other hand, a horizontal line on the Pourbaix diagram indicates that only pH dependence exists.

With the help of the Pourbaix diagrams, the pH and potential range can be found wherein the metal is not active, but forms stable corrosion products. For example, the Pourbaix diagram for Mg in sea water is shown in Figure 2.3.

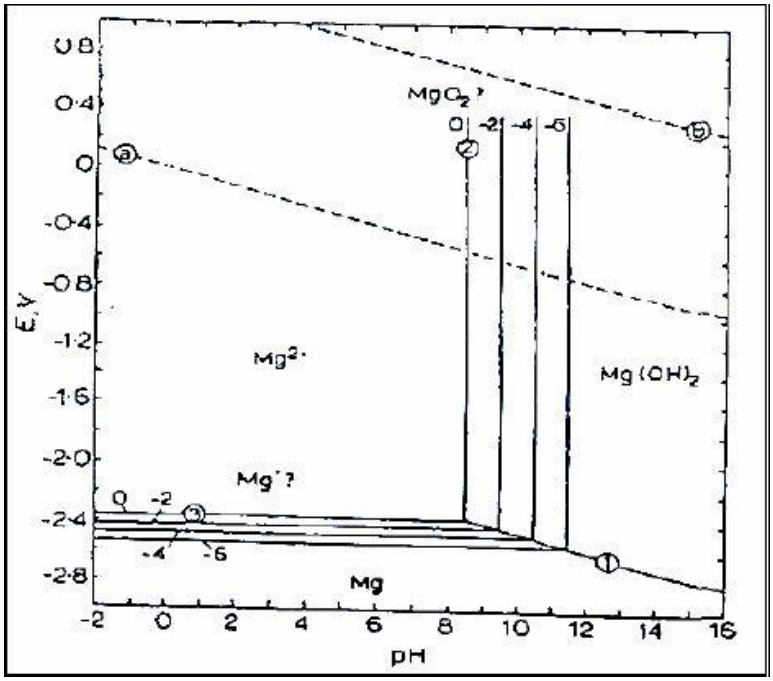

Figure 2.3: Pourbaix diagram for Mg in sea water. ***(©1974, NACE International, by permission)*** **[24]**

As seen in Figure 2.3, Mg^{2+} ions are stable in acidic solutions. For alkaline solutions, $Mg(OH)_2$ is expected to form. A major drawback of using the Pourbaix diagram, however, is that it does not provide any information about the reaction rates. Therefore, the information about the stable species predominant at a particular pH solution and applied potential values is de-coupled from the rate of formation of these species. Also, the nature of the corrosion products is not given. For example, Figure 2.3 reveals that $Mg(OH)_2$ forms for pH values greater than 12. However, the nature of the formed layer (i.e., porosity, stability, etc.) remains unknown. [5]

Corrosion behavior of Mg and some elements found in Mg alloys in different aqueous media are discussed in the subsequent sections. Corrosion resistance of the elements often added to Mg alloys is highlighted.

2.3.2. Corrosion behavior of pure Mg and alloying elements in acidic electrolytes

Acids are frequently used as important solvents and electrolytes in many industries and engineering applications where Mg alloys are also used. [8] The corrosion characteristics of Mg and commonly used alloying elements in organic and inorganic acids are summarized in Table 2.1.

Table 2.1: Corrosion characteristics of commonly used alloying elements for Mg in acidic environments. [8]

Acid	***Electrolyte properties***	***Element***	***Corrosion behavior***	***Additional points***
1) Formic acid (HCOOH)	•Most corrosive out of the known organic acids. •Exhibits high reducing potential.	*Aluminum*	Good corrosion resistance when no impurities are present (at room temperature).	Can be used for shipment and storage of formic acids when impurities are absent.
		Copper	Corrosion resistance is determined by the presence of reducing agents.	Can be resistant to formic acid at high temperatures in the absence of reducing agents.
		Nickel	Good corrosion resistance in formic acid.	Good corrosion resistance even at elevated temperatures.
2) Hydrochloric Acid (HCl)	•Used in acid pickling, cleaning processes.	*Aluminum*	Poor corrosion resistance.	Poor corrosion resistance due to high susceptibility to pitting corrosion.
		Copper	Limited use in HCl solutions due to high susceptibility to corrode.	Low corrosion rates under reducing conditions.
		Nickel	Corrosion resistant to dilute HCl solutions in the absence of oxidizing agents.	Better corrosion resistance is achieved when nickel is alloyed with chromium and molybdenum.

Table 2.1: Corrosion characteristics of commonly used alloying elements for Mg in acidic environments. (Continued) [8]

Acid	Electrolyte properties	Element	Corrosion behavior	Additional points
3) Hydrofluoric Acid (HF)	•Used for etching and cleaning of metals.	*Aluminum*	Poor corrosion resistance at any concentration.	It is known to crack due to HF exposure.
		Magnesium	Good corrosion resistance up to 40% HF at room temperature.	Protection of magnesium is due to the formation of a magnesium fluoride film.
		Copper	Average corrosion resistance in the absence of oxidizing agents.	Copper tubing is known to be used for short term services in the absence of any contaminants.
		Nickel	Better corrosion resistance when compared to other alloys.	Corrosion rate increases with HF concentration and temperature.

2.3.3. Corrosion behavior of Mg and pure alloying elements in alkaline electrolytes

Once initiated, corrosion of Mg alloys in basic aqueous electrolytes often results in the formation of a $Mg(OH)_2$ layer. [25] [26] However, due to the P/B ratio for $Mg/Mg(OH)_2$ being 1.73 [11], this layer readily nucleates voids and subsequently cracks, thus promoting localized and accelerated corrosion of Mg alloys if the electrolyte is able to continuously penetrate the cracked hydroxide layer. [23] The most commonly used alkaline electrolytes in the fuel cell industries include sodium and potassium hydroxides. The corrosion behavior of

Mg and its different alloying elements is believed to be similar in both the electrolytes. [8] [27] Table 2.2 summarizes the behavior of Mg and its common alloying elements in sodium hydroxide (NaOH) and potassium hydroxide (KOH). As seen in the table, corrosion of aluminum (Al) is readily activated. Corrosion of elemental Al in caustic solutions (e.g., NaOH) is controlled by competing processes of film growth and dissolution. [8] The film formed is known to possess an inner compact layer and an outer layer. [27] At higher pH values (pH>12), the outer layer often contains cavities, which provide a path for the electrolyte to further corrode the substrate, thereby increasing the corrosion rate. Impurities (for example Fe^{2+}) may get reduced on the surface of the Mg alloy, and form sites for H_2 evolution [8] leading to accelerated corrosion rates.

Table 2.2: Corrosion characteristics of commonly used alloying elements for Mg in alkaline environments. [27]

Base	***Properties***	***Metal/ Alloy***	***Corrosion behavior***	***Additional points***
Sodium hydroxide/ potassium hydroxide (NaOH/ KOH)	• Used in various processes of manufacturing of pulp, paper, plastic, soap etc.	*Aluminum*	Poor corrosion resistance for even dilute solutions.	The Al^{3+} ion is easily formed when the alloy is immersed in NaOH/KOH solution.
		Copper	Average corrosion resistance.	May be used when alloyed with nickel in the absence of oxidizing agents.
		Magnesium	Relatively resistant to corrosion	Forms a partially protective $Mg(OH)_2$ or MgO layer. [25]
		Nickel	Resistant to corrosion	Susceptible to Stress Corrosion Cracking (SCC) in concentrated solutions

Although Mg is considered relatively resistant to corrosion in highly alkaline environments, corrosion remains a significant concern for long time application of Mg alloys in alkaline environments.

2.4. Magnesium alloys

Magnesium alloys are often used in structural, automotive and aircraft applications due to their high strength to weight ratios. [2] Specifically, magnesium-aluminum (Mg-Al) alloy systems show excellent mechanical performance, ease of processing and optimal cost. [28]

2.4.1. AZ series

The AZ series Mg alloys contain aluminum (Al) and zinc (Zn) as the primary alloying elements. In general, Al is added to Mg alloys to enhance the strength, hardness and castability. [29] An Al content of 6% provides an optimum balance of strength and ductility compared to other Mg-Al-Zn alloys. [29] Zn is added to Mg to improve the room temperature strength, while it is added to Mg-Al alloys to enhance the corrosion resistance in NaCl. [2]

A ternary phase diagram for Mg alloys with Al and Zn additions is shown in Figure 2.4. As can be seen from the phase diagram, AZ alloys may contain Mg-Zn and Mg-Al solid solutions, as well as Mg-Al-Zn phases.

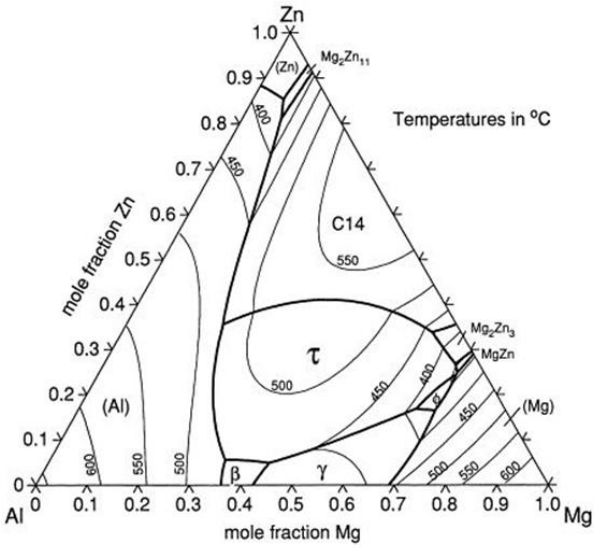

Figure 2.4: Mg-Zn-Al ternary phase diagram. ***(Reprinted with permission from Elsevier)*** **[30]**

Manganese (Mn) is also known to be present in some Mg-Al alloys. [2] From the Al-Mn binary phase diagram (Figure 2.5), the Al-Mn precipitate may form in alloys of AZ series depending on the concentration of Mn. [31] Also, referring to the Mg-Al binary phase diagram, the $Mg_{17}Al_{12}$ (β-phase) is expected to readily form in the AZ series alloys. [25]

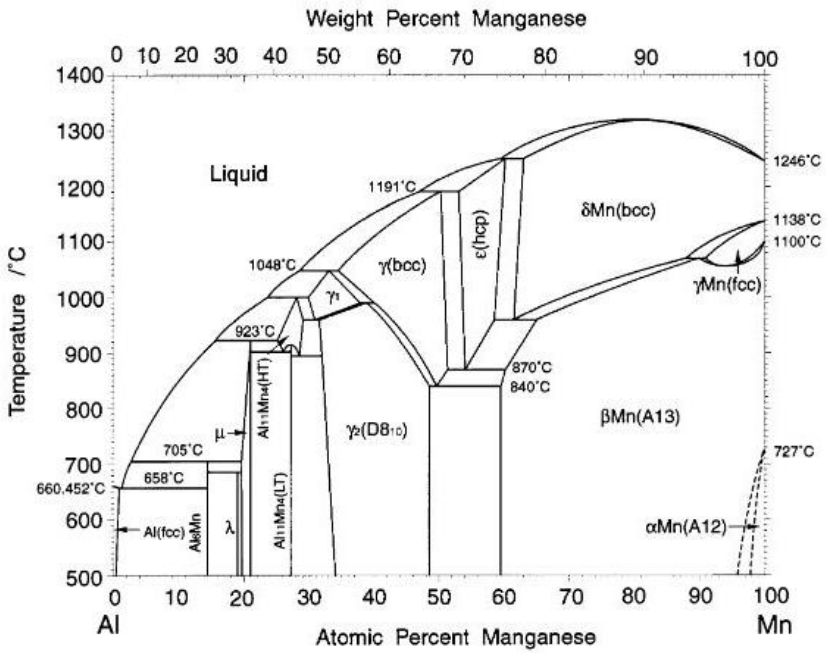

Figure 2.5: Al-Mn binary phase diagram. ***(Reprinted with permission from ASM International)*** **[32]**

It is believed that Mg-Al alloys with Al content less than 3% are relatively resistant to intergranular corrosion. The tendency of the alloy for intergranular corrosion increases with an increase in the Al content [33], due to the formation of the Mg_2Al_3 phase, which is anodic with respect to the Mg matrix.

Other impurities, like nickel (Ni), iron (Fe) and copper (Cu), were shown to have a deleterious effect on the corrosion resistance of Mg alloys [23], since they are highly cathodic in relation to the Mg matrix. [29] As a result, they rapidly establish a micro-galvanic cell, leading to rapid corrosion. Cu is also known to form Mg(Cu-Zn) eutectic known to be cathodic with respect to the α-Mg matrix. [34] [35] Similarly, precipitates in AZ series alloys are generally cathodic with respect to the Mg matrix (except Mg_2Ca) and thus also establish additional micro-galvanic corrosion cells [36], leading to advanced dissolution of the matrix around these precipitates. [37]

2.4.1.1. Properties of industrial AZ series alloys

i. AZ31 magnesium alloy

The AZ31 Mg alloy (3 wt% Al, 1 wt% Zn, bal. Mg) is a popular wrought alloy with good room temperature properties. [38] [39] It has a good strength (tensile strength of 240 MPa) and is easy to weld when compared to other Mg-Al-Zn alloys. [29]

In the AZ31 alloy, an Al or Al - Mg oxide forms during atmospheric corrosion and may provide limited protection against corrosion. [40] For the AZ31 alloy, Al-Mn rich precipitates were observed by several researchers, and suggested to possibly contribute to the film formation. [31] [41]

Despite the protective Al-Mg oxide, long term industrial use of the AZ31 alloy has been limited, due to issues related to the alloy's poor corrosion resistance [38] [42]. The presence of the Al-Mn or Al-Mn-Fe precipitate has a deleterious effect on the corrosion resistance of the alloy. [31] These precipitates are known to be cathodic with respect to the Mg matrix solid solution and readily establish a micro-galvanic corrosion cell in the alloy. [31] Cano *et al*. [37] observed filiform like corrosion behavior near the Al-Mn precipitates in NaCl containing electrolyte, which ultimately led to the degradation of the alloy.

ii. **AZ61 magnesium alloy**

The AZ61 Mg alloy (6 wt% Al, 1 wt% Zn, bal. Mg) is a common extruded wrought Mg alloy. [43] It has a good strength (tensile strength of ~260 MPa) when compared to other Mg-Al-Zn alloys. [29]

Since the Al content in AZ61 is higher than that in AZ31, an Al oxide layer readily forms [29] on immersion of sample in aqueous environments, as was experimentally verified by Samaniego *et al.* [44] who investigated immersion of AZ61 in 0.5M NaCl electrolyte. Therefore, formation of a relatively more protective Al_2O_3 layer is easier in AZ61 alloy when compared to AZ31. However, with an increase in the immersion time, micro-galvanic corrosion proceeds at a much higher rate due to the presence of greater concentration of highly cathodic β-particles. [25]

iii. AZ91 magnesium alloy

The AZ91 Mg alloy (9 wt% Al, 1 wt% Zn, bal. Mg) is a common cast Mg alloy. [2] Die cast AZ91 alloys have a good castability and an average strength (tensile strength of ~ 215 MPa).[29]

A number of studies have been performed to understand the corrosion behavior of AZ91 in aqueous environments. The $Mg_{17}Al_{12}$ β-phase is known to be highly cathodic with respect to the α-Mg matrix. [25] The distribution of this phase in the matrix governs the corrosion behavior of the alloy. If the composition and distribution of the β-phase is uniform, it may protect the Mg matrix from corrosion, because the β-phase present on the grain boundaries acts as a barrier to corrosion of the grain interior. However, if this phase is scattered throughout the matrix as a divorced eutectic, it has the tendency to couple with the matrix and further accelerate micro-galvanic corrosion. [25]

2.4.1.2. Role of alloying elements on the corrosion behavior of AZ magnesium alloys

When impurities are present in an alloy, they may act as a cathode or an anode with respect to the matrix, and form micro-galvanic corrosion cells. In the case of Mg alloys, impurities like Ni, Fe and Cu have a detrimental effect on the corrosion resistance of the alloy. [9] [23]

Ni has a low solid solubility in Mg and often remains as an elemental Ni in the matrix. [2] Also, Ni is highly cathodic and is often responsible for accelerating pitting corrosion in AZ Mg alloys. [2]

Fe is generally insoluble in Mg solid solution and exists as free species (i.e., Fe does not combine with other elements). [23] Fe has a deleterious effect on the corrosion of Mg

alloys. Being highly cathodic with respect to the α-Mg matrix (according to the electrochemical series), Fe galvanically couples with the matrix and accelerates its degradation. To combat the effect of Fe, Mn is added to AZ alloys to improve corrosion resistance, since Mn binds to Fe and forms an Mn-Fe precipitate, which is less cathodic in than elemental Fe. [23] However, there is an optimum ratio between these two elements in order to passivate the alloy's surface. Figure 2.6 shows the optimum Fe to Mn ratio to prevent the presence of elemental Fe. If the Fe:Mn ratio is greater than the tolerance limit, corrosion of the AZ series alloys is greatly accelerated.

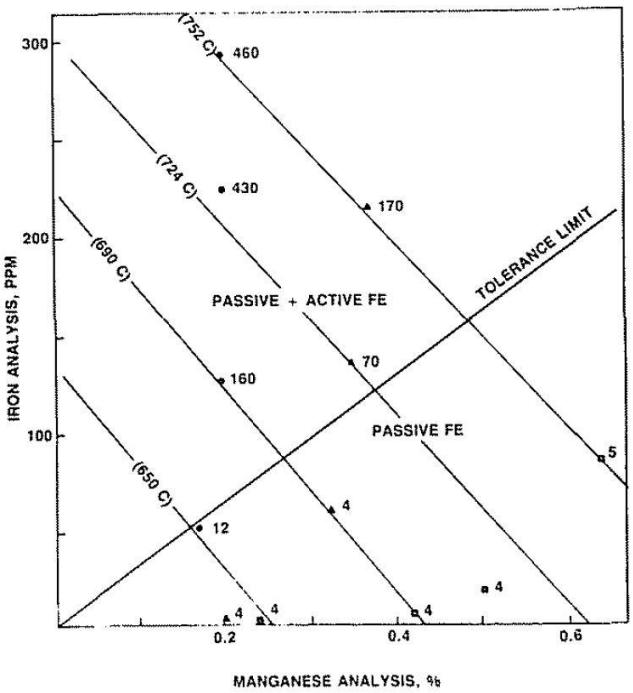

Figure 2.6: Effect of Fe and Mn on passivation of Mg alloys. (*Reprinted with permission by SAE © 2017 SAE International*) [45]

Copper (Cu) is known to act as a cathodic site in Mg alloys. Also, it is more noble than Mg, therefore Cu ions may gain electrons and get deposited on the substrate. However, Cu may also form Mg_2Cu phase, which is known to be cathodic in nature when compared to the Mg matrix. [6] [34] [46]

Calcium (Ca) is added to AZ alloys to induce grain refinement. It increases ductility and improves the rolling behavior of AZ31. [2] However, Ca may accelerate pitting corrosion due to the formation of the Mg_2Ca phase, which jointly, with Al and Mg, acts as an anodic site and promotes preferential corrosion. The optimal concentration of Ca (in alkaline environments) yielding reduced corrosion of the AZ series alloys has not been reported to-date. [47] [48] [49]

Secondary phases present in the Mg alloys generally act as sites for the formation of localized galvanic cells. [6] These phases could either be Al-Mn rich precipitates or $Mg_{12}Al_{17}$ β-phase.

2.4.2. Review of studies on aqueous corrosion of Mg alloys containing Al, Zn and Mn

The corrosion behavior of the AZ series of Mg alloys was extensively studied over the past decades. Literature on the corrosion performance of these alloys in diverse environments and electrolytes is available. Although Al and Mn are added to Mg alloys to improve strength and castability, these elements readily form precipitates, which are noble with respect to the α-Mg matrix, thereby enabling formation of micro-galvanic cells where the matrix is degraded. [50] For example, Sudholz *et al*. reported that Al containing precipitates were more noble than the Mg_2Ca or $MgZn_2$ precipitates. [49] Also, the $Mg_{17}Al_{12}$ phase present in Mg-Al alloys has been shown to form a cathodic couple with the α-Mg matrix. [39] [51] Pitting corrosion was reported to relate to the formation and degradation of the $Mg_{17}Al_{12}$, Al_xMn_y and Al-Mn-Fe precipitates. [34] Lunder *et al*. observed *in-situ* production of H_2 gas at the Al-Mn-Fe precipitates when AZ91 alloy was exposed to 5 % NaCl electrolyte. [52] Pardo *et al*. [50] studied the corrosion of AZ91, AZ31 and AZ80 alloys in 3.5 wt% NaCl electrolyte, and

determined that Al in the solid solution directly governed the corrosion resistance of the alloys. Specifically, they observed that the α-Mg solid solution was preferentially attacked due to presence of $Mg_{17}Al_{12}$ or Al-Mn rich compounds by forming micro-galvanic cells with them. [50]

Matsubara *et al.* [53] studied the effect of Fe on the corrosion behavior of AM50 and AM60 Mg alloy and reported that regions with localized elevated Fe concentrations were associated with the onset of corrosion in the alloys. [53] As a result, the concentration of impurities must be maintained at or below tolerance limits for industrial Mg alloys. [54] [25]

The corrosion test used to study the corrosion behavior of alloys also influences the outcome of a corrosion study. For AZ31 Mg alloy, Thirumalaikumarasamy *et al.* [55] found that corrosion rates obtained from immersion tests were much greater than those obtained from Tafel analysis in NaCl solution. This was attributed to the greater area of the sample exposed to the electrolyte in the case of an immersion test, thus enabling higher corrosion rates. Similarly, the sample preparation method also affects the corrosion rate of the alloy samples, as reported by Samaniego *et al.* [44] For example, a polished surface of AZ31 exhibited a lower corrosion rate in comparison to an as-received sample of AZ31 in 0.6M NaOH.

Although corrosion studies on the exposure of Mg alloys to highly alkaline electrolytes have not been reported extensively in the literature to-date, it is expected that impurities and precipitates in the AZ alloys would remain cathodic with respect to the magnesium matrix and thus have a direct impact on the corrosion resistance of Mg alloys.

Chapter 3: EXPERIMENTAL PROCEDURE

In this chapter, the procedures and methods used to perform the experiments in this research are outlined. Specifically, sample preparation for microstructural analysis, as well as methods for corrosion studies including immersion testing, electrochemical impedance spectroscopy and Tafel analysis are outlined in detail.

In this work, several AZ31 alloy samples were examined. Their description is as follows:

i. Virgin AZ31

Figure 3.1 shows the virgin AZ31 plate (a 10 mm thick rectangular plate) obtained from ZincNyx Energy Solutions, Canada. This plate was new, unused and hermetically sealed AZ31 magnesium alloy. The chemical composition of the virgin AZ31 alloy is provided in Table 3.1.

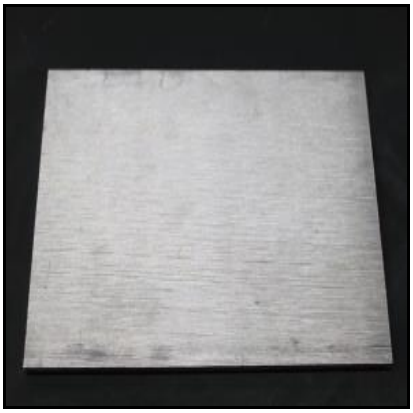

Figure 3.1: Virgin AZ31 magnesium alloy plate.

Table 3.1: Chemical composition of virgin AZ31 plate (wt%)*.

Element	Mg	Al	Zn	Ca	Mn	Fe	Ni	Cu
Concentration	95.40 ±0.13	2.99 ±0.07	1.25 ±0.08	0.04 ±0.03	0.20 ±0.04	0.08 ±0.10	0.01 ±0.00	0.03 ±0.01

**± indicates the error in measurement.*

ii. In-service AZ31 electrode

A sample of an AZ31 electrode was obtained from ZincNyx Energy Solutions Canada. This electrode was used in a fuel cell environment, and was exposed to 45 wt% KOH with 2 wt% Na_2SiO_3. The exposed area of the electrode had visible signs of corrosion, as seen in Figure 3.2.

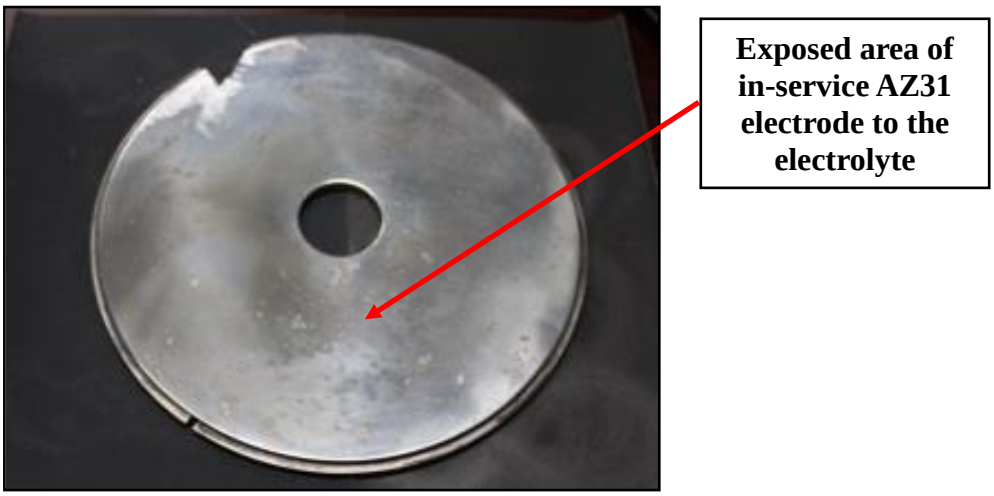

Figure 3.2: In-service AZ31 magnesium alloy electrode.

Two samples were extracted from the in-service AZ31 electrode. The first sample enabled observation of the corroded "top surface", which was in direct contact with the electrolyte. This top surface was examined in "as-received" condition and was not polished. The second sample enabled observation of the "cross-section" of the in-service plate. The cross-section sample was cold mounted in a resin and polished for microstructure evaluation using standard metallographic techniques [56] to a surface finish of 0.05µm. The cross-section was analyzed to study the elements constituting the corrosion products as well as the evolution of the corrosion products with respect to the bulk (i.e., interior) of the AZ31 electrode.

iii. Corroded AZ31

Polished samples of the virgin AZ31 plate were used to carry out various corrosion tests. After completing the corrosion tests, the surfaces of the corroded samples were examined for the initiation and growth of corrosion products. Samples were examined after each of the corrosion tests as follows:

a. *Samples examined after Immersion tests*

Sample I (Identifiers: "electrolyte type", "duration of immersion in days") – Corroded AZ31 samples examined after immersion tests in a specific electrolyte for a specific duration of time. For example, Sample I (1, 10) was immersed in Electrolyte #1 for a duration of 10 days.

b. *Samples examined after Tafel tests*

Sample T (Identifier: "electrolyte type") – Corroded AZ31 samples examined after the completion of a Tafel test in a specific electrolyte. For example, Sample T (1) was exposed to Electrolyte #1 during a Tafel test.

c. *Samples examined after EIS tests*

Sample E – Corroded AZ31 samples examined after the completion of an EIS test in a specific electrolyte. For example, Sample E (1) was exposed to Electrolyte #1 during EIS testing.

3.1. Sample preparation for corrosion tests

The virgin AZ31 plate was cut into rectangular samples (15 mm x 10 mm) using a vertical band saw and polished following standard metallographic techniques with SiC papers (from 120 grit to 600 grit), followed by polishing with diamond compounds (9 μm to 1 μm), as summarized in Table 3.2. A Mark V Lab manual polishing machine was used for manual polishing, as shown in Figure 3.3(a). After each polishing step, the samples were ultrasonically washed in acetone. The final polish was achieved with a 0.05 μm colloidal alumina. Figure 3.3(b) shows a macroscopic image of a polished AZ31 sample.

Table 3.2: Polishing procedure for AZ31 samples.

Step #	Polishing medium	Grit size / size of particles	Duration (Seconds)	Lubricating medium
1	Silicon Carbide paper	120	120	Distilled water
2	Silicon Carbide paper	240	100	Distilled water
4	Silicon Carbide paper	600	60	Distilled water
5	Diamond paste	9 μm	40	Diamond extender
6	Diamond paste	6 μm	30	Diamond extender
7	Diamond paste	3 μm	20	Diamond extender
8	Diamond paste	1 μm	15	Diamond extender
9	Colloidal Alumina	0.05 μm	10	Diamond extender

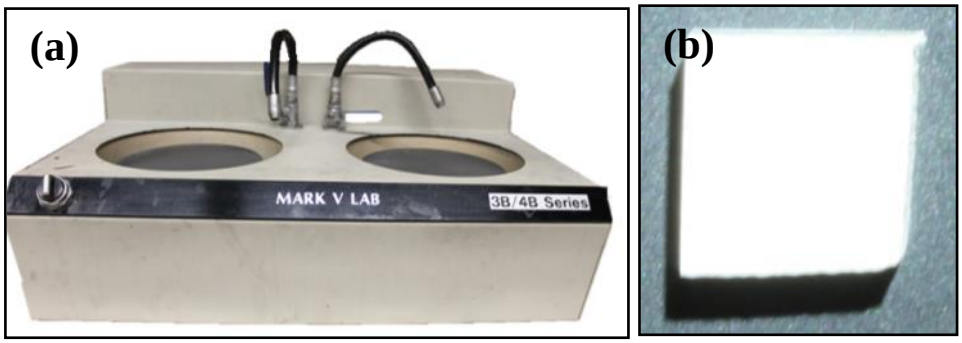

Figure 3.3: Polishing of metallographic samples: (a) Mark V lab manual polisher, (b) Polished AZ31 sample.

3.2. Corrosion testing

Corrosion testing was performed at the University of British Columbia, Okanagan. Immersion tests and electrochemical tests were performed with a potentiostat in order to quantify and study the corrosion behavior of the AZ31 alloy.

3.2.1. Electrolyte preparation

Two different electrolytes were used to study the corrosion characteristics of the AZ31 alloy. The identification of the two electrolytes was as follows:

i. ***Electrolyte #1:*** 45 wt% potassium hydroxide (KOH) electrolyte

ii. ***Electrolyte #2:*** 45 wt% KOH + 2 wt% sodium silicate (Na_2SiO_3) electrolyte

In order to prepare the 45 wt% KOH electrolyte, 45 g of KOH crystal pellets obtained from Fisher Scientific (Product # 1310-58-3) were added to 100 ml of Reverse Osmosis (RO) water. For preparation of KOH electrolyte with Na_2SiO_3 addition, 2 wt% Na_2SiO_3 solution obtained from Fisher Scientific (Product # 7732-18-5) was added to 98 ml of 45 wt % KOH solution.

3.2.2. Immersion tests

The edges of the sectioned and polished AZ31 samples were wrapped with a Teflon tape, to ensure that only the rectangular surface of the sample was exposed to the electrolyte, as seen in Figure 3.4(a). The samples were then immersed in a bottle with 100 ml of freshly prepared electrolyte, as seen in Figure 3.4(b). The electrolytes were maintained at standard room temperature and pressure (25° C and 1 atm).

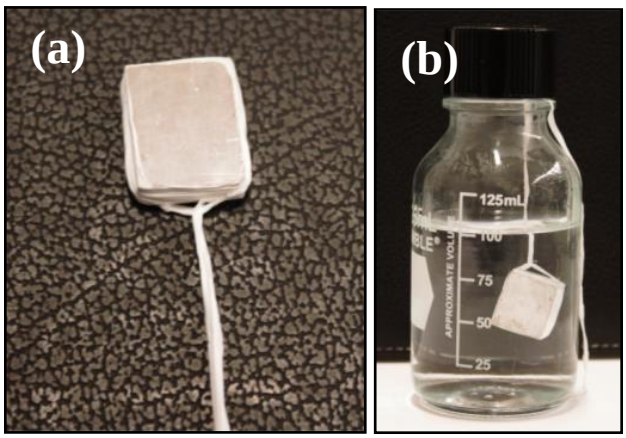

Figure 3.4: Immersion test set-up: (a) Sample prior to immersion test, (b) Suspended sample.

Two samples of polished virgin AZ31 plate were immersed at the same time in respective electrolytes for a total duration of 20 days. After the first 10 days of immersion, the samples were removed from the electrolyte and examined under the SEM without cleaning the corrosion products. Samples were then re-immersed in the electrolyte for additional 10 days. After 20 days (total), the samples were removed from the electrolyte and stored in a vacuum desiccator. A total of four samples were observed after immersion tests as follows:

i. Sample I (1,10) in Electrolyte #1 immersed for 10 days
ii. Sample I (2,10) in Electrolyte #2 immersed for 10 days
iii. Sample I (1,20) in Electrolyte #1 immersed for 20 days
iv. Sample I (2,20) in Electrolyte #2 immersed for 20 days

SEM analysis of the sample's surface and the cross-section was performed. Figure 3.5 shows these two surfaces. The cross-section sample was prepared by wrapping the corroded AZ31 plate with Teflon tape. This was done to ensure that corrosion products remained intact on the AZ31 substrate. After cutting a slice of the AZ31 plate the sample was cold mounted in a resin. The sample was then polished to yield a 0.05µm surface finish using standard metallographic techniques. Before SEM examination, the samples were coated with a platinum-

palladium coating (10 nm thick) to ensure the surface was conductive. Two repeats were performed for these experiments to maintain statistical validity of the experiments.

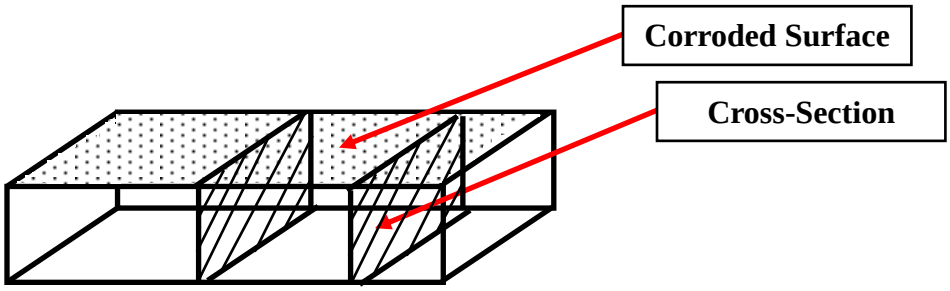

Figure 3.5: Surface and cross-section of samples examined after an immersion test.

After 20 days of immersion, the used liquid electrolyte was filtered through a paper filter in order to retain the precipitates or residuals, which were left undissolved in the electrolyte after the immersion test. A small section of the filter paper was cut and placed in the SEM microscope for imaging and chemical analysis. Also, corrosion products from the filter paper were stuck to a stub with adhesive carbon tape to perform SEM-EDS analysis.

3.2.3. Electrochemical studies

Tafel analysis and Electrochemical Impedance Spectroscopy (EIS) were performed using a Parstat 4000 potentiostat connected to a P.A.R. flat cell (model K0235) were used for all electrochemical studies. Figure 3.6 shows the image of the PARSTAT 4000 potentiostat. Versa Studio software was used to collect data points and to operate the potentiostat.

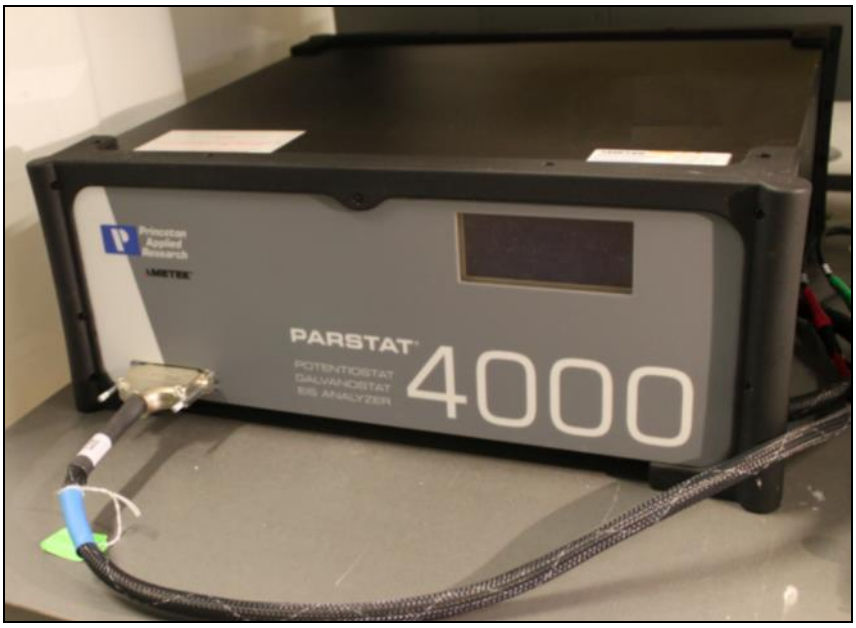

Figure 3.6: PARSTAT 4000 potentiostat.

The area of exposure of the AZ31 sample in the flat cell was 1 cm^2. Experiments were performed using a standard three electrode configuration (Figure 3.7) with Ag/AgCl saturated with KCl as the reference electrode. The electrode potential of the Ag/AgCl reference electrode was 0.197V with respect to Standard Hydrogen Electrode (SHE), and was constant throughout the experiments. A platinum wire mesh was used as the counter electrode. The counter electrode was present to provide a path for the current to flow and make a complete circuit.

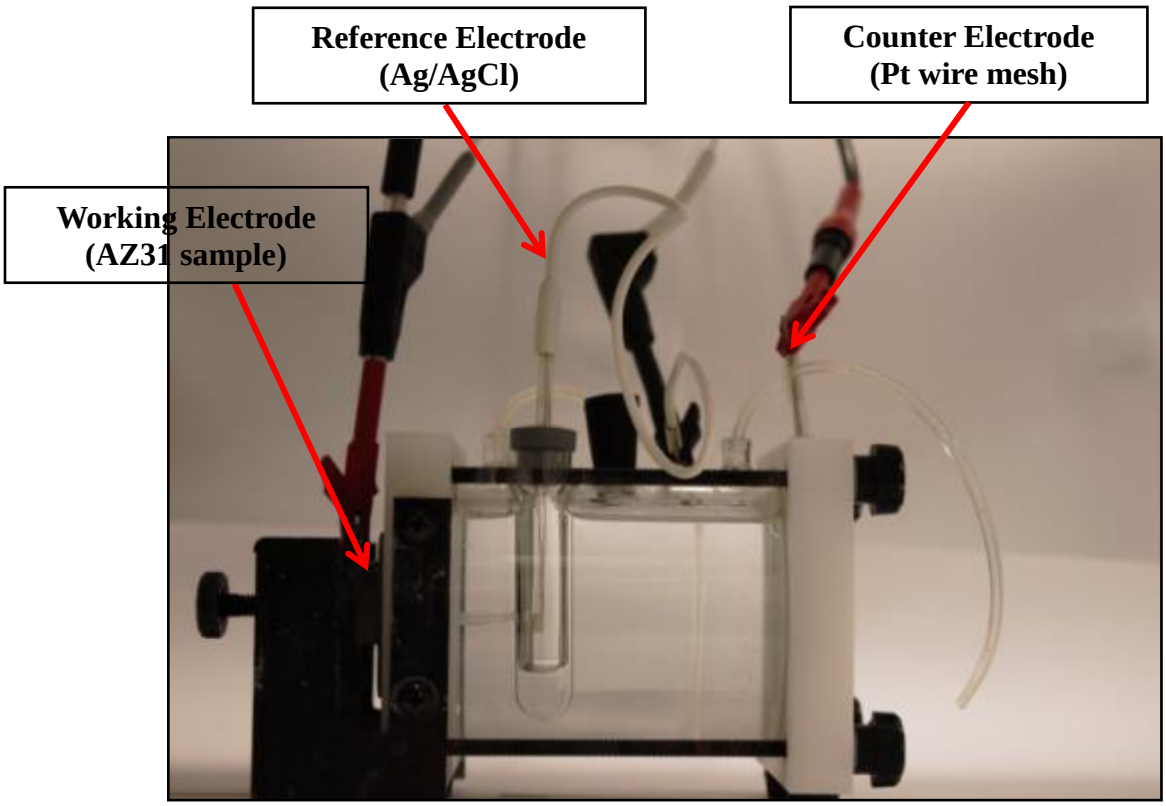

Figure 3.7: Standard three-electrode configuration used for electrochemical experiments.

The details of the EIS experimental set-up are provided in Figure 3.8 as a screenshot from the VersaStudio software, where the type of reference electrode and the working electrode were specified. Also, the area of sample exposed to the electrolyte was entered, in order to allow the software to directly calculate the value of the corrosion rate.

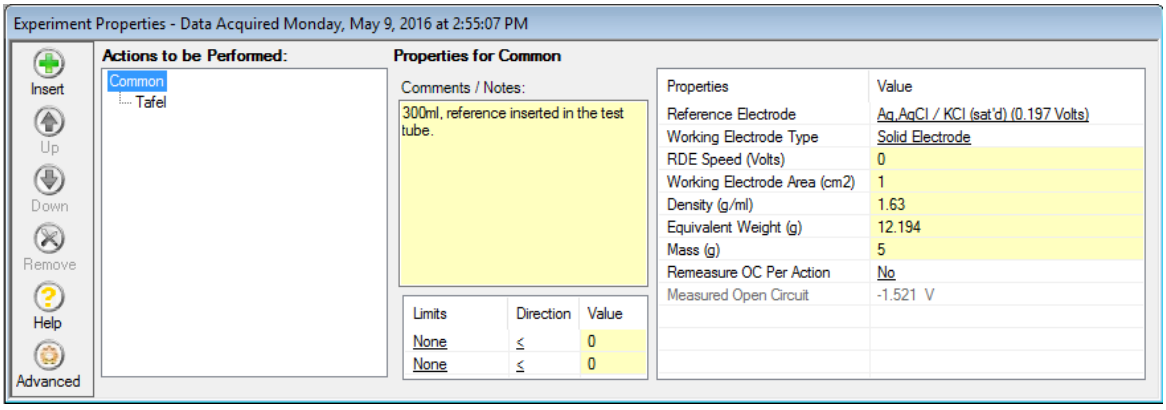

Figure 3.8: VersaStudio basic experimental set-up.

3.2.3.1. Tafel polarization

A polished sample of the virgin AZ31 plate was cleaned with acetone prior to a corrosion test. The sample was then placed in the flat cell and no external potential was applied for 15 minutes. Open Circuit Potential (OCP) was stabilized so that a stable layer of corrosion products formed before the electrochemical experiment was started. For Tafel analysis, the applied potential was varied from -0.3 to 1.2 mV with respect to the OCP. The scan rate was fixed to a value of 0.2 mV/sec, as outlined in Figure 3.9.

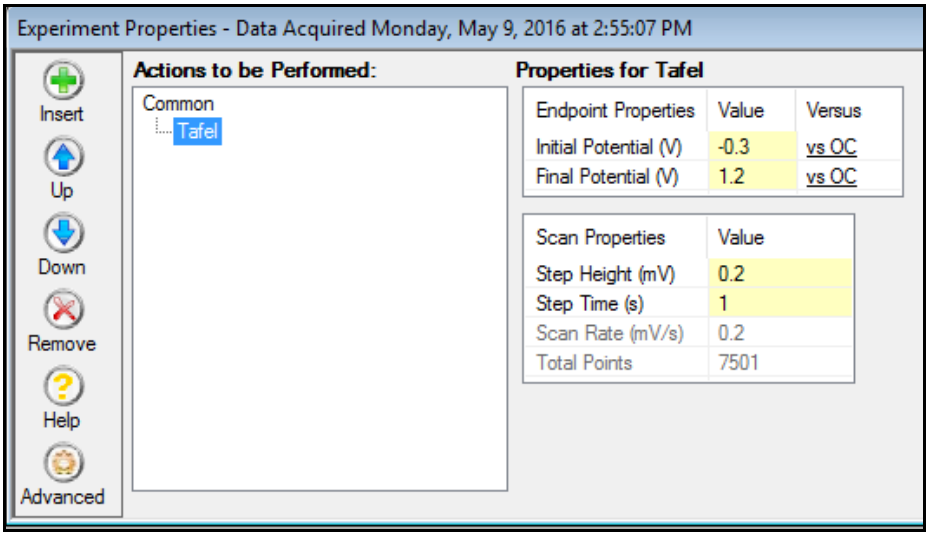

Figure 3.9: Experimental set-up for Tafel analysis.

Once the Tafel polarization experiment was concluded, a plot of the applied potential vs. the logarithmic value of the measured current was generated. Extrapolating the anodic and cathodic curves yielded the value of the corrosion current density (measured in $\mu A/cm^2$), as illustrated in Figure 3.10. The corrosion current was determined from tangents drawn on the polarization curve seen in Figure 3.10. The Tafel experiments were repeated two times for each sample and electrolyte to ensure statistical validity of the results.

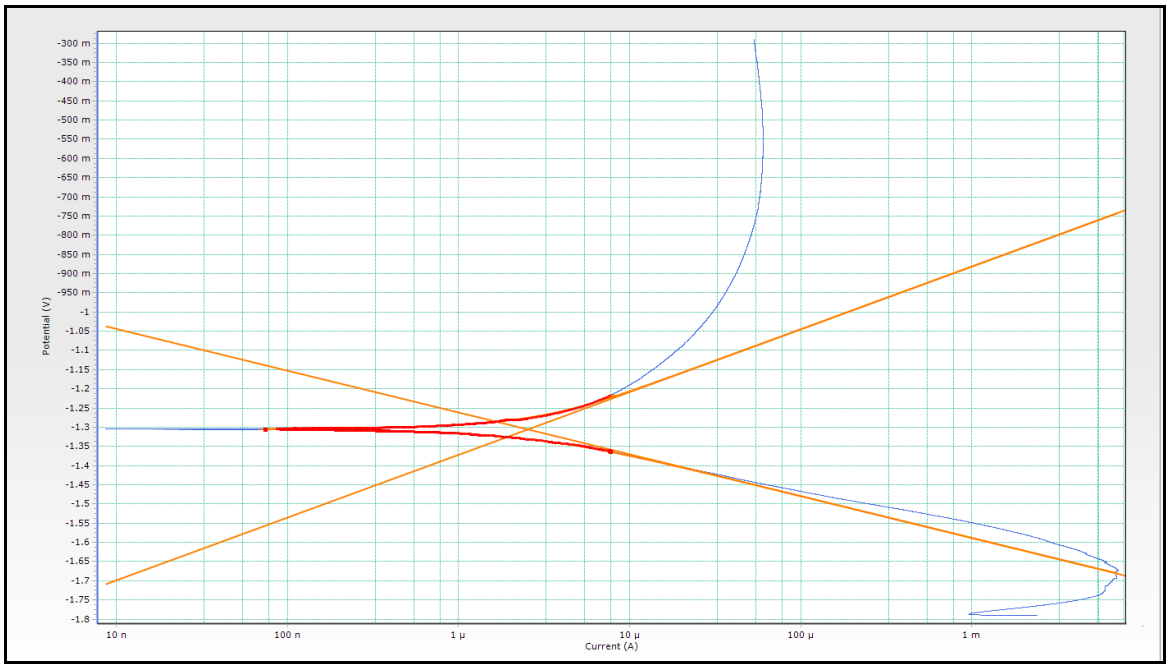

Figure 3.10: Extrapolation of potentiodynamic polarization curves.

3.2.3.2. Electrochemical impedance spectroscopy

EIS was performed using the standard three electrode configuration. The signal frequency ranged from 10,000 Hz to 0.01 Hz at a fixed amplitude of 10 mV. Nyquist and Bode plots from the raw data were obtained by Versa Studio. The details of the EIS experimental set-up are included in Figure 3.11.

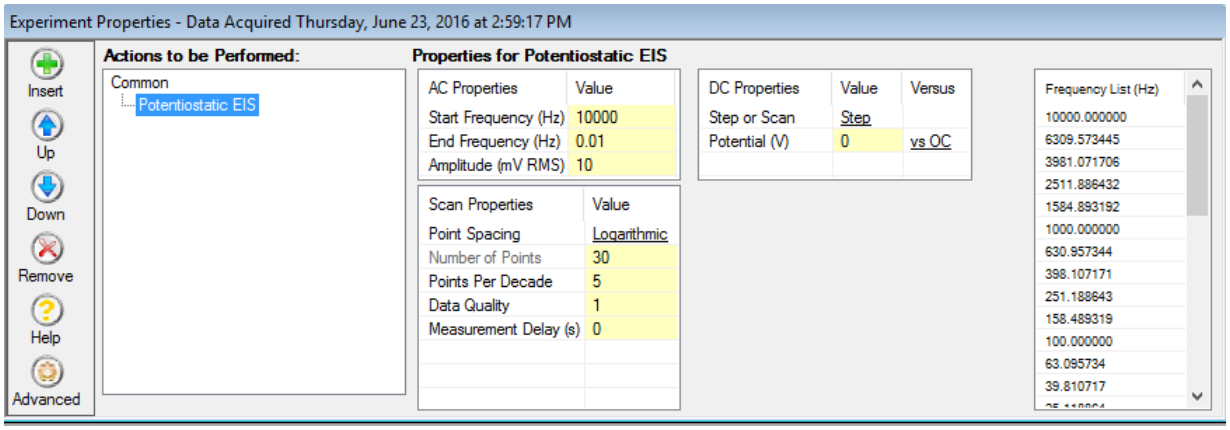

Figure 3.11: Experimental set-up for EIS test.

ZSimpWin software (EChem Software, Ann Arbor, USA) was used for curve fitting of the Nyquist and Bode plots. After appropriate model was selected, the electrochemical parameters were obtained from the software. A minimum of two repeats were performed for each of the sample and electrolyte combinations.

3.3. Characterization of AZ31 samples

The AZ31 samples before and after corrosion testing were studied using diverse methods, including Scanning Electron Microscope (SEM), X-ray Diffraction (XRD), Transmission Electron Microscope (TEM) and Inductively Coupled Plasma-Optical Emission Spectroscope (ICP-OES). After immersion testing, the corroded surface was analyzed using XRD and SEM analyses. ICP-OES technique was used to compute the composition of used Electrolyte #1 and Electrolyte #2 after 20 days of immersion testing.

3.3.1. SEM analysis

Scanning Electron Microscopy was performed with a Tescan Mira^3 XMU field emission gun SEM. An Oxford Aztec Energy Dispersive X-ray Spectroscopy (EDS) system was used to determine the chemical composition of the AZ31 samples.

Corroded samples immersed in Electrolyte #1 and Electrolyte #2 were analyzed after 10 and 20 days of immersion (Sample I (1, 10), Sample I (1, 20), Sample I (2, 10), Sample I (2, 20)). SEM analysis was also performed for the in-service AZ31 electrode surface and cross-section.

3.3.2. XRD analysis

XRD analysis of the virgin AZ31 was performed using a Panalytical X-ray diffractometer (Figure 3.12) with a Cu K-α radiation at the Indian Institute of Technology, Chennai, India. Scans were performed from 10° to 90° with a step size 0.008° and a time per step of 40 seconds. Both virgin and corroded AZ31 samples (Sample I (1, 20), Sample I (2, 20)) were analyzed.

Figure 3.12: X-ray Diffractometer at IIT Chennai, India.

Indexing of diffraction patterns was carried out using the JCPDS (Joint Committee on Powder Diffraction Standards) and ICSD (Inorganic Crystal Structure Database) databases in X'Pert HighScore software.

3.3.3. TEM analysis

A FEI Tecnai T20 was used for characterization of the precipitates in the virgin AZ31 plate. All TEM sample preparation and analysis was performed at the Indian Institute of Technology,

Chennai, India. TEM samples were prepared by dimpling a thin slice of virgin AZ31 alloy (about 400μm thick). Once the thickness reached about 80 μm, ion milling was performed (firing Argon ions on the surface of the sample) to bring the sample to electron transparent thickness.

TEM analysis was performed with the goal of determining the crystal structure of the precipitates, since these could not be identified using any other technique available. Only virgin AZ31 sample was analyzed using TEM, since the corrosion products would spall off during the conventional sample preparation methods used.

3.4. ICP-OES analysis

All electrolytes used for immersion testing were analyzed using ICP-OES technique using a Perkin Elmer Optima 5300 DV. Due to the absence of available standards at IIT Madras, India, In, K, Ca and Na could not be detected in the electrolytes.

Chapter 4: RESULTS AND DISCUSSIONS

This chapter provides an in-depth analysis of the results generated in this research. First, the characterization of the virgin AZ31 alloy and in-service AZ31 electrode material is discussed. Then, the results of immersion, as well as electrochemical testing are presented. The chapter concludes with a proposed mechanism on the possible degradation of AZ31 in highly alkaline environment.

4.1. Characterization of virgin and in-service AZ31 alloy

The raw materials including virgin AZ31 plate and in-service AZ31 electrode were examined using SEM-EDS to determine any compositional variations in the AZ31 alloy due to service conditions.

4.1.1. Virgin AZ31 plate

The virgin AZ31 plate was polished to 0.05 µm surface finish using standard metallographic techniques. SEM-EDS analysis was performed on the top surface, as well as on the cross-section.

4.1.1.1. Top surface

Figure 4.1 shows the top surface of the polished virgin AZ31 plate. The microstructure consisted of Mg solid solution (α-Mg) and white precipitates. The precipitates were dispersed across the entire sample and had a particle size in the range of 1 – 30 µm.

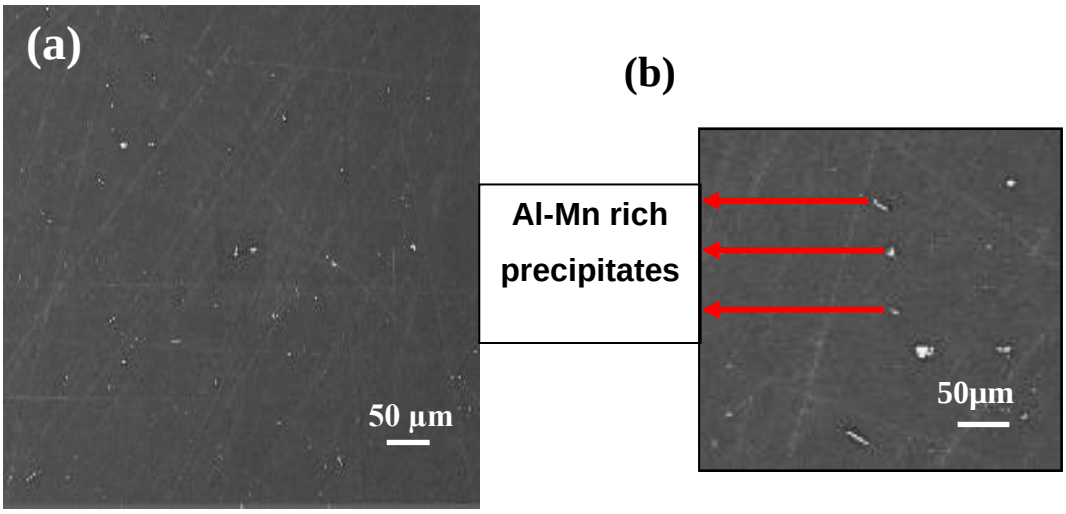

Figure 4.1: General microstructure of virgin AZ31 top surface: (a) Low magnification, (b) Al-Mn rich precipitates.

4.1.1.2. Cross section

The cross-section of the AZ31 plate is shown in Figure 4.2**.** Similarly as observed for the top surface, the cross section of the plate contained polygonal precipitates, which appeared to be homogeneously dispersed throughout the plate thickness. As seen from Figure 4.2(b), some of the precipitates fragmented (e.g., due to the rolling process during the plate manufacture). [31] Both the top surface and the cross-section compositions obtained from SEM-EDS analysis are included in Table 4.1.

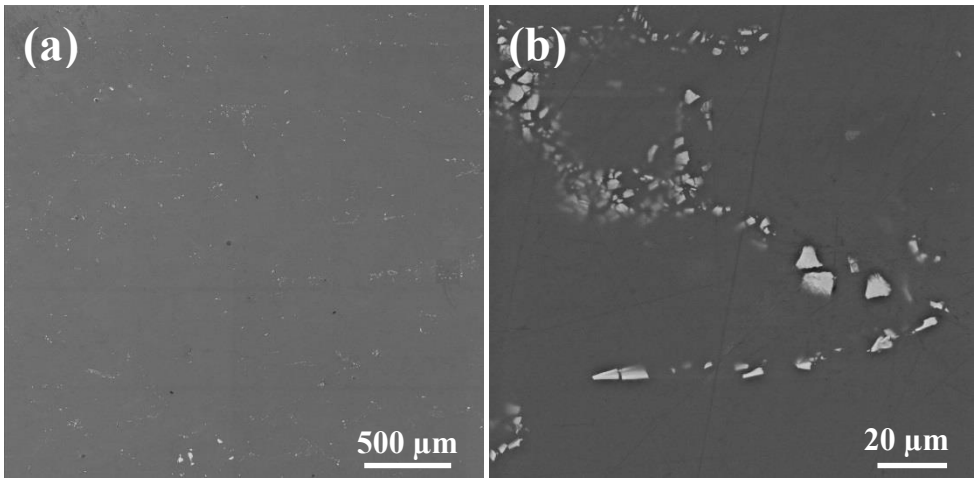

Figure 4.2: Cross section of virgin AZ31 plate: (a) General microstructure, (b) Al-Mn precipitates.

Table 4.1: Composition of constituents of virgin AZ31 plate using SEM-EDS (wt%)*.

Surface	Element	O	Na	Mg	Al	Mn	Ca	Fe	Ni	Cu	Zn
Top surface	***White precipitates***	0.00 ±0.00	0.00 ±0.00	10.92 ±0.02	39.98 ±1.86	48.53 ±4.03	0.35 ±0.01	0.09 ±0.14	0.02 ±0.20	0.05 ±0.05	0.06 ±0.20
	Matrix	0.31 ±0.26	0.30 ±0.25	94.88 ±0.59	2.99 ±0.87	0.20 ±0.05	0.90 ±0.04	0.08 ±0.11	0.01 ±0.30	0.03 ±0.04	0.30 ±0.11
Cross-section	***White precipitates***	1.50 ±0.79	0.00 ±0.00	4.82 ±0.29	36.79 ±5.28	56.31 ±7.82	0.00 ±0.00	0.34 ±0.16	0.00 ±0.00	0.10 ±0.05	0.14 ±0.04
	Matrix	0.65 ±0.03	0.32 ±0.07	94.53 ±0.70	2.91 ±0.01	0.30 ±0.37	0.02 ±0.04	0.03 ±0.08	0.00 ±0.00	0.02 ±0.00	1.22 ±0.10

*± *indicates the error in measurement.*

The chemistry of the top surface and the cross-section of the virgin AZ31 plate was relatively consistent. The chemical analysis of the α-Mg matrix confirmed that the virgin AZ31 alloy's composition was in agreement with American Society for Metals (ASM). [29]

The alloy also contained traces of Ni, Fe and Cu in trace quantities. Presence of these trace elements could have originated from the manufacturing process (e.g., by contamination from the hot rolling operation of the AZ31 plate). In general, however, these elements are undesirable due to their role in accelerating corrosion of magnesium alloys.

The chemical analysis of the white precipitates revealed that they were rich in Al and Mn, as seen in Table 4.1. Presence of Al-Mn-rich precipitates in AZ31 alloy system was reported in the literature. [31] [41] A trace of Fe was also present; however, it was not consistently detected in all of the precipitates. Presence of these Al-Mn precipitates is also consistent with the phase diagrams discussed in Section 2.4.1.

Following initial characterization with SEM, the sample was etched with 10% HF solution to enable a further characterization of the Al-Mn precipitates. It was observed that some of the Al-Mn precipitates were preferentially etched and fell out of the matrix during HF etching,

as seen in Figure 4.3. The shape and size of the resulting pits left behind by the dislodged Al-Mn precipitates was similar in dimension and geometry to the Al-Mn precipitates in the virgin AZ31, suggesting that these precipitates were chemically active in acidic environments and readily fell out of the matrix.

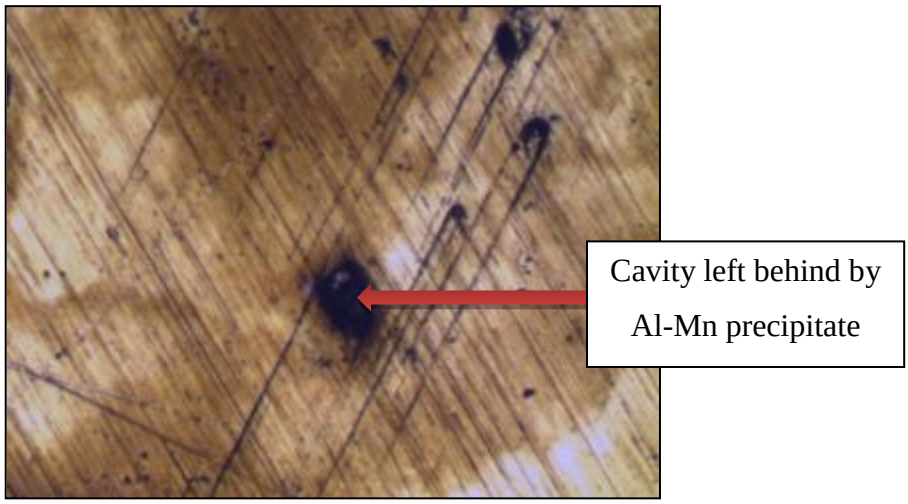

Figure 4.3: Cavities in etched top surface of virgin AZ31 plate (100x).

4.1.1.3. TEM analysis

The Al-Mn precipitates in the virgin AZ31 matrix were studied using a transmission electron microscope (TEM) and selected area diffraction technique in order to determine the precise stoichiometry of the precipitates. Figure 4.4 shows the TEM images as well as Selected Area Diffraction Pattern (SADP) obtained from the matrix and the Al-Mn precipitate.

Figure 4.4(a) shows a representative bright field image of the precipitates. The TEM micrographs reveal that the precipitates were well attached to the matrix. However, they were brittle and readily fractured. Figures 4.4(b) and (c) show the diffraction patterns for the precipitates and the matrix, respectively.

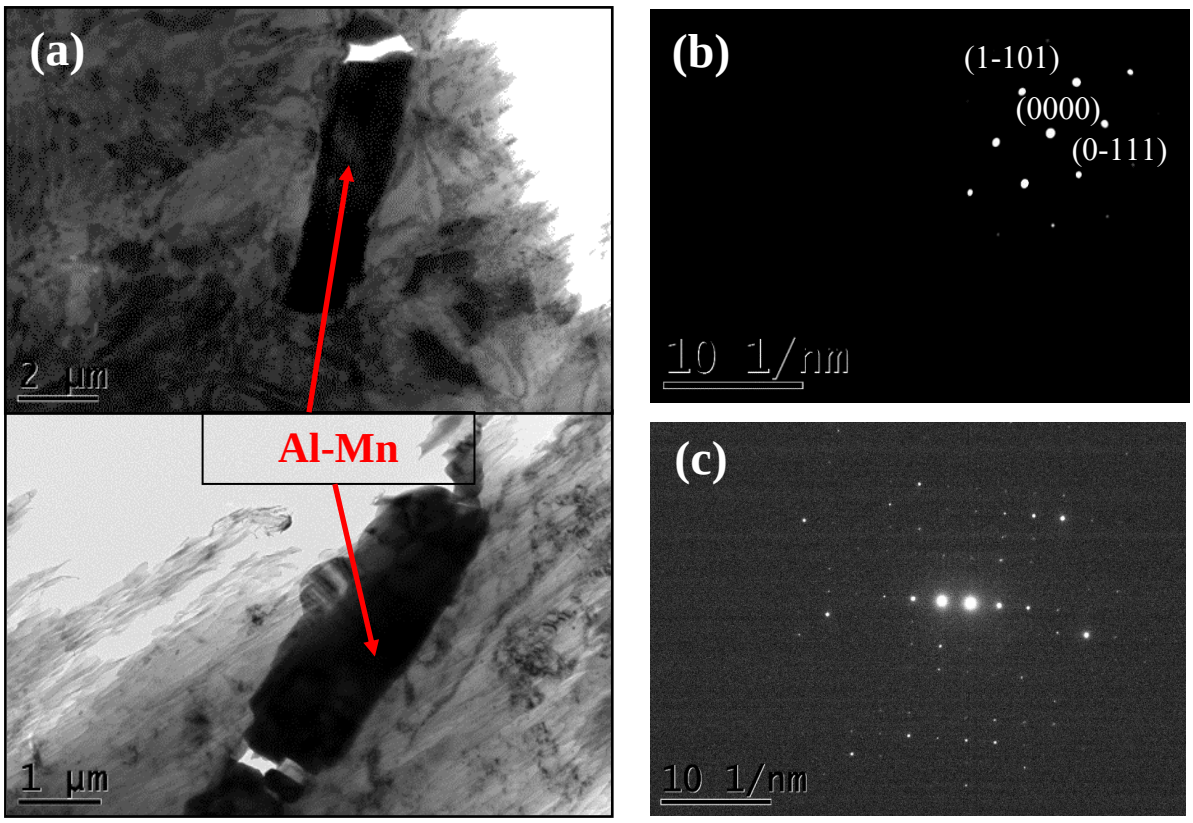

Figure 4.4: TEM analysis of Al-Mn precipitates: (a) Al-Mn precipitate, (b) SADP of AZ31 matrix, (c) SADP of Al-Mn precipitate obtained from TEM analysis.

The distance between two diffraction points in the matrix SADP was 619.643 units and 622.535 units, yielding a ratio of 0.995. The matching set of planes for this ratio was (0-111) and (1-101). These planes were indexed, with indices in Figure 4.4(b). Indexing was done with the help of standard available indexing patterns for hexagonal symmetry of planes. [57] Interestingly the presence of impurities (Ni, Fe and Cu) did not affect the SADP, perhaps due to their low concentrations.

Once the matrix was evaluated, precipitate chemistry was determined via TEM-EDS analysis (Table 4.2). As expected, the precipitates were rich in Al and Mn, with a trace amount of Fe.

Table 4.2: Composition of Al-Mn precipitate from TEM-EDS analysis (wt%)*.

Element	Al	Mn	Fe
Composition	45.6±2.49	53.5±5.28	0.90±0.14

*± *indicates the error in measurement.*

A representative SADP obtained from the Al-Mn precipitates is shown in Figure 4.4(c). The SADP was consistent to those found in the literature for the Al_8Mn_5 phase in the Al-Mn phase diagram (Figure 2.5). [58] The ratio of concentration of Al to Mn obtained from the TEM-EDS analysis (~1.68) was similar to the ratio of Al_8Mn_5 phase (1.6). The crystal structure of this phase was rhombohedral, [59] as was verified by the two fold symmetry of planes seen in Figure 4.4(c). However, indexing of the precipitate patterns was challenging due to signal interference with the matrix, resulting in the SADP being a combination of DP's from the matrix and the precipitates. Similar challenges were reported in published literature as well. [58] [59] [60]

Figure 4.5 shows an XRD diffraction pattern obtained from the virgin AZ31 plate. The most intense peaks correspond to the Mg matrix solid solution. Also, $Mg_{17}Al_{12}$ β-phase as well as small peaks corresponding to Al_8Mn_5 phase were detected. Thus, the XRD results further confirmed the stoichiometry of the Al-Mn precipitates as Al_8Mn_5.

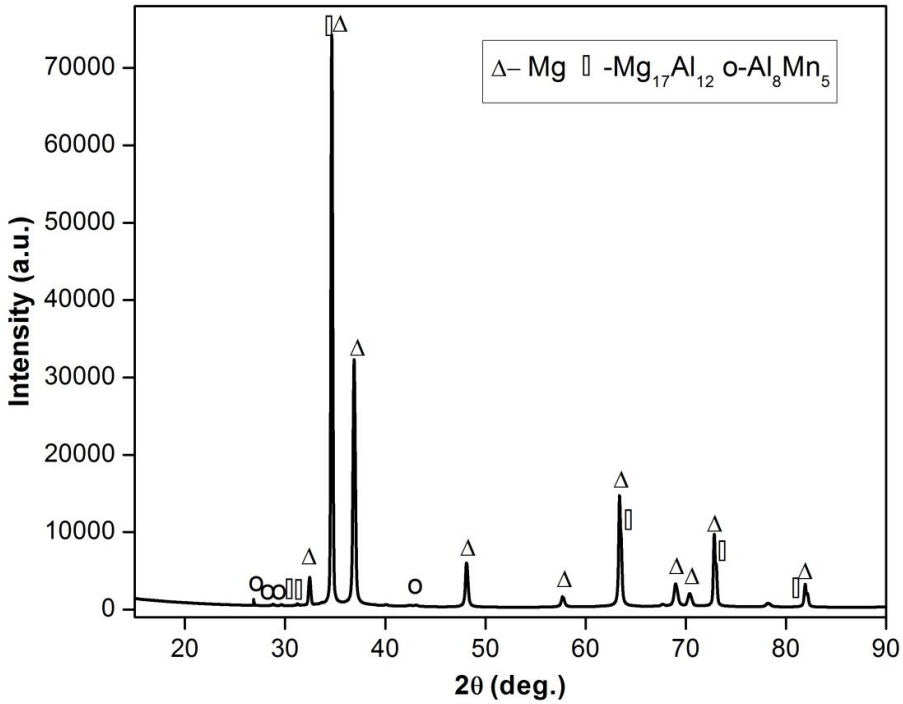

Figure 4.5: XRD analysis of virgin AZ31 plate.

4.1.2. KOH crystals

As will be discussed in subsequent sections, some foreign elements were detected in the corrosion products and in the electrolyte. In an effort to examine the source of these elements, the composition and purity of the KOH crystals used to prepare the electrolyte was examined and the results are included in Table 4.3.

Table 4.3: Composition of KOH crystals used (wt%).

Element	K	O
Composition	55.27	44.73

As seen in Table 4.3, the crystals contained K and O, as expected, while Hydrogen could not be detected with the SEM-EDS system. No other impurities were detected in the KOH crystals.

4.1.3. In-service AZ31 electrode

The exposed area of the in-service AZ31 electrode had visible signs of pitting corrosion (Figure 4.6). Both top surface and cross-section were analyzed to understand the structure of the corrosion products in the in-service AZ31 electrode.

4.1.3.1. In-Service AZ31 electrode - Top surface

Figure 4.6 shows a representative SEM micrograph of the top surface of the in-service AZ31 electrode, which was exposed to the fuel cell electrolyte. The surface consisted of dark gray regions with corrosion pits. The corrosion products in the pits had irregular and varying morphologies. An area scan was performed across the corrosion products on a pit to obtain its average composition, and the results are provided in Table 4.4.

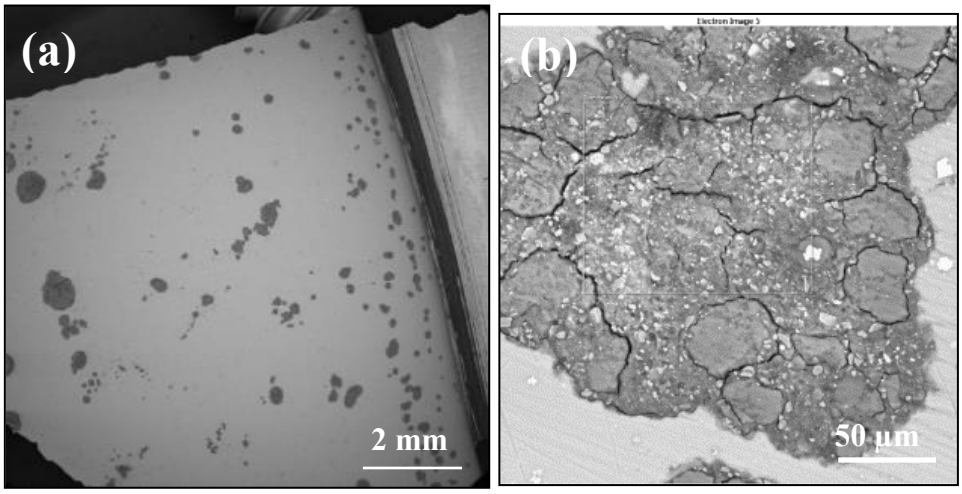

Figure 4.6: SEM micrograph of in-service AZ31 electrode: (a) General surface overview, (b) Site for area scan of a corrosion pit.

Table 4.4: Average composition of corrosion products in a pit of in-service AZ31 electrode (wt%) *.

Element	O	Na	Mg	Al	Si	K	Ca	Mn	Fe	Ni	Cu	Zn
Composition	48.84 ±2.27	0.48 ±0.21	37.15 ±0.11	10.21 ±1.06	0.63 ±0.01	0.40 ±0.02	0.14 ±0.06	0.31 ±0.03	0.06 ±0.06	0.70 ±0.51	0.02 ±0.03	1.07 ±0.06

*± *indicates the error in measurement.*

The corrosion pits contained large quantities of oxygen, aluminum and magnesium, thus suggesting a potential formation of a magnesium oxide or an aluminum oxide. However, additional deleterious elements were detected. The pit contained potassium, which likely was retained from an electrolyte residue. Also, traces of iron were present (~0.06 wt%) and possibly originated from the dissolution of the Al-Mn-Fe precipitates. Also, it was likely that oxides/hydroxides of Ni, as well as silicates of Mg and Ca were also present in the corrosion products. This was verified by the XRD analysis of Sample I (2, 20). As marked in Figure 4.7, three distinct areas were identified:

i. "*clean" corroded region,*
ii. "*dirty" corroded region, and*
iii. *white precipitates on corroded region*

The chemical compositions of the "clean" and "corroded" regions, as well as the white precipitates are summarized in Table 4.5.

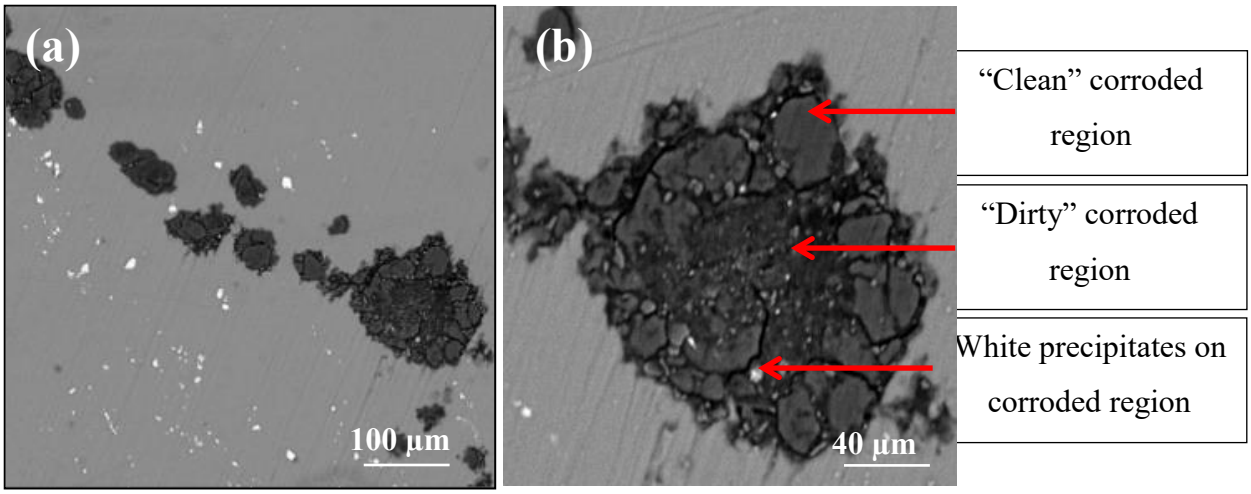

Figure 4.7: Surface of in-service AZ31 electrode revealing "clean" and "dirty" corroded regions: (a) Low magnification and (b) High magnification view.

Table 4.5: Chemical analysis of corrosion products on in-service AZ31 electrode (in wt%)*.

Element	O	Na	Mg	Al	K	Ca	Mn	Fe	Ni	Cu	Zn
"Dirty" corroded region	47.25 ±4.14	0.46 ±0.25	28.32 ±2.52	21.71 ±3.42	0.39 ±0.19	0.07 ±0.06	0.09 ±0.04	0.02 ±0.02	0.54 ±0.42	0.03 ±0.05	1.12 ±0.68
"Clean" corroded region	63.73 ±0.14	0.42 ±0.05	29.16 ±0.49	4.96 ±0.50	0.08 ±0.02	0.02 ±0.01	0.14 ±0.13	0.03 ±0.02	0.00 ±0.00	0.01 ±0.01	1.45 ±0.10
White precipitates in corroded region	37.79 ±2.63	1.17 ±0.58	19.52 ±3.76	2.81 ±0.21	8.80 ±2.28	0.18 ±0.10	0.37 ±0.02	19.28 ±5.78	0.23 ±0.03	0.00 ±0.02	9.86 ±5.78

**± indicates the error in measurement.*

The "clean" corroded region was found to be rich in oxygen (~64 wt%), suggesting the presence of oxides/hydroxides in this area, while the "dirty" corroded region was rich in aluminum (~22 wt%) and had a reduced amount of oxygen (~47 wt%) when compared to the clean corroded region. A higher oxygen content in the "clean" corroded region may be due to presence of manganese oxide resulting from dissociation of the Al-Mn or Al-Mn-Fe precipitates. It has been reported in the literature that the Al-Mn precipitate dissolution enables the formation of Mn_3O_4. [61]

The high Al content in the "dirty" corroded regions may be due to the diffusion of Al towards the surface (after being de-alloyed from Al-Mn or Al-Mn-Fe precipitate) and subsequent formation of an $Al(OH)_3$ or Al_2O_3. [62] [63] [64] Equation 10 describes the chemical reaction for the formation of $Al(OH)_3$. [63]

$$Al + 3OH^- \rightarrow Al(OH)_3 + 3\,e^- \quad \textbf{(10)}$$

A similar observation was made by Danaie *et al*. [64], who reported the presence of Al and O in certain areas of AM50 Mg alloy exposed to aqueous environments, where the areas initially contained Al-Mn rich precipitates prior to corrosion. Therefore, in the present work, the clean corroded regions were possibly sites rich in Al-Mn precipitate clusters.

In the present work, the Al-Mn precipitates also contained Fe (19 wt%) in some regions, which may have induced these precipitates to act as cathodic sites for micro galvanic corrosion in the alloy. [31] It is also possible that Fe^{2+} ions from the Al-Mn-Fe precipitates were reduced to elemental Fe due to cathodic reaction at these sites.

The results in Table 4.5 also suggest that Ni segregated in the "dirty" corroded region (0.54 wt%), while it was absent from the "clean" corroded region. Ni was found in appreciable amounts along the cross-section of the in-service AZ31 electrode.

The pits observed in Figure 4.7 appeared to be the "end" result of the pit formation process (i.e., the final effect of the corrosion process). As a result, the surface of the plate was examined at higher magnifications to seek out regions where the formation of the pits appeared to just begin. These initiation sites (or a pit at its early stage of formation) were examined in order to find elements contributing to the pit formation.

Figure 4.8 shows a suspected pit initiation site. A linescan was performed along the yellow line marked in Figure 4.8(a) and revealed that the pit initiated near a region rich in Al and

Mn (this region has been marked with a red circle in Figure 4.8). This evidence further supports the hypothesis that the Al-Mn precipitates may have contributed to the initiation of the pit. The region where the depth of the pit increased (this region has been marked with a blue circle in Figure 4.8) was rich in Na. This was possibly due to activity of electrolyte in this region. Na was present as an additive for the electrolyte used for the in-service AZ31 electrode. The SEM-EDS linescan shows that the variation of elements was gradual, suggesting that the element transport phenomenon was diffusion driven.

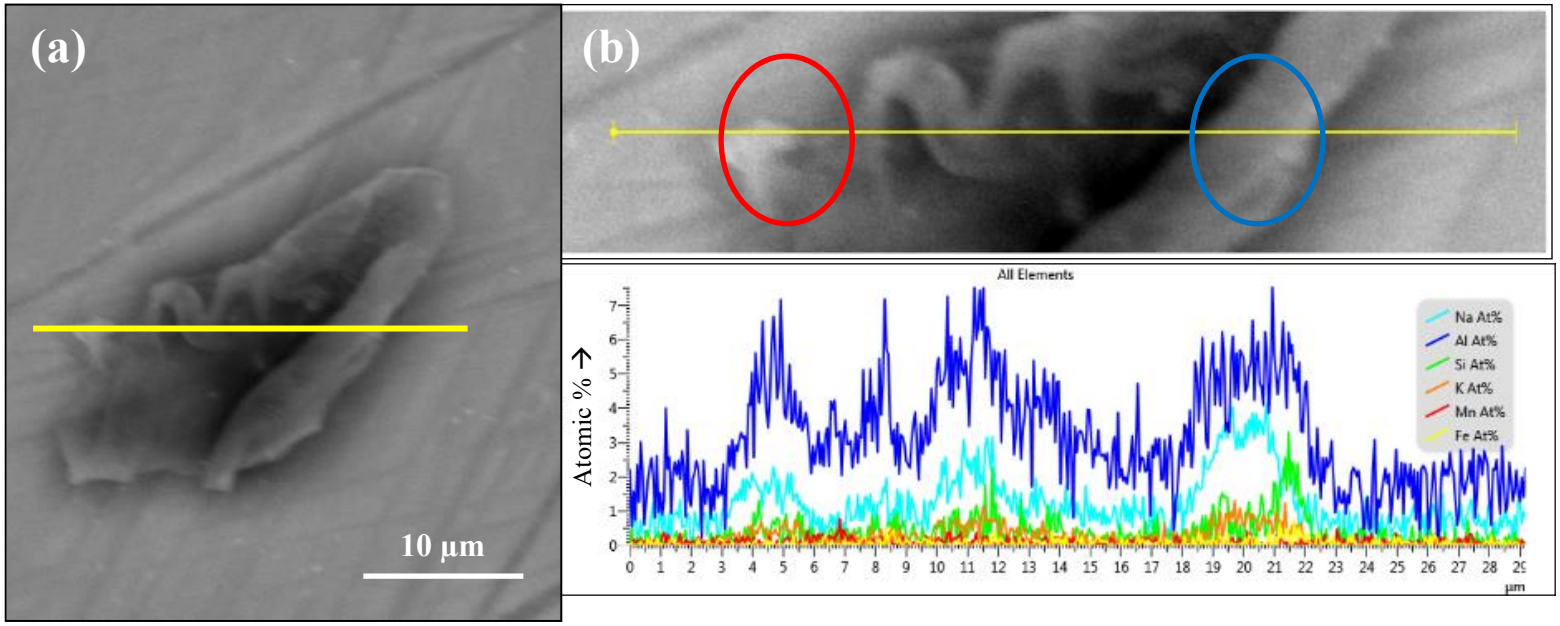

Figure 4.8: Pit initiation site in in-service AZ31: (a) Suspected pit initiation site on in-service AZ31 electrode, (b) Linescan results obtained from SEM-EDS analysis.

4.1.3.2. Cross-section - The cross section of the in-service electrode

The central region of the cross section of the in-service AZ31 electrode (i.e., mid-point through the thickness of the in-service AZ31 electrode) was analyzed to determine if there was a variation in composition with respect to the top surface which was exposed to the electrolyte. SEM image of the central region in Figure 4.9 shows the general microstructure of the cross-section. The chemical composition of central region in cross-section of the in-service plate is provided in Table 4.6. The SEM-EDS results suggest that the composition of the central region of the sample's cross section was consistent with the virgin AZ31 matrix as well as the Al-Mn precipitates (Table 4.1), respectively.

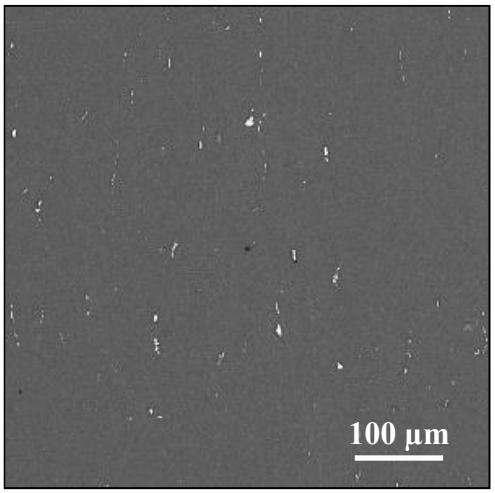

Figure 4.9: Central region of the cross section of in-service AZ31 electrode.

Table 4.6: Composition of the central region of the in-service AZ31 electrode (wt%)*.

Element	O	Na	Mg	Al	K	Ca	Mn	Fe	Ni	Cu	Zn
Matrix	1.12 ±0.29	0.27 ±0.05	93.88 ±0.39	3.31 ±0.23	0.00 ±0.00	0.02 ±0.03	0.18 ±0.14	0.00 ±0.00	0.00 ±0.00	0.05 ±0.07	1.16 ±0.08
Al-Mn precipitates	0.24 ±0.25	0.09 ±0.05	21.87 ±11.84	36.31 ±2.40	0.01 ±0.00	0.00 ±0.00	40.7 ±8.07	0.32 ±0.20	0.03 ±0.03	0.05 ±0.02	0.39 ±0.05

**± indicates the error in measurement.*

Observing the cross section of the specimen at a higher magnification revealed an interesting feature at the sample's edge exposed to the electrolyte. At this interface region, a narrow surface layer was observed, as seen in Figure 4.10 and Figure 4.11. Elemental mapping of the corrosion product layer revealed the presence of three separate sub-layers of elements adhering to the AZ31 material, as seen in Figure 4.12**.**

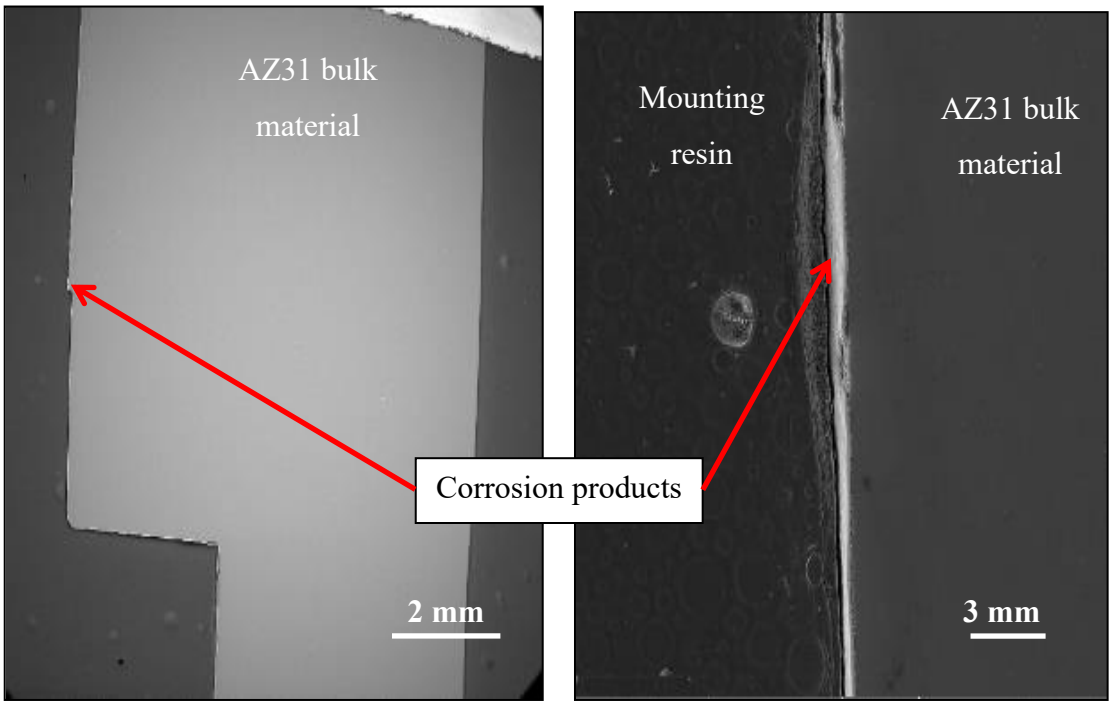

Figure 4.10: Cross-section of in-service AZ31 electrode.

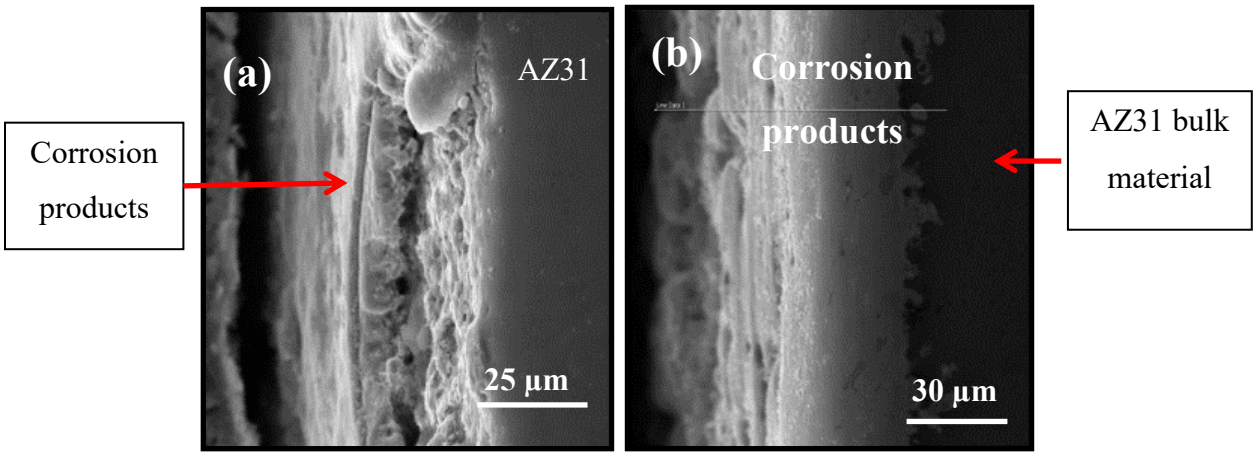

Figure 4.11: Corrosion products on the surface of in-service AZ31 electrode: (a) Location #1, (b) Location #2.

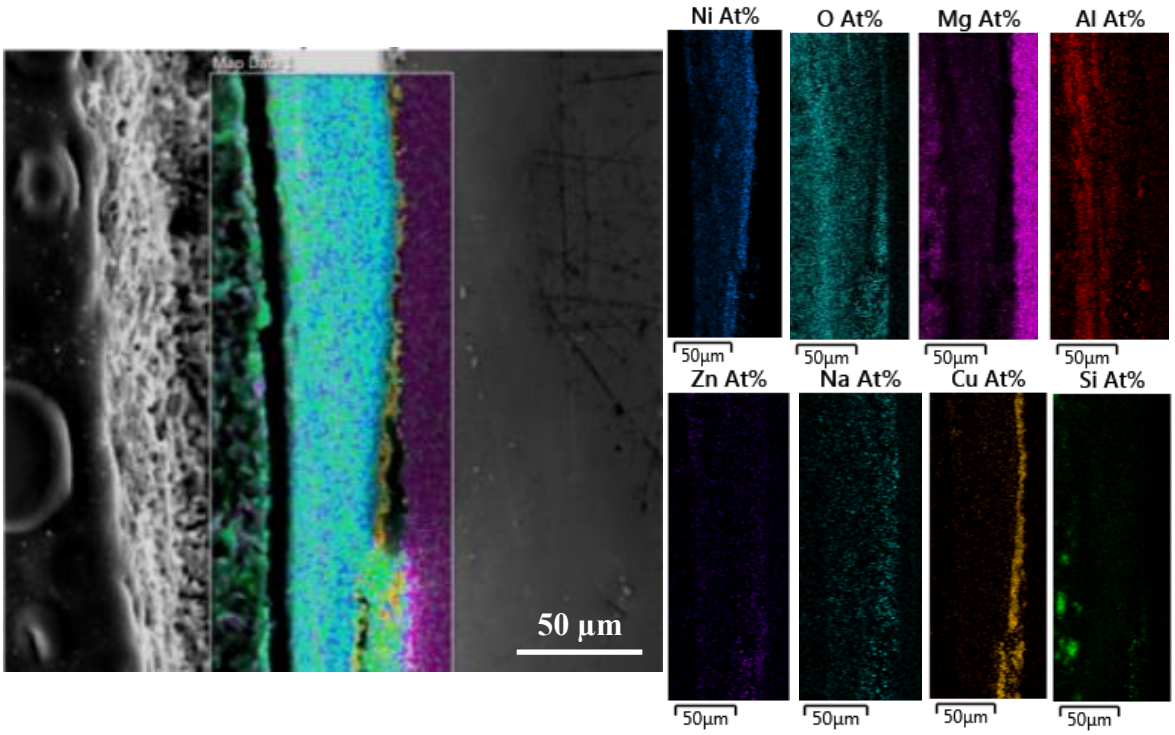

Figure 4.12: SEM-EDS mapping of corrosion products on in-service AZ31 electrode.

The SEM-EDS maps reveal the presence of a Cu layer in contact with the AZ31 substrate. This layer possibly formed due to the attack of the electrolyte on the Cu present as impurity in the virgin AZ31 plate. [25]

A second sub-layer consisting of Ni was detected to adhere to the corroded surface. This Ni sub-layer was formed possibly by the selective dissolution of Mg at the interface with the electrolyte. The dissolution of the matrix was verified by ICP-OES (Section 4.3), where an increase in Mg concentration in the electrolyte before and after an immersion test was detected.

Finally, an Al sub-layer was detected in the corrosion products. The Al layer was in direct contact with the electrolyte. Al was likely present due to the dissolution of the Al-Mn precipitates. After being dissociated from the precipitates, it may have diffused to the surface or dissolved in the electrolyte.

Mg was found to be present with Si in the corrosion products, and appeared to co-exist with the Ni-rich layer. This may have been the result of magnesium silicate layer formation on the surface of the sample. The silicate layer was also detected in XRD analysis of Sample I (2, 20). The possible reaction between magnesium and silicates is provided in Equation 11. [65]

$$2Mg^{2+}2SiO_3^{2-} \rightarrow Mg_2SiO_4 + SiO_2 \quad \textbf{(11)}$$

Figure 4.13 shows the detail of the cross-section of in-service AZ31 electrode ("resin" refers to the plastic resin used to hold the sample during metallographic polishing). A number of area scans were performed using SEM-EDS analysis to determine the quantitative composition of the corrosion products in the different regions shown. The results are provided in Table 4.7.

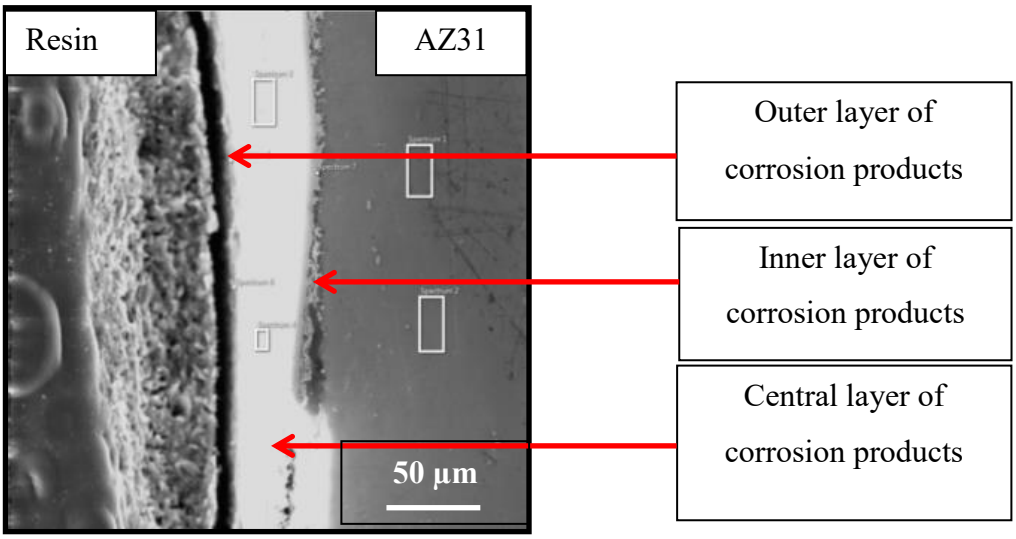

Figure 4.13: Area scans along the cross section of in-service AZ31 electrode.

Table 4.7: Composition of corrosion product layers on in-service AZ31 electrode (wt%) *.

Element	O	Na	Mg	Al	Si	K	Ca	Mn	Fe	Ni	Cu	Zn
Matrix	1.16 ±0.05	0.26 ±0.03	93.73 ±0.31	3.06 ±0.37	0.01 ±0.01	0.05 ±0.02	0.02 ±0.03	0.19 ±0.01	0.03 ±0.04	0.12 ±0.06	0.00 ±0.00	1.38 ±0.04
Inner corroded layer	12.62 ±1.67	0.74 ±0.04	45.86 ±3.40	0.80 ±0.06	0.04 ±0.13	0.12 ±0.01	0.01 ±0.00	0.07 ±0.01	0.00 ±0.00	1.70 ±0.71	35.50 ±0.07	2.54 ±0.89
Central corroded layer	10.89 ±3.49	0.14 ±0.15	15.83 ±3.00	7.50 ±2.06	1.75 ±0.83	0.03± 0.01	0.00 ±0.00	0.10 ±0.02	0.00 ±0.00	63.37 ±9.62	0.18 ±0.07	0.31 ±0.01
Outer corroded layer	30.73 ±6.93	0.27 ±0.08	16.8 ±4.74	24.14 ±3.73	1.51 ±0.14	0.02 ±0.03	0.11 ±0.01	0.00 ±0.00	0.00 ±0.01	24.96 ±5.26	0.00 ±0.00	1.45 ±0.56

*± *indicates the error in measurement.*

As seen in Table 4.7, the outer region of the corrosion products had an elevated Al (~24 wt%) and Ca (~0.1 wt%) content. Ca was present in the matrix as an impurity, and likely reacted with Si to form a silicate compound, since elevated concentration of Si (~1.5 wt%) and Ca (~0.1 wt%) were seen to track in the outer corroded layer.

Na was seen to be present in the corrosion products. This may be due to deposition of electrolyte through cracks and pores in the corrosion products. This was also observed during linescan analysis of cross-section of Sample I (2, 20).

Figure 4.14 shows the results of a linescan across the corrosion product layer of in-service AZ31 electrode. In this linescan, Si and Mg had a similar profile, suggesting a possible formation of magnesium silicates, which was confirmed by XRD analysis.

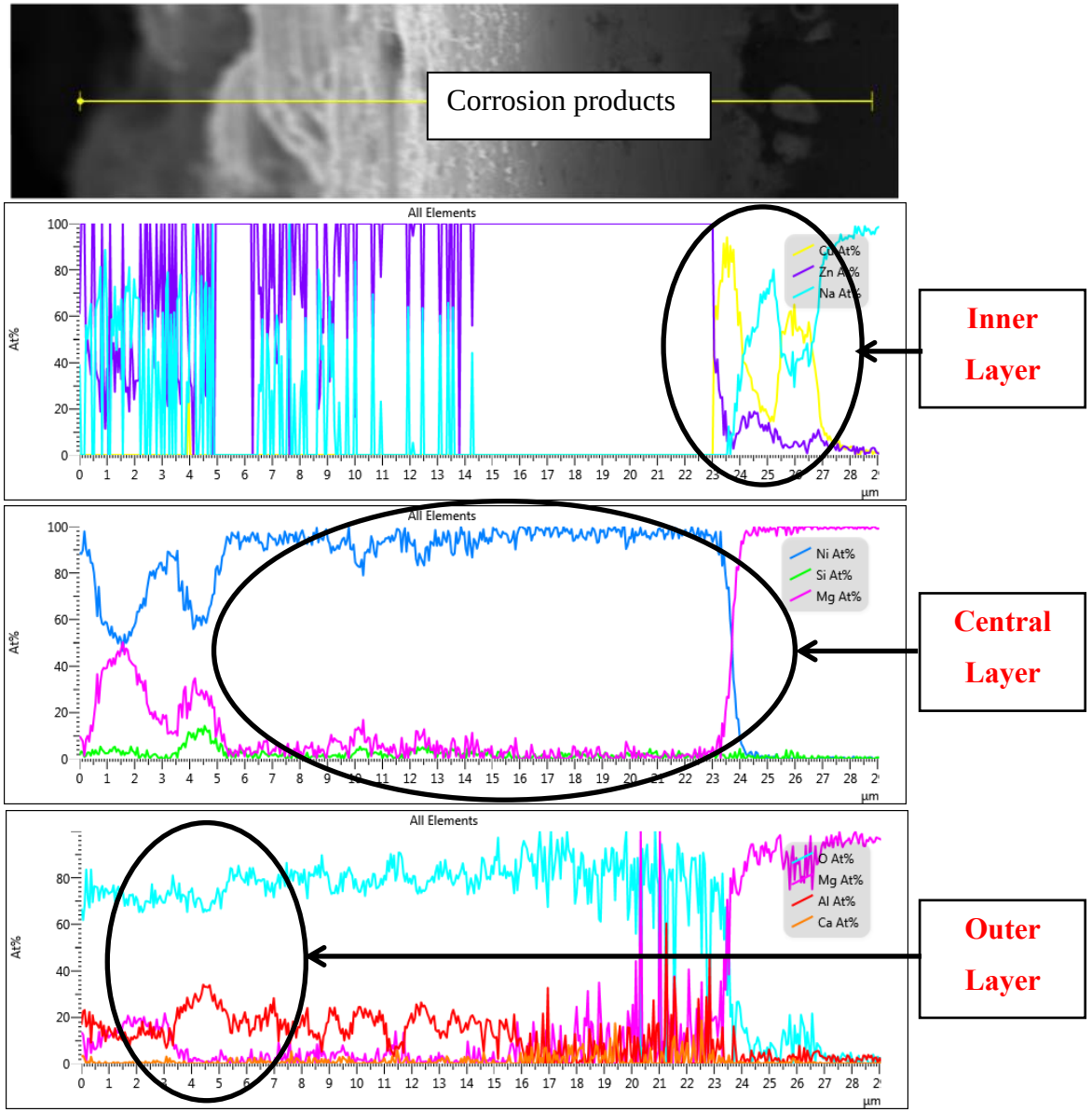

Figure 4.14: Linescan across the corrosion products on in-service AZ31 electrode's cross-section.

4.2. Immersion test results

Immersion tests were performed to examine the physical and chemical changes in the virgin AZ31 alloy as a result of exposure to Electrolyte #1 and Electrolyte #2. In addition to examining the surface of the corroded AZ31 samples, the electrolyte after completion of an immersion test was filtered and the filter paper residue was examined using SEM. Examination of the filter paper residue helped identify any undissolved corrosion products present in the electrolytes.

4.2.1. Analysis of the filter paper residue

Figure 4.15 shows the residue and precipitates retained on the filter paper after filtering the used electrolyte. For both electrolytes, the residues had a relatively high variation in particle size. The quantitative chemical analysis of the filter paper residue for both the electrolytes is provided in Table 4.8.

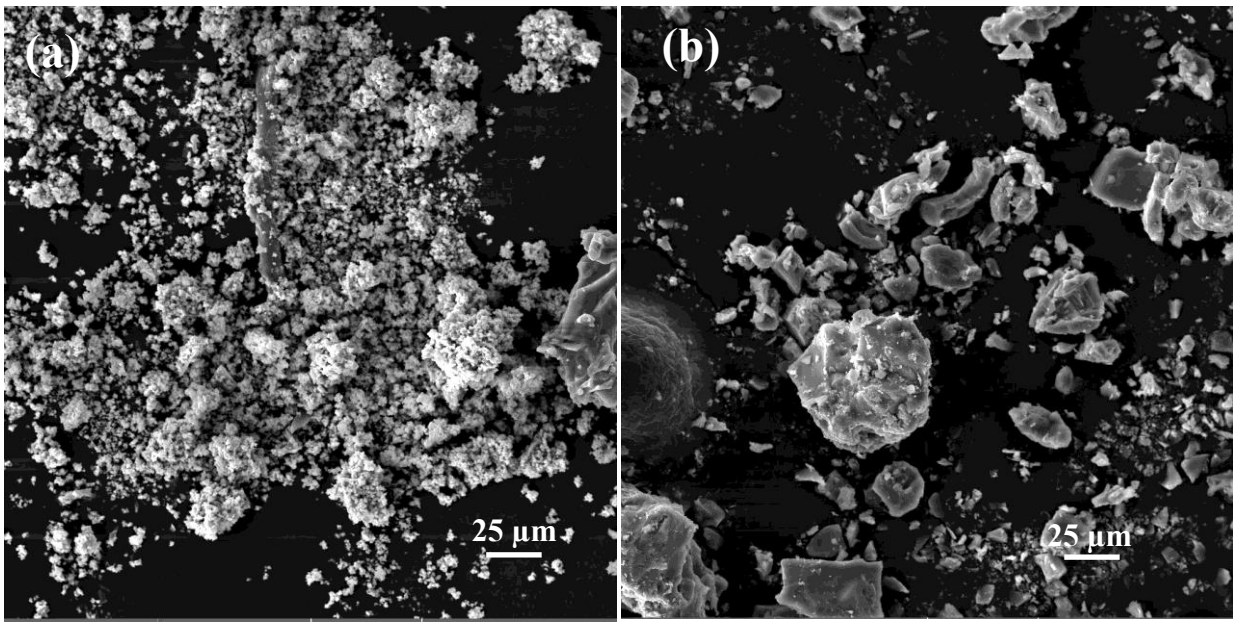

Figure 4.15: Filter paper residue after 20 days of immersion in: (a) Electrolyte #1, (b) Electrolyte #2.

Table 4.8: Composition of filter paper residue in Electrolyte #1 and Electrolyte #2 (wt%) *.

Element	Na	Mg	Al	Si	K	Ca	Mn	Fe	Ni	Cu	Zn
Residue from Electrolyte #1	0.02± 0.03	0.01± 0.02	0.66± 0.04	0.09± 0.05	98.93 ±7.59	0.00± 0.00	0.03± 0.04	0.01± 0.01	0.05± 0.04	0.09± 0.10	0.01± 0.00
Residue from Electrolyte #2	0.57± 0.35	0.92± 0.31	1.26± 0.13	3.87± 1.06	89.85 ±5.98	3.25± 1.25	0.03± 0.02	0.06± 0.24	0.11± 0.04	0.07± 0.03	0.01± 0.01

**± indicates the error in measurement.*

As seen in Table 4.8, Na and Si content was higher for Electrolyte #2 as compared to Electrolyte #1, which was the result of sodium silicate addition to the KOH (in the case of Electrolyte #2). However, a considerable amount of Ca was also present in Electrolyte #2 residuals. This was possibly the result of a reaction between silicon (from the electrolyte) and calcium (present as impurity in the virgin AZ31), resulting in the formation of calcium silicates, as seen in XRD analysis on Sample I (2, 20).

4.2.2. Analysis of the AZ31 surface after immersion test

The surface of all samples after immersion for 10 and 20 days was analyzed in order to observe the evolution of the corrosion products in the respective electrolytes.

4.2.2.1. Analysis of corroded surface after immersion for 10 days

After 10 days of immersion, Sample I (1, 10) and Sample I (2, 10) were removed from the respective electrolytes and stored in a vacuum desiccator until SEM analysis was performed. The results of surface analysis are discussed in the following sections.

i. Corroded AZ31 plate immersed in Electrolyte #1

Figure 4.16 shows the surface of Sample I (1, 10). The morphology of the pits often had similar geometry (shape and diameter) as that of the large Al-Mn precipitates (or agglomerates of fine Al-Mn precipitates) found in the virgin AZ31 alloy (Figure 4.1). Also, it was seen in Figure 4.16(b) that some of the corrosion products remained attached to the AZ31 substrate. These were sites of Al-Mn precipitates of diameter greater than ~20 μm. Figure 4.16(b) shows regions similar to those observed in the in-service AZ31 electrode with "clean" and "dirty" corroded regions (discussed in Section 4.1.3). In this corroded AZ31 sample, the "clean" corroded region had corrosion products still attached to the AZ31 substrate, while the "dirty" corroded region exhibited subdued attack. It was also observed that the fine (<15 μm) Al-Mn precipitates were absent from the surface after 10 days of immersion, as noted in Figure 4.16(c). Elemental mapping (Figure 4.17) was performed on sites with corrosion products still attached to the pits.

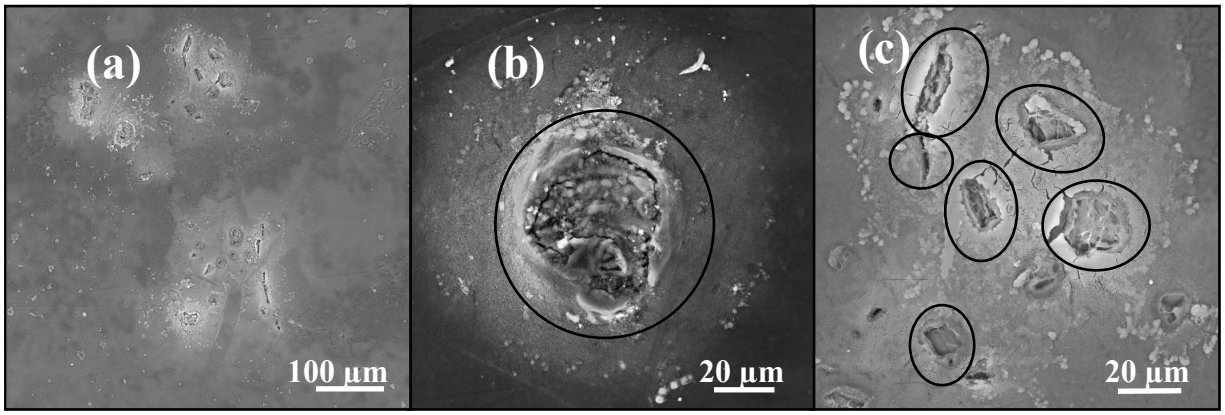

Figure 4.16: SEM image of Sample I (1, 10): (a) Low magnification view, (b) Corrosion products attached to the surface, (c) Pits on the surface.

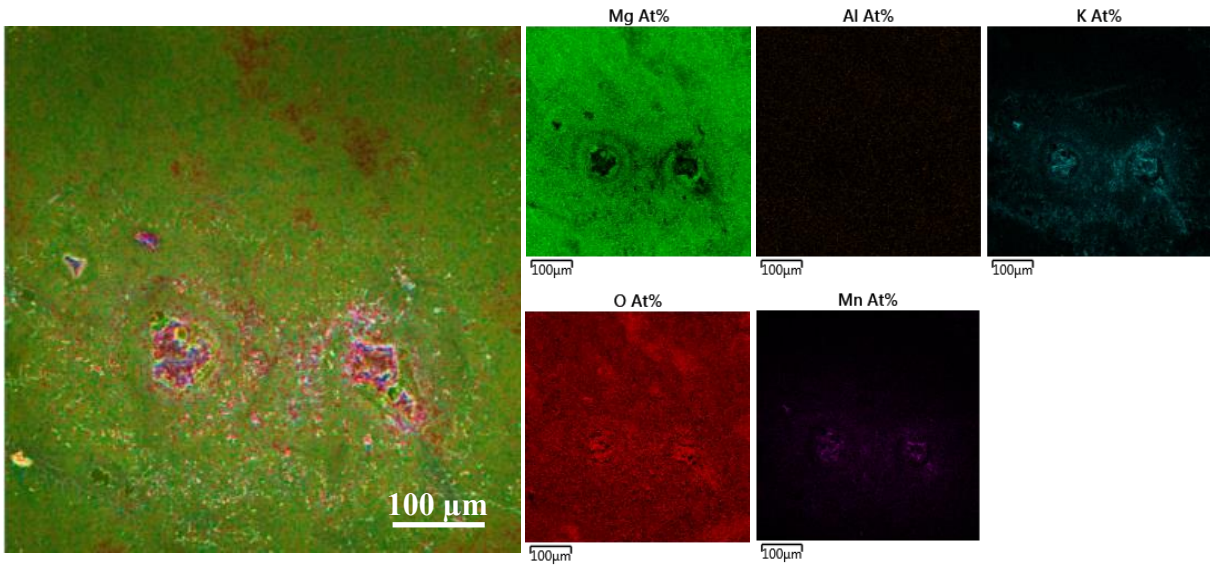

Figure 4.17: Elemental mapping on corrosion products on Sample I (1, 10) using SEM-EDS.

It was observed that Mg was absent in the corrosion products, indicating its selective dissolution into the electrolyte. Potassium was concentrated in the corrosion products in the pit, suggesting its activity in the pit formation.

Interestingly, Mn was present in the corrosion products, but no Al was detected. Thus, the results suggest that Mn from the Al-Mn precipitate was retained, while Al may have de-alloyed from the precipitate and dissolved into the electrolyte. Such de-alloying of Al-Mn precipitate during corrosion was also observed by Oktay *et al.* [31] for AZ31 Mg alloy.

ii. Analysis of corroded AZ31 plate immersed in Electrolyte #2

Analysis of the surface from Sample I (2, 10) in Figure 4.18 revealed that pits evolved on the surface exposed to the electrolyte. These pits were observed across the entire sample surface.

Examination of the sample revealed that pits larger than 10µm had corrosion products still attached to them, as seen in Figure 4.18(b). Such corrosion products were not observed in Sample I (1, 10). Retention of such corrosion products suggests a slower corrosion rate, possibly

the result of the presence silicates in the electrolyte, which may have contributed to the formation of a stable surface magnesium silicate layer (as observed in XRD analysis of Sample I (2, 20)). In addition to the pits with retained corrosion products, fine pits were observed on the sample surface (pit diameter was < 5µm).

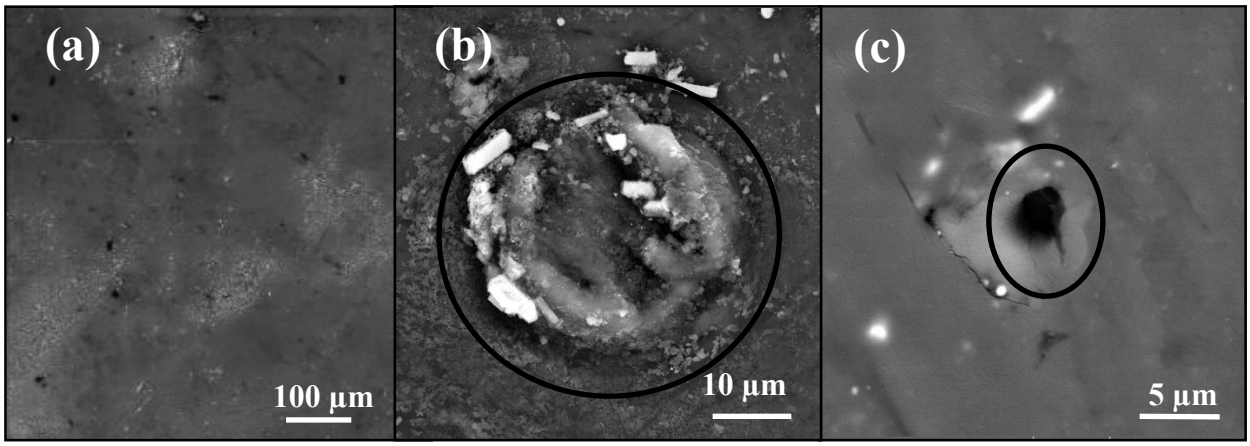

Figure 4.18: Sample I (2, 10) showing: (a) Distribution of pits, (b) Corrosion products attached to a pit, (c) Micro pit.

A representative elemental map at a location where corrosion products were retained on the corrosion pits is presented in Figure 4.19**.** The results indicate that K, Mn and Si were present in the corrosion products, while Al was absent, suggesting its dissolution into the electrolyte. However, the presence of Si and O layer exclusively on the top of the corrosion pit suggests formation of a protective silicon oxide layer covering the corrosion pit

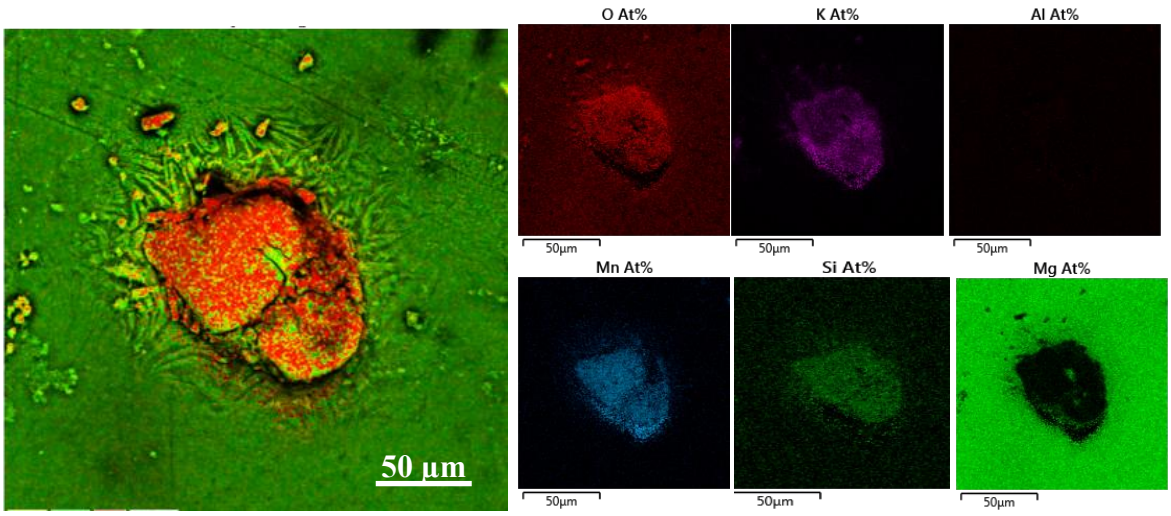

Figure 4.19: Elemental mapping of a pit region in Sample I (2, 10).

4.2.2.2. Analysis of corroded surface after immersion for 20 days

After SEM analysis was completed, the samples were re-immersed in the electrolyte for additional 10 days. After 20 days of total immersion time, SEM analysis was repeated.

i. Analysis of corroded AZ31 plate immersed in Electrolyte #1

After 20 days of immersion, many pits were present on the surface of Sample I (1, 20). Both macroscopic and SEM images of the surface are shown in Figure 4.20. The brown dots seen in the macroscopic image (Figure 4.20(a)) were sites with more advanced corrosion.

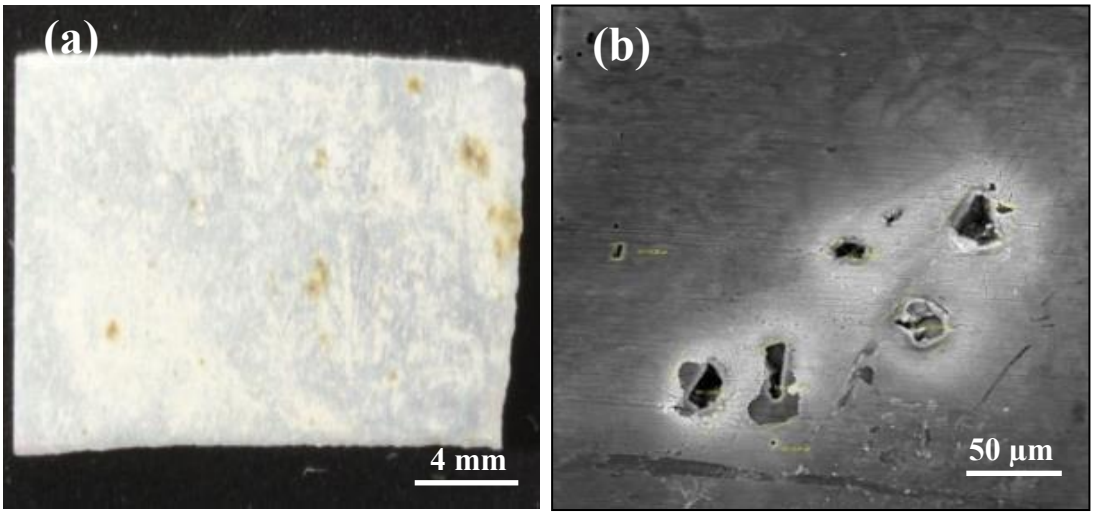

Figure 4.20: Corrosion pits in Sample I (1, 20): (a) Macro view of the sample, (b) Large pits and voids.

It was observed that pits of ~ 20µm were present across the entire sample surface. Interestingly, the shape of these pits resembled the Al-Mn precipitates. Corrosion products on the pits of ~ 20µm were absent (while these were still present after immersion after 10 days). Elemental mapping was performed to determine the composition of elements in the pit, as shown in Figure 4.21.

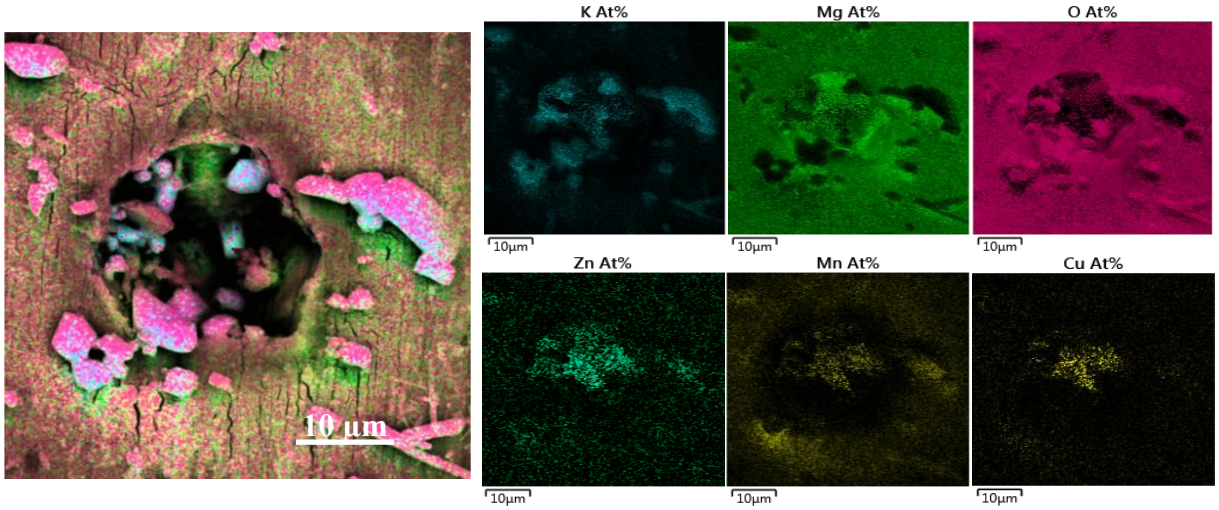

Figure 4.21: SEM-EDS map of a pit on Sample I (1, 20).

As seen in Figure 4.21, Mn was retained in the pit, while Al was absent, suggesting a preferential dissolution of Al from the Al-Mn precipitates

In addition, segregation of Cu and Zn was observed after immersion for 20 days, which was not observed after 10 days of immersion. This Cu-Zn may have been formed due to the reaction of Mg(Cu-Zn) phase with the electrolyte. This phase was reported to readily form in Mg alloys. [23]

It was noticed that the immediate area around the cavities had a different chemistry than the matrix, as seen in the BSE image in Figure 4.22. The average concentration of elements near the pit is summarized in Table 4.9.

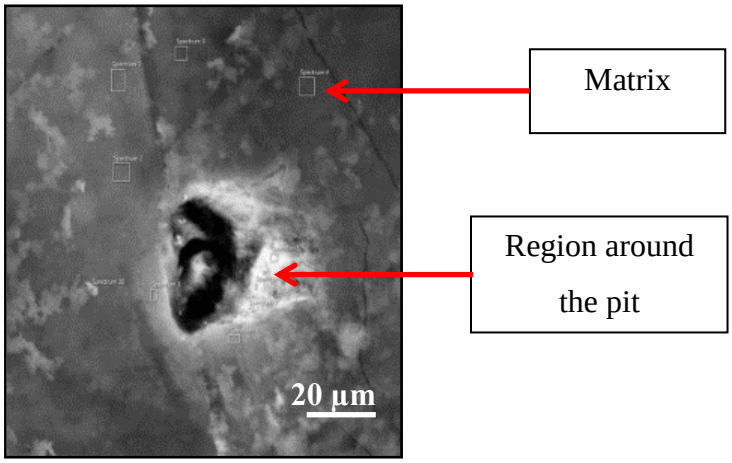

Figure 4.22: Vicinity of a pit in Sample I (1, 20).

Table 4.9: Concentration of elements in the vicinity of the pit in Sample I (1, 20) (wt%) *.

Element	O	Na	Mg	Al	Si	K	Ca	Mn	Fe	Ni	Cu	Zn
Matrix	33.24 ±5.59	0.22 ±0.12	62.61 ±5.59	1.17 ±0.12	0.10 ±0.05	0.84 ±0.23	0.27 ±0.08	0.53 ±0.12	0.22 ±0.03	0.00 ±0.00	0.01 ±0.00	0.78 ±0.07
Region around pit	29.73 ±6.63	0.15 ±0.06	40.96 ±4.03	0.86 ±0.14	0.15 ±0.04	14.29 ±3.01	0.60 ±0.09	11.89 ±5.86	0.78 ±0.22	0.00 ±0.00	0.18 ±0.06	0.40 ±0.06

*± *indicates the error in measurement.*

As seen in Table 4.9, the potassium content in and around the pit (~14 wt%) was higher than in the matrix. Similarly, Mn near the pit was significantly higher (11.9 wt%) than in the matrix, suggesting that pit initiated at a region of an Al-Mn precipitate.

ii. Analysis of corroded AZ31 plate immersed in Electrolyte #2

After immersion of Sample I (2, 20), a few pits were present on the specimen surface. Visual examination of the corroded surface (Figure 4.23a) did not reveal a localized attack as was seen the case of Sample I (1, 20). However, many of the corrosion sites were seen to have corrosion products still attached, as seen in Figure 4.23(b)**.** The size of the corrosion products was ~20µm (or greater) in diameter and appeared to protect the AZ31 matrix from undergoing further degradation

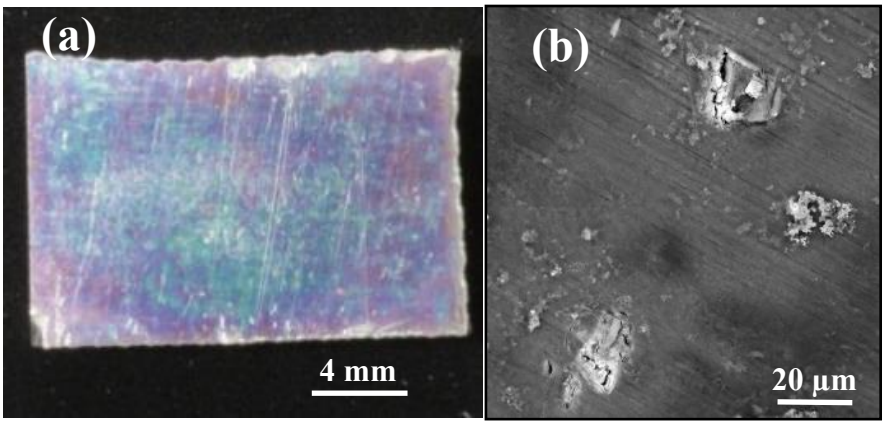

Figure 4.23 : Corrosion pits in Sample I (2, 20): (a) Macro view of the sample, (b) Corrosion pits.

Elemental mapping was performed on the pits (Figure 4.24) and revealed that the pit region contained segregated Mn, Si and K. Also, Ca was present in the pit, possibly forming a calcium silicate compound via reaction of Ca (from the alloy) and Si (from the electrolyte).

Further, the Si was present in the vicinity of the pit, together with Mg, possibly confirming the presence of magnesium silicates, which was detected in XRD analysis of the Sample I (2, 20).

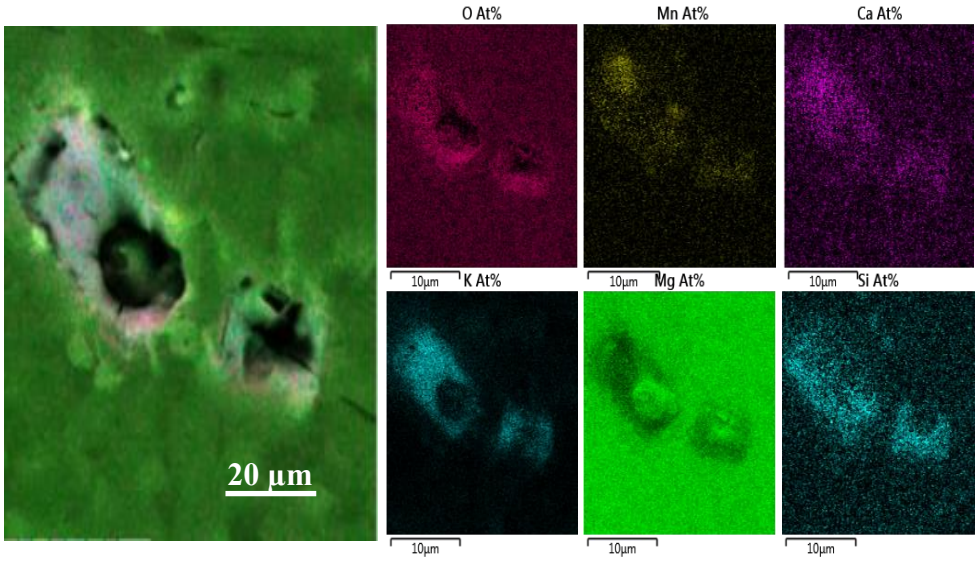

Figure 4.24: SEM-EDS map of pits in Sample I (2, 20).

A number of point and area scans were performed, as seen in Figure 4.25, to obtain quantitative composition in the region surrounding the pit. The results are summarized in Table 4.10.

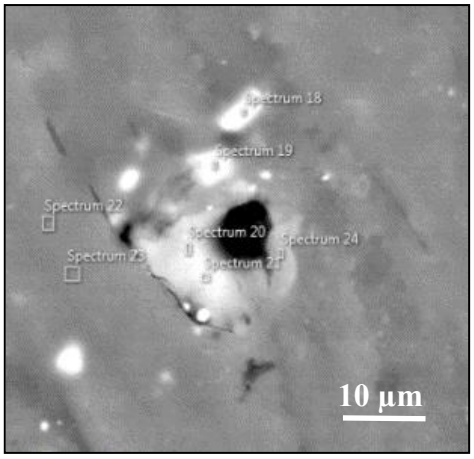

Figure 4.25: Detailed view of a pit in Sample I (2, 20).

Table 4.10: Composition of corroded pit in Sample (2, 20) (wt%) *.

Element	O	Na	Mg	Al	Si	K	Ca	Mn	Fe	Ni	Cu	Zn
Area around the pits	21.9 ±6.04	0.24 ±0.06	42.99 ±4.87	4.66 ±1.83	1.41 ±0.69	21.00 ±3.23	0.41 ±0.18	6.12 ±2.83	0.61 ±0.24	0.08 ±0.07	0.04 ±0.05	0.55 ±0.12
Matrix	14.01 ±0.63	0.25 ±0.05	78.91 ±0.60	2.00 ±0.04	0.42 ±0.05	3.04 ±0.03	0.10 ±0.06	0.22 ±0.02	0.09 ±0.10	0.07 ±0.06	0.01 ±0.01	0.88 ±0.16

*± *indicates the error in measurement.*

As seen in Table 4.10, Si (~1 wt%) and Mn (~6 wt%) content in the pits was considerably higher in comparison to the matrix. The Mn content was high due to a possible trace of an Al-Mn precipitate, which degraded due to corrosion. Similar to Sample I (1, 20), the Mg content (~79 wt%) in the matrix was much lower than the Mg content in the virgin AZ31 plate (~95 wt%), indicating a possible dissolution of Mg in the vicinity of the pit, or the formation of surface oxides which decreased the relative amount of Mg in the measured area.

4.2.3. Analysis of the cross-section of the AZ31 plate after immersion for 20 days

The cross-section of the corroded samples was analyzed to study the interface region (i.e., interface between AZ31 alloy and the electrolyte).

4.2.3.1. Cross section of corroded AZ31 alloy in Electrolyte #1

Elemental mapping (Figure 4.26**)** of the cross-section region was carried out. In addition to maps, a linescan was also performed across the interface to reveal the changes in elemental concentrations, as plotted in Figure 4.27.

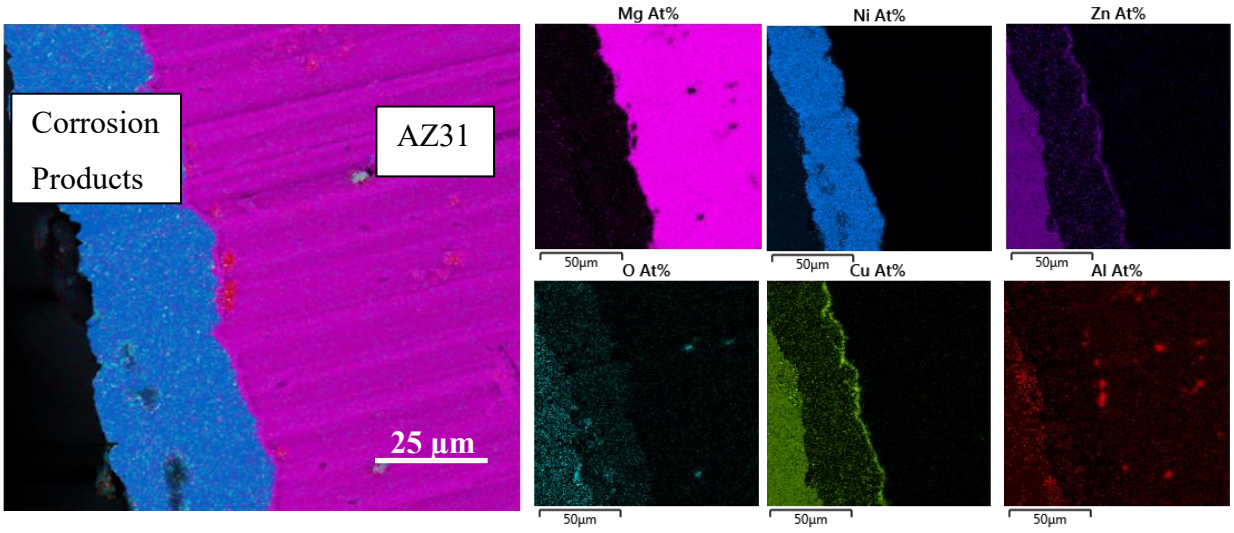

Figure 4.26: SEM-EDS map across corrosion products in Sample I (1, 20).

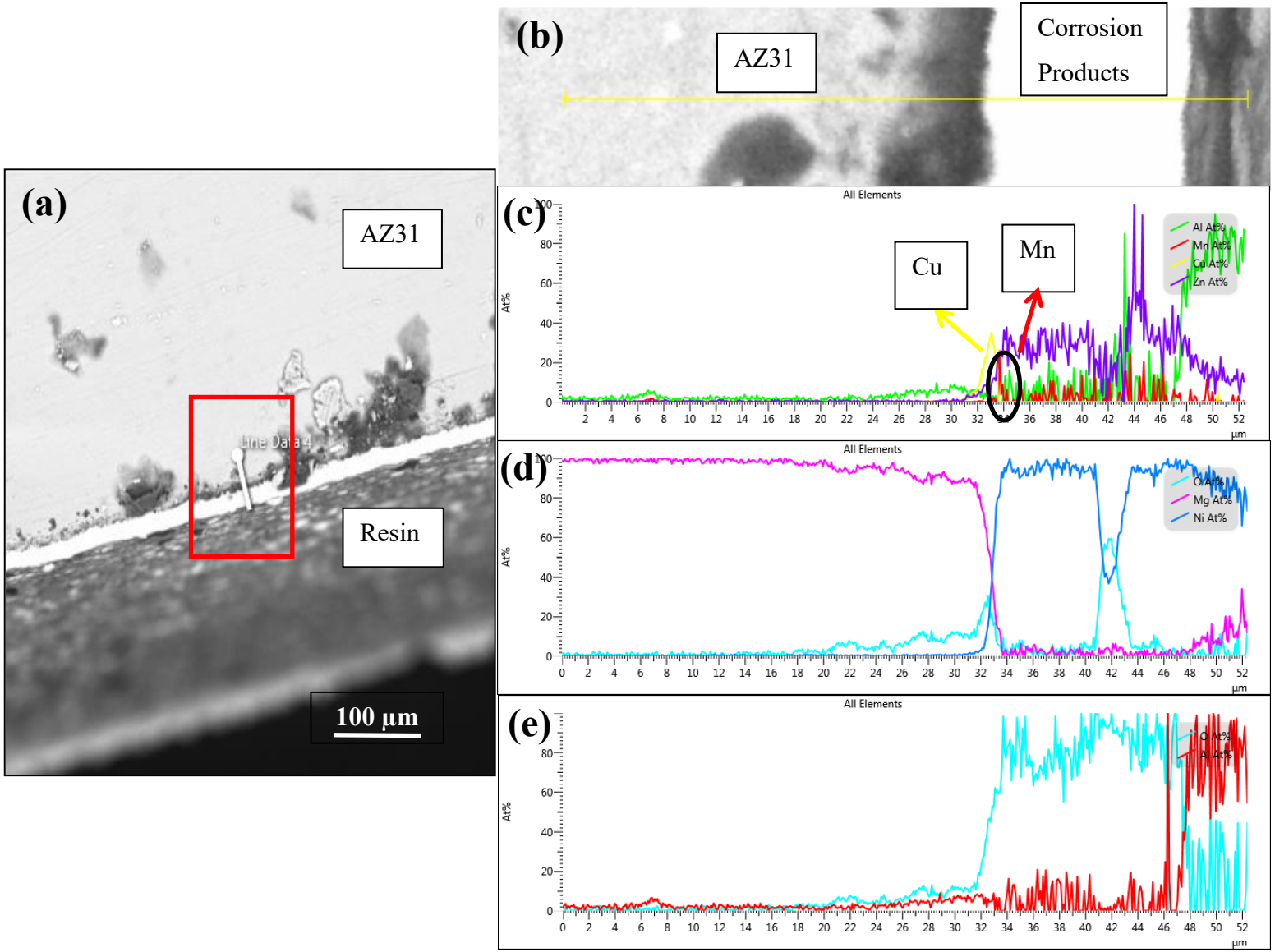

Figure 4.27: Linescan along cross section of Sample I (1, 20): (a) Location of linescan, (b) Detailed view of linescan location, (c) Inner layer of corrosion products, (d) Middle layer of corrosion products, (e) Outer layer of corrosion products.

Figure 4.27 revealed the presence of ~15μm thick Ni-rich layer. Although Ni was present in the AZ31 alloy only as an impurity, it is possible that due to selective dissolution of the α-Mg matrix and other elements at the electrolyte interface, the corrosion layer retained elemental Ni (which is insoluble in Mg).

In addition to Ni, an inner layer rich in Cu was also detected, and this layer had an elevated concentration of Mn (reaching ~19 wt%) at the interface between the corrosion products and the AZ31 substrate, as seen in Figure 4.27(c). Figure 4.26 shows concurrent presence of Cu and Zn, suggesting that a Mg(Cu-Zn) phase was selectively attacked leaving Cu-Zn residue at the substrate surface, with preferential dissolution of Mg into the electrolyte.

4.2.3.2. Cross section of corroded AZ31 plate immersed in Electrolyte #2

Elemental maps of the interface region between the electrolyte and the AZ31 alloy of Sample I (2, 20) are shown in Figure 4.28. Also, a linescan across the corrosion products is provided in Figure 4.29**.**

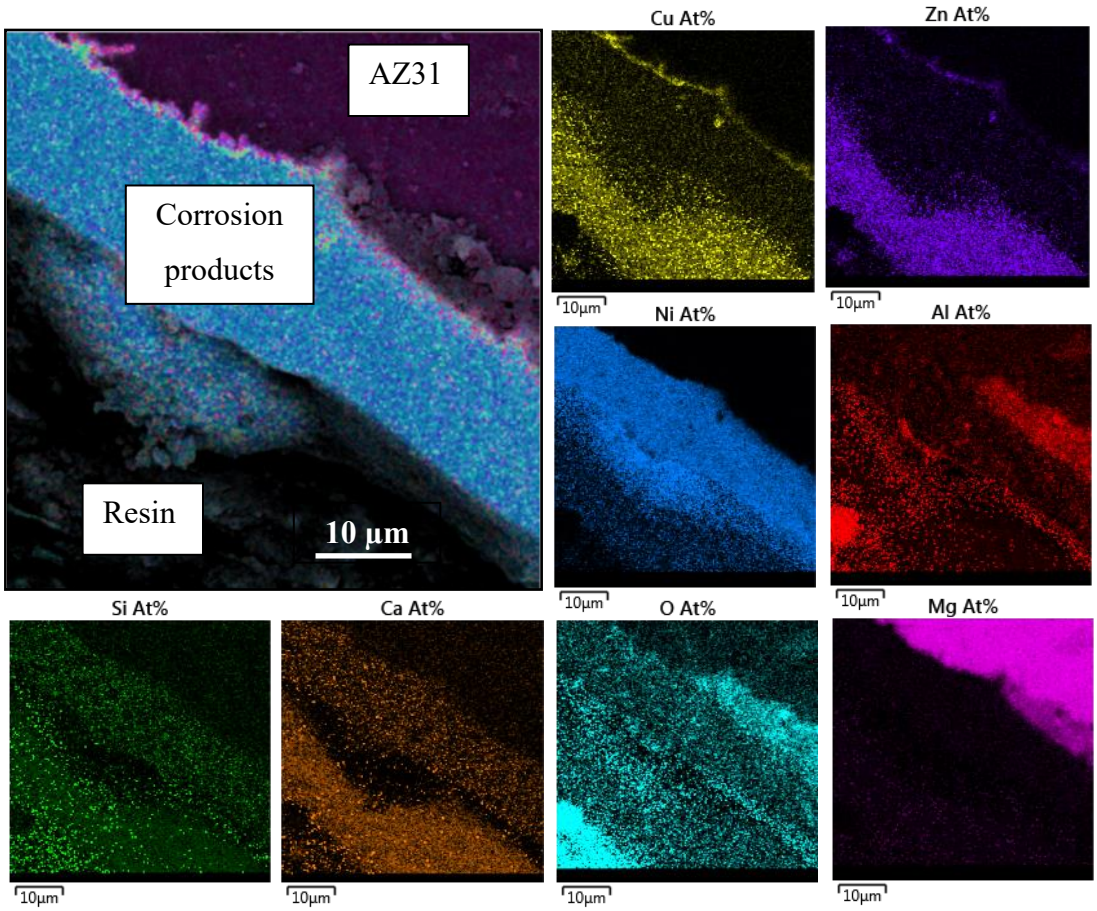

Figure 4.28: Elemental mapping of Sample I (2, 20).

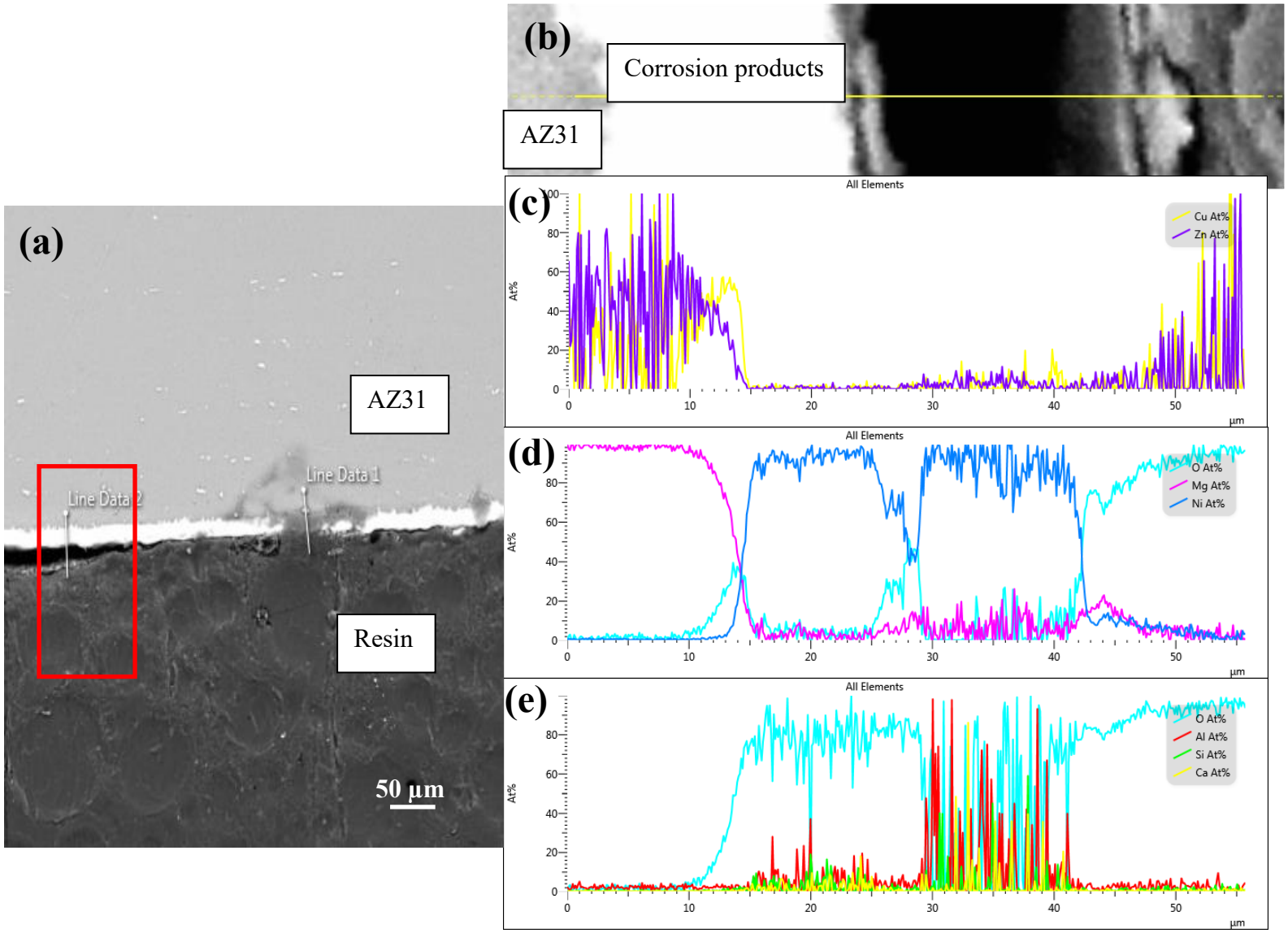

Figure 4.29: SEM-EDS linescan across the corrosion products of Sample I (2, 20): (a) Sample cross-section, (b) Linescan location, (c) Inner layer of corrosion products, (d) Middle layer of corrosion products, (e) Outer layer of corrosion products.

The continuous inner layer of corrosion products observed in Figure 4.28 and Figure 4.29 was rich in Cu and Zn. The central region of the corrosion layer was rich in Ni, similarly as observed in Sample I (1, 20).

Unlike in the case of Sample I (1, 20), the sample exposed to the sodium silicate electrolyte contained a significant amount (~12.5 wt%) of Si in the corrosion layer. This layer may have been Mg silicate rich layer also detected in the XRD analysis (Figure 4.31).

The presence of Ca in the corrosion products was also detected at the interface with Electrolyte #2. Presence of Ca may indicate the formation of calcium silicates, which are stable and thus would protect the AZ31 substrate. [67]

The concentration of Al at the interface was relatively high (30 wt%), suggesting that an outer layer rich in Al evolved due to dissolution of the Al-Mn precipitates. [31]

Interestingly, a uniform layer of Mg was absent from the corrosion products in corroded samples immersed in both Electrolyte #1 and Electrolyte #2. This may have been due to selective dissolution of Mg from the matrix in the electrolyte.

4.2.4. Effect of immersion time on the corrosion surface layer

Based on the results presented in Section 4.2.2.1 and Section 4.2.2.2, it is evident that the duration of immersion had a significant impact on the formation of pits on the AZ31 alloy.

The trends in degradation observed for the two different electrolytes were comparable for both electrolytes (i.e., comparison of Sample I (1, 10) to Sample I (1, 20), as well as Sample I (2, 10) to Sample I (2, 20)).

The number of pits significantly increased with time in both electrolytes. This trend indicates a continued corrosion of the AZ31 alloy and the absence of a protective surface film. In

particular, the corrosion was likely driven by the continued dissolution and spallation of Al-Mn precipitates, as well as dissolution of the magnesium matrix.

Increase in the immersion time from 10 days to 20 days enabled formation of a Cu-Zn layer in both electrolytes. This layer is believed to be formed from cathodic Mg(Cu-Zn) eutectic phase present in Mg alloys. [35] This Cu-Zn rich layer was not observed in the samples after 10 days of immersion. As seen in Appendix (Section B2), the Cu-Zn layer became appreciable only after ~10 days of immersion.

4.3. ICP-OES analysis

The change in the composition of the electrolyte prior to and post corrosion is provided in Table 4.11.

Table 4.11: Concentration of elements in electrolyte prior and post corrosion (after 20 days) obtained from ICP-OES analysis (mg/L).

Element	Al	Cu	Mg	Mn	Ni	Zn
Electrolyte #1 (Pre corrosion)	0.052	0.576	0.036	0.069	0.158	2.533
Electrolyte #1(Post corrosion)	3.471	0.584	0.838	0.076	0.163	2.581
Electrolyte #2 (Pre corrosion)	0.024	0.480	0.004	0.160	0.130	2.179
Electrolyte #2 (Post corrosion)	2.217	0.522	0.312	0.067	0.143	2.402

It was observed that the concentration of Al increased in both electrolytes after corrosion, suggesting that Al was dissolving from the AZ31 alloy into the electrolytes. The Al could have originated either from the α-Mg solid solution matrix, or from the disintegrating Al-Mn precipitates. This increase in Al concentration was expected due to its known high activity in alkaline solutions. [63]

The concentration of Mg in the electrolyte also increased after corrosion experiment. The Mg may have originated from the dissolution of the α-Mg matrix at the AZ31 – electrolyte

interface, or it may have originated from the spallation of $Mg(OH)_2$ [25] residuals, which were present on the substrate after a corrosion test.

Since the concentration and dissolution of Mn, Ni, Cu was relatively low, it is thus likely that these elements were retained on the corroded AZ31 surface after immersion tests due to the dissolution of the AZ31 matrix, rather than due to electro-deposition of these elements from the electrolyte.

Comparing the values observed for the two electrolytes, it is of interest to note that the concentration of both Mg and Al in Electrolyte #1 was higher than in Electrolyte #2. Thus, it appears that the addition of the sodium silicate has reduced the activity of reactions between the AZ31 alloy and the Electrolyte #2, thus reducing the corrosion rate in this electrolyte.

4.4. X-Ray diffraction studies

X-ray diffraction studies were performed to detect the composition of the corrosion products on the surface of the AZ31 alloy. The results obtained for corroded Sample I (1, 20) are shown in Figure 4.30. XRD analysis detected the α-Mg matrix, as expected. However, $Ni(OH)_2$ was also detected on the surface of the corroded sample, suggesting that the trace amounts of Ni in the matrix possibly reacted with the OH^- ions from the electrolyte and enabled the formation of a $Ni(OH)_2$. Thus, the layer rich in Ni seen in the SEM-EDS linescans of Sample I (1, 20) (seen in Figure 4.27) was possibly $Ni(OH)_2$.

The XRD analysis did not identify the presence of Al-Mn precipitates on the surface of the corroded AZ31 sample. This was possibly because of dissociation of the precipitates post corrosion.

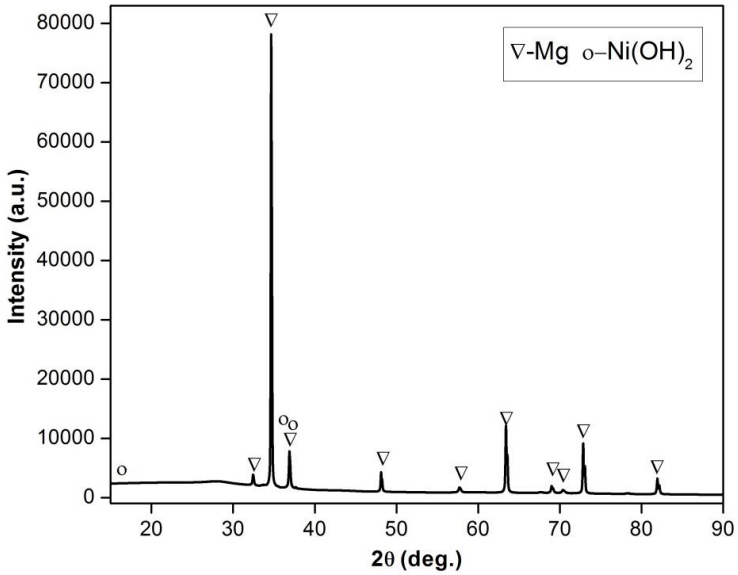

Figure 4.30: XRD results for AZ31 Sample I (1, 20).

The XRD diffractogram for Sample I (2, 20) is included in Figure 4.31. In addition to detecting a $Mg(OH)_2$ layer, Ca- and Mg-silicates were also indexed. Their presence has been known to be beneficial for corrosion protection of Mg alloys. [23] [67] The $Ni(OH)_2$ layer was not detected in this case, possibly because it was covered with the silicate layers, and the XRD penetration of the Ca- and Mg-silicate layer was difficult.

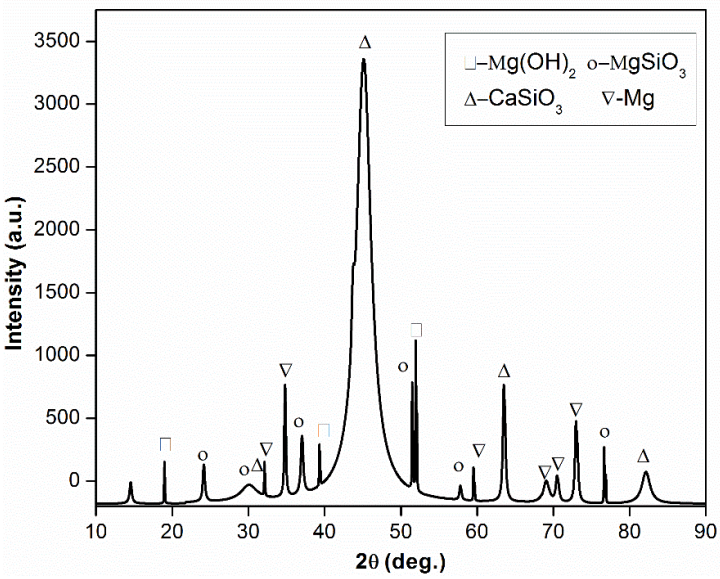

Figure 4.31: XRD results for Sample I (2, 20).

4.5. Electrochemical tests

The electrochemical behavior of the samples was studied by performing Tafel polarization tests and electrochemical impedance spectroscopy. The results of these analyses are discussed in the following sections.

4.5.1. Tafel polarization

A representative curve obtained for a Tafel polarization test is provided in Figure 4.33. Both anodic and cathodic curves are included. The cathodic curve shows a degree of linearity, which is typically associated with hydrogen gas evolution during corrosion of Mg alloys. [25]

The corrosion current density was calculated by extrapolating the anodic and cathodic curves near the cusp potential. The circuit constants obtained from Tafel analysis are included in Table 4.12. The values of corrosion current obtained for the samples exposed to the two electrolytes are also samples exposed to the two electrolytes are also included in Table 4.12.

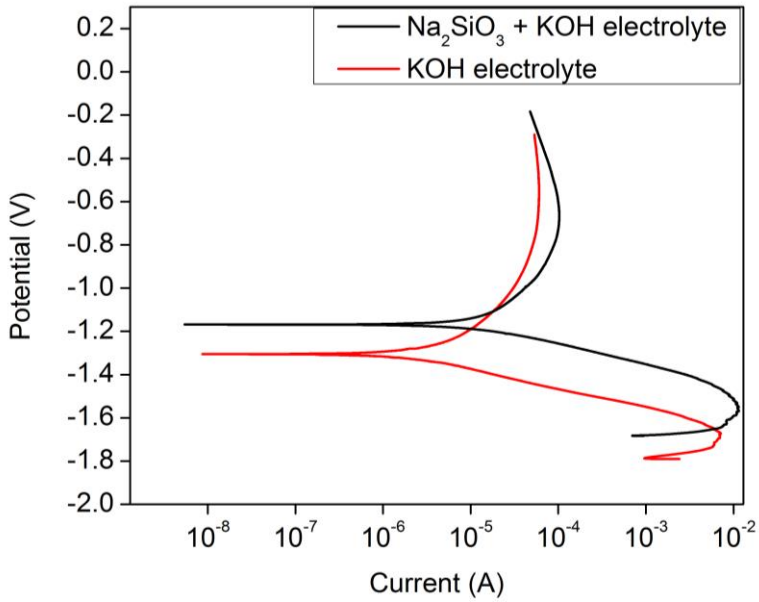

Figure 4.32: Tafel polarization curve for Sample T (1) and Sample T (2).

Table 4.12: Passivation parameters for corroded AZ31 alloy obtained from Tafel analysis.

Material	β_a	B_c	E_{corr} (V)	i_{corr} (µA/cm^2)
Sample T (1)	0.23	0.08	-1.27	7.71
Sample T (2)	0.08	0.05	-1.16	5.85

It was observed that the corrosion potential of Sample T (2) was more noble (~ -1.1V) in comparison to that of Sample T (1) (~ -1.3V). This result provided a quantitative proof of an improved corrosion resistance of Sample T (2). This was possibly also contributed from the protective nature of silicate layer (detected in XRD and SEM analyses) formed on the surface of the sample immersed in electrolyte with silicate addition.

As seen in Table 4.12, the corrosion current for Sample T (1) (7.71 µA/cm^2) was ~ 30% greater than that of the Sample T (2) (5.85 µA/cm^2). The corrosion rate is directly proportional to the corrosion current. [22] Therefore, corrosion rate of Sample T (2) was reduced with the addition of sodium silicate to KOH by ~ 30%.

However, the corrosion test results obtained from Tafel extrapolation only give information about the onset of corrosion [22], since the Tafel test was completed within a relatively short period of time. Thus, the Tafel analysis did not capture long term exposure effects.

4.5.2. Electrochemical impedance spectroscopy

Figure 4.33 shows the Nyquist plot and the equivalent circuit obtained for AZ31 Sample E (1) and Sample E (2). The equivalent circuit that provided the best match between experimental and theoretical results was the modified Randle's circuit. In this circuit model, R_s represents the solution resistance, Q and R_t are the constant phase element and the charge transfer resistance, respectively, and W is the Warburg coefficient. [68]

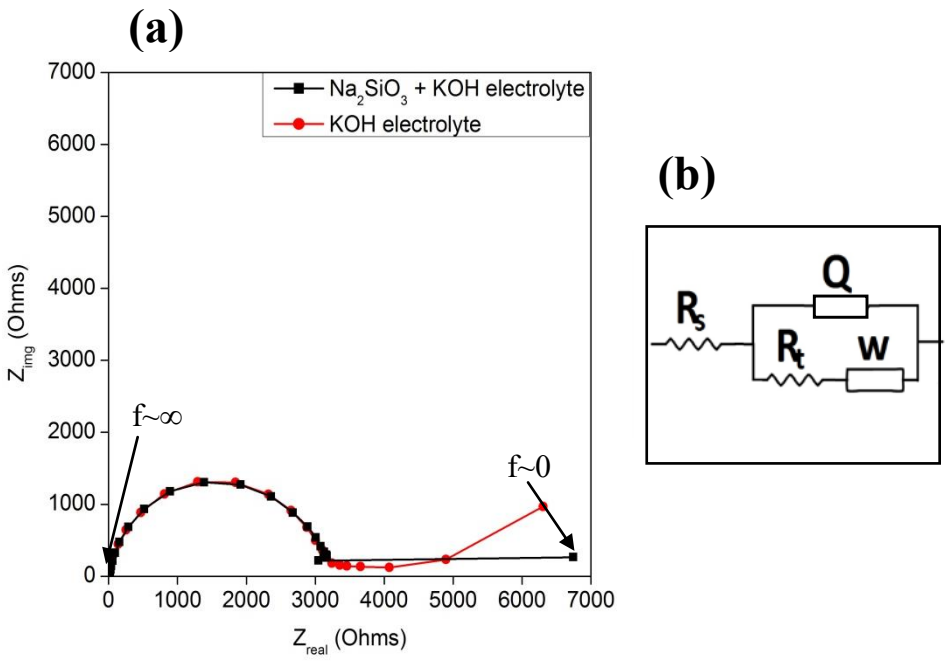

Figure 4.33: EIS results for Sample E (1) and Sample E (2): (a) Nyquist plot, (b) Equivalent circuit.

The results in Figure 4.33 reveal a deviation of the semicircle for both electrolytes for lower frequency values (at high Z_{real} values), possibly due to diffusion of elements into the

electrolyte from the AZ31 alloy surface. [69] This result is consistent with the observed diffusion of Al and Mg from the virgin AZ31 plate into the electrolyte, as seen in SEM-EDS and ICP-OES analyses. The Bode magnitude and phase plots for the two electrolytes are included in Figure 4.34.

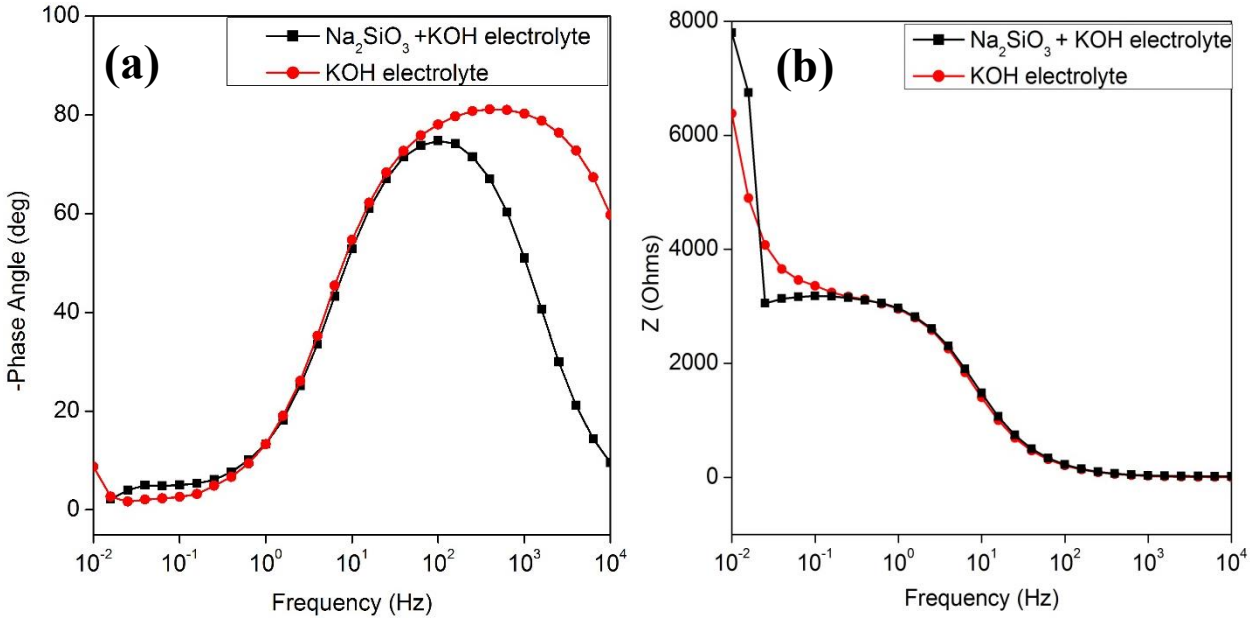

Figure 4.34: EIS results: (a) Bode phase plot, (b) Bode impedance plot.

As seen in Figure 4.34, at frequencies above $>10^1$ Hz the phase angle was approaching -80^0 and the slope of the impedance vs. frequency curve was negative for both samples. This indicates that the circuit was capacitive in nature. [6] Capacitance was present possibly because of the formation of the electrical double layer on the surface of the sample. [70]

At higher frequencies ($>10^2$), the phase angle approached 0°, indicating a purely resistive circuit. Therefore, in this region, diffusion controlling processes [71] with Al and Mg ions diffusing into the electrolyte dominated.

The electrochemical parameters obtained from EIS analysis are included in Table 4.13. Although the EIS modeling and analysis may provide information about mechanisms in corroding systems, impedance measurements at low frequencies often do not capture the dynamic events associated with corrosion reactions, thus leading to some measurement error. [14] Therefore EIS was only used as a tool to provide further qualitative information about the corrosion mechanisms occuring in the system.

Table 4.13: Electrochemical parameters obtained from EIS analysis.*

Material	R_s (Ω)	Q (μF)	R_c (kΩ)	W ($m\Omega s^{-1/2}$)
Sample E (1)	10.81±1.18	7.14±0.44	3.09±0.26	0.84±0.16
Sample E (2)	22.42±1.58	7.28±0.37	3.02±0.18	1.81±0.41

** Values in brackets represent error for individual parameters.*

The capacitance value can provide information about the structure of the corrosion product film. [72] In the present work, the value suggests the presence of an electrical double layer. Assuming the surface area of the corrosion products and the distance of separation (of charges in the double layer) to be the same for the two samples, the capacitance was directly proportional to the dielectric constant. [73] The dielectric constant is directly proportional to the film thickness and its molecular density. [72] [74] [75] Since the capacitance measured for Sample E (2) (7.28±0.13μF) was greater than that of Sample E (1) (7.14±0.12μF), the corrosion products in Electrolyte #2 had a higher density and possibly offered a better corrosion protection of the AZ31 substrate. For Electrolyte #2, the Warburg impedance (or resistance to diffusion) (1.81 $m\Omega s^{-1/2}$) was higher than in the case of Electrolyte #1 (0.84$m\Omega s^{-1/2}$). This result also suggests a reduction in diffusion at the AZ31 surface in Electrolyte #2, possibly due to the presence of the silicate surface layer.

4.6. Role of Al-Mn precipitates on corrosion

Based on the results obtained in this research, the initiation of corrosion in the AZ31 alloy exposed to a highly alkaline environment was associated with the Al-Mn precipitates. These precipitates were reported to act as a cathodic site and form a galvanic couple with α-Mg in the literature. [23] In the present work, pit formation and AZ31 degradation was seen to initiate at fine Al-Mn precipitates.

With continued corrosion and diffusion of Al and Mg from the vicinity of the Al-Mn precipitates, pits nucleated and grew in size. As result of the galvanic coupling (between Al-Mn precipitate and the Mg matrix), corrosion continued deep into the AZ31 matrix until the precipitates completely detached from the matrix and fell-out. The falling out of precipitates resulted in the formation of irregular shaped voids on the surface. This mechanism is schematically illustrated in Figure 4.35.

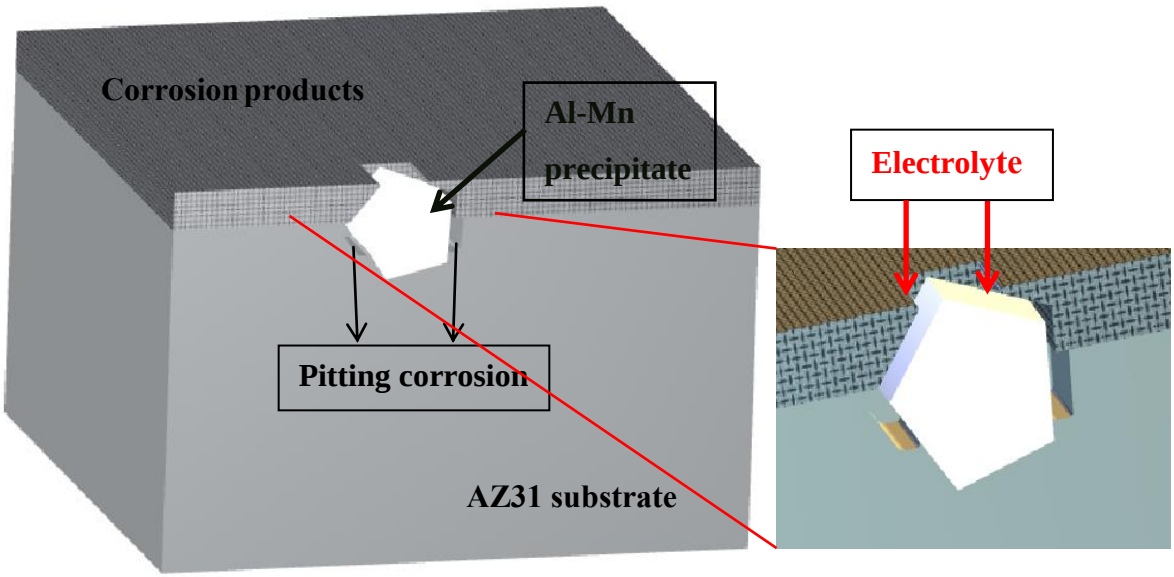

Figure 4.35: Role of Al-Mn precipitates in pitting corrosion of AZ31 alloy.

Chapter 5: CONCLUSIONS AND FUTURE WORK

5.1. Conclusions

The mechanism of pit formation and the effect of addition of silicates into KOH electrolyte was studied in this research. The major conclusions from this work are as follows:

i. Microstructural analysis revealed that the virgin AZ31 plate contained Al- and Mn-rich precipitates. TEM and XRD analyses revealed that these precipitates were Al_8Mn_5.

ii. The corrosion of the AZ31 plate was non-uniform. The regions around Al-Mn precipitates appeared to be severely affected by the electrolyte after immersion for 20 days. It was also observed that pit morphologies in both electrolytes appeared to correlate with the Al-Mn precipitate morphologies.

iii. The addition of sodium silicate improved the corrosion resistance of the AZ31 alloy due to the formation of a stable silicate layer. This was confirmed with XRD and SEM analyses.

iv. Tafel analysis revealed a shift of corrosion potential to nobler direction for the sample immersed in electrolyte with silicate addition.

v. Electrochemical Impedance Spectroscopy showed low diffusion rates (higher Warburg coefficient) for samples immersed in electrolyte with silicate addition, possibly due to the presence of a stable silicate layer restricting corrosion and dissolution of the Mg matrix.

vi. ICP-OES analysis of the electrolyte prior to and post corrosion revealed possible dissolution of Mg and Al from the matrix into the electrolyte.

5.2. Future work

In this research, it was observed that the Al-Mn rich precipitates likely contributed to micro-galvanic corrosion in the alloy. Also, the presence of trace amounts of Ni and Cu may have contributed to the formation of surface layers. Therefore, control of the purity of the AZ31 material may be a key to avoiding corrosion issues related to Fe, Ni and Cu diffusion.

Casting or sintering of different Mg alloy compositions can be carried out to study the effect of elements on the corrosion behavior of the new alloys.

An interesting area to explore would be to alter the concentration of the electrolyte and observe the effect of concentration on the corrosion kinetics of the AZ31 alloy. Further, the role of Mg(Cu-Zn) phases on the corrosion of AZ31 plate is not understood and additional research is required to understand the presence and corrosion of these precipitates.

Bibliography

[1] C. Uttley, Magnesium, New York: Benchmark Books, 2000.

[2] E. Emley, Principles of magnesium technology, Pergamon Press, 1966.

[3] D. Aurbach, Y. Gofer, Z. Lu, A. Schechter, O. Chusid, H. Gizbar, Y. Cohen, V. Ashkenazi, M. Moshkovich, R. Turgeman and E. Levi, "A short review on the comparison between Li battery systems and rechargeable magnesium battery technology.," *Journal of Power Sources,* vol. 97, pp. 28-32, 2001.

[4] S. Alsagabi, J. Ninlachart, K. S. Raja and I. Charit, "Passivity and localized corrosion of AZ31 magnesium alloy in high pH electrolytes," *Journal of Materials Engineering and Performance,* vol. 25, no. 6, pp. 2364-2374, 2016.

[5] R. W. Revie and H. H. Uhlig, Corrosion and corrosion control, John Wiley and Sons, 2008.

[6] ASM13A, "Corrosion: Fundamentals, testing, and protection," ASM International, 2003.

[7] G. Davis, Corrosion: Understanding the basics, ASM International, 2000.

[8] D. Shoesmith, Kinetics of corrosion, ASM International, 2003, pp. 42-51.

[9] R. Cahn, P. Haasen and E. J. Kramer, Material science and technology; Corrosion and environmental degradation, Wiley, 2000.

[10] W. D. Callister, Materials science and engineering: An introduction, John Wiley and Sons, 2007.

[11] G.L.Song, "Corrosion electrochemistry of magnesium and its alloys," in *Corrosion of Magnesium alloys*, Woodhead Publishing, 2011, pp. 3-65.

[12] ASTMG31-2012a, "Standard guide for laboratory immersion corrosion testing of metals," ASTM International, West Conshohocken, PA, 2012.

[13] Y. Cheng, T. Qin, H. Wang and Z. Zhang, "Comparison of corrosion behaviors of AZ31, AZ91, AM60 and ZK60 magnesium alloys," *Transactions of Nonferrous Metals Society of China,* vol. 19, no. 3, pp. 517-524, 2009.

[14] D. A. Jones, Priciples and prevention of corrosion, Prentice Hall, 1996.

[15] N. Perez, Electrochemistry and corrosion science, vol. 412, Boston: Kluwer Academic Publishers, 2004.

[16] A. J. Bard and L. R. Faulkner, Electrochemical methods: Fundamentals and applications, John Wiley and Sons, 2001.

[17] B. L. Mordike and T. Ebert, "Magnesium; Properties — applications — potential," *Materials Science and Engineering: A.*, vol. 302, no. 1, pp. 37-45, 2001.

[18] G. Song, A. Atrens and D. StJohn, "A hydrogen evaluation method for the estimation of the corrosion rate of magnesium alloys," *Magnesium Technology,* pp. 254-262, 2011.

[19] A. Atrens, G. Song, F. Cao, Z. Shi and P. K. Bowen, "Advances in magnesium corrosion and research suggestions. Journal of magnesium and alloys," *Journal of Magnesium and Alloys,* vol. 1, pp. 177-200, 2013.

[20] R. Udhayan and D. Bhatt, "Corrosion of magnesium alloys in aqueous magnesium perchlorate battery electrolyte- a gasometry study," *Journal of Power Sources,* pp. 107-112, 1992.

[21] Z. Xiong, Y. Si, X. Feng and M. Li, "Investigation on the discharge behaviors of AZ31 and AZ61 magnesium alloys as anode material of metal-air fuel cells," *Advanced Materials Research,* vol. 1051, pp. 211-214, 2014.

[22] Z. Shi, M. Liu and A. Atrens, "Measurement of the corrosion rate of magnesium alloys using Tafel extrapolation," *Corrosion Science,* vol. 52, pp. 579-588, 2010.

[23] G. L. Song and A. Atrens, "Corrosion mechanisms of magnesium alloys," *Advanced Engineering Materials,* vol. 1, no. 1, pp. 11-33, 1999.

[24] M. Pourbaix, "Atlas of electrochemical equilibria in aqeous solutions," 1974.

[25] G. L. Song and A. Atrens, "Understanding magnesium corrosion- A framework for improved alloy performance," *Advanced Engineering Materials,* vol. 5, no. 12, pp. 837-858, 2003.

[26] G. L. Song, A. Atrens, D. StJohn, J. Nairn and Y. Li, "The electrochemical corrosion of pure magnesium in 1N NaCl," *Corrosion Science,* vol. 39, no. 5, pp. 855-875, 1997.

[27] ASM13C, "Corrosion: Environment and industries," ASM International, 2006.

[28] A. Pardo, M. Merino, A. Coy, F. Viejo, R. Arraba and S. F. Jr., "Influence of microstructure and composition on the corrosion behaviour of Mg/Al alloys in chloride media," *Electrochimica Acta,* vol. 53, no. 27, pp. 7890-7902, 2008.

[29] M. M. Avedesian and H. Baker, Magnesium and magnesium alloys, ASM International, 1999.

[30] P. Liang, T. Tarfa, J. Robinson, S. Wagner, P. Ochin, M. Harmelin, H. Seifert, H. Lukas and F. Aldinger, "Experimental investigation and thermodynamic calculation of the Al–Mg–Zn system," *Thermochimica Acta,* vol. 314, no. 1-2, pp. 87-110, 1998.

[31] G. Oktay and M. Urgen, "Corrosion behaviour of magnesium AZ31 sheet produced by twin roll casting," vol. 50, no. 5, pp. 380-389, 2015.

[32] A. McAlster and J. Murray, "Binary alloy phase diagrams," in *0-87170-381-5*, ASM Intenational, 1992, pp. 2.4-2.56.

[33] E. Ghali, Corrosion resistance of aluminum and magnesium alloys, John Wiley, 2010.

[34] R. C. Zeng, J. Zhang, W. J. Huang, W. Dietzel, K. U. Kainer, C. Blawert and K. E. Wei, "Review of studies on corrosion of magnesium alloys.," *Transactions of Nonferrous Metals Society of China*, vol. 16, pp. s763-s771, 2006.

[35] M. Gonzalez-Nunez, C. Nunez-Lopez, P. Skeldon, G. Thompson, H. Karimzadeh, P. Lyon and T. Wilks, "A non-chromate conversion coating for magnesium alloys and magnesium-based metal matrix composites," *Corrosion Science*, vol. 37, no. 11, pp. 1763-1772, 1995.

[36] L. Bland, A. King, N. Birbilis and J. Scully, "Assessing the corrosion of commercially pure magnesium and commercial AZ31B by electrochemical impedance, mass-loss, hydrogen collection, and inductively coupled plasma optical emission spectrometry solution analysis," *Corrosion*, vol. 71, no. 2, pp. 128-145, 2014.

[37] Z. Cano, M. Danaie, J. Kish, J. McDermid, G. Botton and G. Williams, "Physical characterization of cathodically-activated corrosion filaments on magnesium alloy AZ31B," *Corrosion*, vol. 71, no. 2, pp. 146-159, 2015.

[38] M. Montemor, A. Simoes and M. Carmezim, "Characterization of rare-earth conversion films formed on the AZ31 magnesium alloy and its relation with corrosion protection," *Applied Surface Science*, vol. 253, p. 6922–6931, 2007.

[39] G. B. Hamu, D. Eliezer and L. Wagner, "The relation between severe plastic deformation microstructure and corrosion behavior of AZ31 magnesium alloy," *Journal of Alloys and Compounds*, vol. 468, no. 1, pp. 222-229, 2009.

[40] S. Feliu Jr., M. C. Merino, R. Arrabal, A. E. Coy and E. Matykina, "XPS study of the effect of aluminium on the atmospheric corrosion of the AZ31 magnesium alloy," *Surface and Interface Analysis*, vol. 41, no. 3, pp. 143-150, 2009.

[41] X. Xia, X. Chen, W. Zhao, H. Xue, B. Liao, B. Hur and Z. Wang, "Corrosion behavior of closed-cell AZ31 Mg alloy foam in NaCl aqueous solutions," *Corrosion Science*, vol. 80, pp. 247-256, 2014.

[42] G. L. Song and Z. Xu, "The surface: Microstructure and corrosion of magnesium alloy AZ31 sheet," *Electrochimica Acta*, vol. 55, pp. 4148-4161, 2010.

[43] C. Bettles and M. Barnett, Advances in wrought magnesium alloys, Cambridge: Woodhead Publishing, 2012.

[44] A. Samaniego, I. Llorente and F. Jr. S., "Combined effect of composition and surface condition on corrosion behaviour of magnesium alloys AZ31 and AZ61," *Corrosion Science,* vol. 68, pp. 66-71, 2013.

[45] K. Reichek, K. Clark and J. Hillis, "Controlling the salt water corrosion performance of magnesium AZ91 alloy," *SAE Technical Paper 850417,* 1985.

[46] Y. Yang, F. Scenini and M. Curioni, "A study on magnesium corrosion by real-time imaging and electrochemical methods: relationship between local processes and hydrogen evolution," *Electrochimica Acta,* vol. 198, pp. 174-184, 2016.

[47] R. Zeng, W. Qi, H. Cui, F. Zhang, S. Li and E. Han, "In vitro corrosion of as-extruded Mg–Ca alloys—The influence of Ca concentration," *Corrosion Science,* vol. 96, pp. 23-31, 2015.

[48] J. Yang, J. Peng, E. A. Nyberg and F. Pan, "Effect of Ca addition on the corrosion behavior of Mg-Al-Mn alloy," *Applied Surface Science,* vol. 369, pp. 92-100, 2016.

[49] A. D. Südholza, N. T. Kirkland, R. G. Buchheit and N. Birbilis, "Electrochemical properties of intermetallic phases and common impurity elements in magnesium alloys," *Electrochemical Solid-State Letter,* vol. 14, no. 2, 2011.

[50] A. Pardo, M. Merino, A. Coy, R. Arrabal, F. Viejo and E. Matykina, "Corrosion behaviour of magnesium/aluminium alloys in 3.5 wt.% NaCl," *Corrosion Science,* vol. 50, pp. 823–834, 2008.

[51] G. Williams, H. L. Dafydd and R. Grace, "The localised corrosion of Mg alloy AZ31 in chloride containing electrolyte studied by a scanning vibrating electrode technique," *Electrochimica Acta,* vol. 109, no. 30, p. 489–501, 2013.

[52] O. Lunder, T. K. Aune and K. Nisancioglu, "Effect of Mn additions on the corrosion behavior of mould-cast magnesium ASTM AZ91," *Corrosion,* vol. 43, no. 5, pp. 291-295, 1987.

[53] H. Matsubara, Y. Ichige, K. Fujita, H. Nishiyama and K. Hodouchi, "Effect of impurity Fe on corrosion behavior of AM50 and AM60 magnesium alloys," *Corrosion Science,* vol. 66, pp. 203-210, 2013.

[54] ASM-13B, "Electrochemical series, Corrosion: Materials," ASM International, 2006.

[55] D. Thirumalaikumarasamy, K. Shanmugam and V. Balasubramanian, "Comparison of the corrosion behaviour of AZ31B magnesium alloy under immersion test and potentiodynamic polarization test in NaCl solution," *Journal of Magnesium and Alloys,* vol. 2, pp. 36-49, 2014.

[56] Metals Handbook Desk, "Metallographic practices generally applicable to all metals," ASM International, 1998.

[57] D. Williams and B. Carter, Transmission electron microscopy, Springer, 2009.

[58] A. Kaya, P. Uzan, D. Eliezer and E. Aghion, "Electron microscopical investigation of as-cast AZ91D alloy," *Material Science and Technology,* vol. 16, no. 9, pp. 1001-1006, 2013.

[59] Y. Wang, M.Xia, Z. Fan, X. Zhou and G. Thompson, "Effect of Al_8Mn_5 intermetallic particles on grain size of as-cast Mg-Al-Zn AZ91D alloy," *Intermetallics,* vol. 18, pp. 1683-1689, 2010.

[60] S. S. Park, Y. S. Oh, D. H. Kang and N. J. Kim, "Microstructural evolution in twin rolled strip cast Mg-Zn-Mn-Al alloy," *Material Science and Technology A,* Vols. 449-451, pp. 352-355, 2007.

[61] C. Xu, R. Wang, Y. Zhang and Y. Ding, "A general corrosion route to nanostructured metal oxides," *Nanoscale,* vol. 2, no. 6, pp. 906-909, 2010.

[62] V. Milinchuk, E. Klinshpont, V. Belozerov, I. Khavroshina and E. Sadikov, "The transformation of the oxide coatings of aluminum by imitation factors of nuclear power plants," *Nuclear Energy and Technology,* vol. 2, no. 3, pp. 209-213, 2016.

[63] S. I. Pun and S. M. Moon, "Corrosion mechanism of pure alumnium in alkaline solutions," *Journal of Solid State Electrochmistry,* vol. 4, no. 5, pp. 267-272, 2000.

[64] M. Danaie, R. M. Asmussen, P. Jakupi, D. W. Shoesmith and G. A. Botton, "The cathodic behaviour of Al–Mn precipitates during atmospheric and saline aqueous corrosion of a sand-cast AM50 alloy," *Corrosion Science,* vol. 83, pp. 299-309, 2014.

[65] S. Durdu and M. Usta, "Characterization and mechanical properties of coatings on magnesium by micro arc oxidation," *Applied Surface Science,* vol. 261, pp. 774–782, 2012.

[66] F. Chen, H. Zhou, B. Yao, Z. Qin and Q. Zhang, "Corrosion resistance property of the ceramic coating obtained through microarc oxidation on the AZ31 magnesium alloy surfaces," *Surface and Coatings Technology,* vol. 201, no. 9-11, pp. 774-782, 2007.

[67] Z. Huan, C. Xu, B. Ma, J. Zhou and J. Chang, "Substantial enhancement of corrosion resistance and bioactivity of magnesium by incorporating calcium silicate particles," *RSC advances,* vol. 6, no. 53, pp. 47897-47906, 2016.

[68] X. Yuan, C. Song, H. Wang and J. Zhang, Electrochemical impedance spectroscopy in PEM fuel cells: fundamentals and applications, Springer Science and Buisiness Media, 2009.

[69] Y. Yuan, J. Tu, H. Wu, C. Zhang, S. Wang and X. Zhao, "Influence of surface modification with Sn6O4(OH)4 on electrochemical performance of ZnO in Zn/Ni secondary cells," *Journal of Power Sources,* vol. 165, no. 2, pp. 905–910, 2007.

[70] X. Liu, J. Xiong, Y. Lv and Y. Zuo, "Study on corrosion electrochemical behavior of several different coating systems by EIS," *Progress in Organic Coatings,* vol. 64, no. 4, pp. 497–503, 2009.

[71] S. Gudić, I. Smoljko and M. Kliškić, "Electrochemical behaviour of aluminium alloys containing indium and tin in NaCl solution," *Materials Chemistry and Physics,* vol. 121, no. 3, pp. 561–566, 2010.

[72] Y. Tan, S. Bailey and B. Kinsella, "An investigation of the formation and destruction of corrosion inhibitor films using electrochemical impedance spectroscopy (EIS)," *Corrosion Science,* vol. 38, no. 9, pp. 1545-1561, 1996.

[73] "Capacitors and Dielectrics," [Online]. Available: http://mirror.mit-ocw.sbu.ac.ir/courses/physics/8-02sc-physics-ii-electricity-and-magnetism-fall-2010/capacitors-and-dielectrics/.

[74] K. Natori, D. Otani and N. Sano, "Thickness dependence of the effective dielectric constant in a thin film," *Applied Physics Letters,* vol. 73, no. 5, pp. 632-634, 1998.

[75] B. Hamah-Ali, B. S. Ali, R. Yusof and M. K. Aroua, "Corrosion of carbon steel in aqueous carbonated solution of MEA/ [bmim] [DCA]," *International Journal of Electrochemical Science.,* vol. 6, pp. 181-198, 2011.

Appendices

Appendix A: Corrosion Measurement Data for the Repeats of Polarization Test

The polarization tests were repeated to maintain statistical significance of data. The second repeat of Tafel polarization is included in figure A1.1. The corrosion potentials were similar in value as those obtained in the 1st set of experiments. Also, the results obtained from EIS analysis are included in Figure A1.2. and A1.3. The change in value of frequency at 0.01 was possibly due to formation of an unstable layer of corrosion products till a frequency of 0.1 was reached. After 0.1, the resistance value increased drastically possibly due to polarization of the material. The electrochemical parameters obtained from EIS analysis are included in Table A1.1. The values of electrical parameters obtained are similar as those obtained in 1st set of experiments. However, the value of R_s was considerably high in this case, this indicated a possibility of presence of a bubble in the electrolyte, which may have resulted in high resistance of the solution. This bubble could possibly be formed due to hydrogen evolution in the system. [10]

A1: 2nd Repeat of the electrochemical test

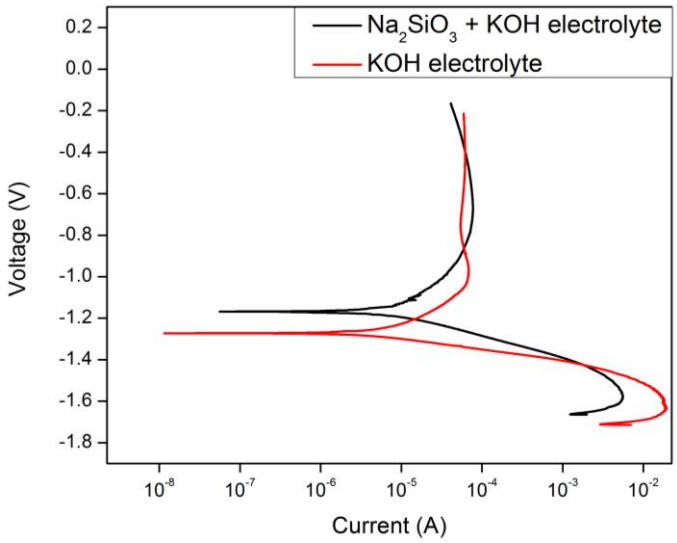

Figure A1.1 Tafel plots for Sample T (1) and Sample T (2).

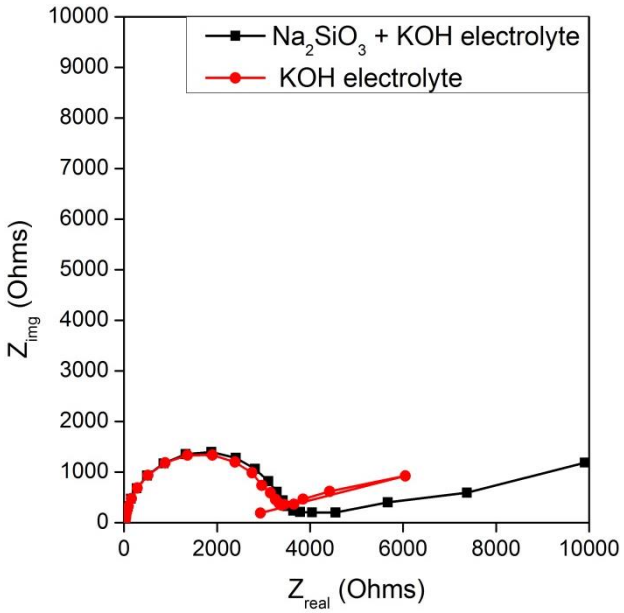

Figure A1.2 Nyquist plots for Sample E (1) and Sample E (2).

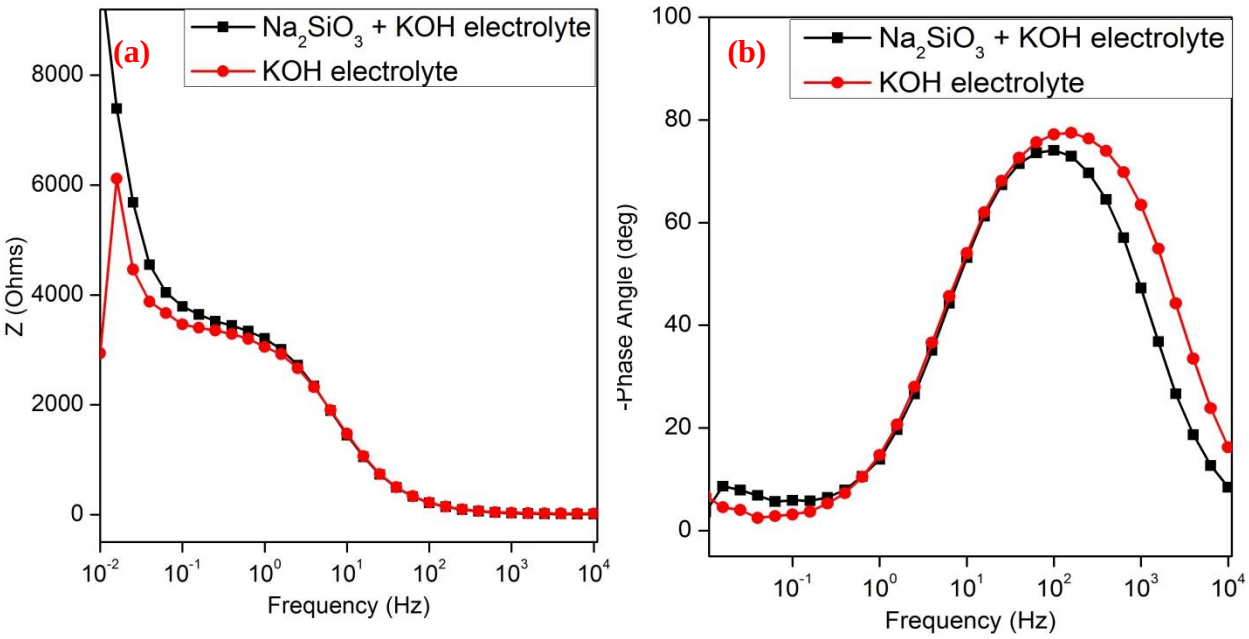

Figure A1.3 Bode (a) magnitude and; (b) phase plots for Sample E (1) and Sample E (2).

Table A1.1: Values of the electrical parameters of the curve-fitted EIS data (Repeat 2).

Material	R_s (Ω)	Q (μF)	R_c (kΩ)	W($m\Omega s^{-1/2}$)
Sample E (1)	1.97±0.41	6.80±0.32	2.31±0.15	1.70 ±0.41
Sample E (2)	1.78±0.09	7.15±0.26	2.93±0.12	11.40±2.46

**brackets represent error for individual parameters.*

Appendix B: Additional data from immersion tests

B1: Immersion test results

The weight loss of the corroded surface was measured using standard analytical balance. The loss in weight and the corresponding corrosion rates for the two different samples are included in Table B1.1. The density of the sample was measured to be 1.63g/cm^3.

Table B1.1: Corrosion rates obtained using immersion tests.

Electrolyte	Change in weight (g)	Corrosion rate (µm/y)
Electrolyte #1	0.0024	0.516
Electrolyte #2	0.0021	0.455

Although corrosion rate for sample immersed in Electrolyte #1 is greater than the sample immersed in Electrolyte #2, the value of corrosion rate obtained was considerably different from the ones obtained using Tafel extrapolation. This was possible because immersion tests give an approximation of long term effect of corrosion whereas electrochemical tests reveal information about the onset of corrosion. [25]

B2: Growth of corrosion products on surface of sample immersed in Electrolyte #1

In order to study the evolution of any surface films and corrosion products, immersion tests were performed for 3, 6, 9, 12, 15 and 18 days for the sample immersed in Electrolyte #1. A graph was made using Origin Pro 8.0 using data on composition of different elements in corrosion products from SEM-EDS analysis on the surface of the corroding sample. This enabled us to understand the variation of elements in the corrosion products during a 20 day immersion period. Since the corrosion products were predominantly composed of Ni rich layer in both samples, this test was

only performed for the Electrolyte #1 as the evolution of bulk corrosion products was expected to be similar in both cases. Also, differences in Si and Ca were too low to be detected accurately using SEM-EDS surface analysis.

The cross-section of the immersed samples was analyzed to examine the evolution of the corrosion products. As seen in Figure B2.1, after 3 days of immersion, a uniform and continuous surface layer ~3 µm thick was observed and its thickness increased by ~1µm / day until 9 days of immersion. Thereafter, an accelerated growth was observed (~ 2µm / day), with an evolution of cracks, voids and pores in the layer. These results correlate well with the observed stability and degradation of the Al-Mn precipitates. At 9 days, the fine (<10 µm) Al-Mn precipitates were seen to dissolve (or fall-out), contributing to the fragmentation of any protective surface film and resulting in its increased porosity and cracking. The resulting cracks enabled penetration of the Electrolyte #1 to the AZ31 substrate and its accelerated localized corrosion with undercutting of the surface layer thereafter, as seen in Figure B2.1 (12 days). Subsequently, continued immersion enabled rapid growth of the surface layer, reaching to over ~25 µm after 18 days.

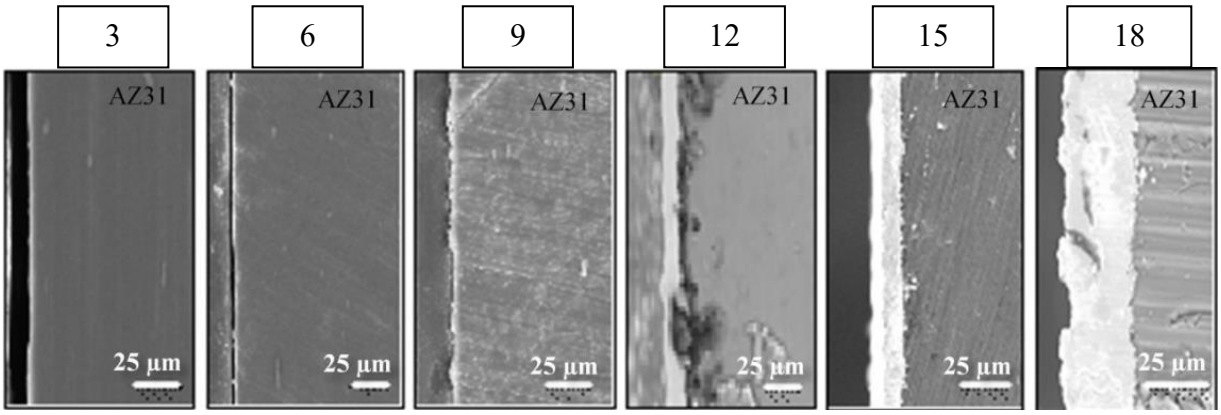

Figure B2.1: Cross-section of sample in Electrolyte #1 after immersion for 3, 6, 9, 12, 15 and 18 days.

Figure B2.2 shows the change in the concentration of different elements in the surface layer of sample immersed in Electrolyte #1 with respect to the immersion time. The solid state

diffusivity of Ni in Mg is low (Log D = -16m^2/sec at 740K). Therefore, the formation of the Ni-rich layer was likely the result of a preferential dissolution of the AZ31 matrix, leaving behind a surface layer enriched in Ni. After 3 days of immersion, the Mg content in the corrosion products was about 95at% whereas Ni was just 10at%. However, with continued immersion of the AZ31 sample in electrolyte, there was a gradual increase in Ni concentration in the corrosion products. After 18 days of immersion, the corrosion products were predominantly composed of Ni (~90 wt%). The Ni layer was observed to be highly porous, suggesting its formation was not exclusively driven by a transport of Ni from the substrate interior.

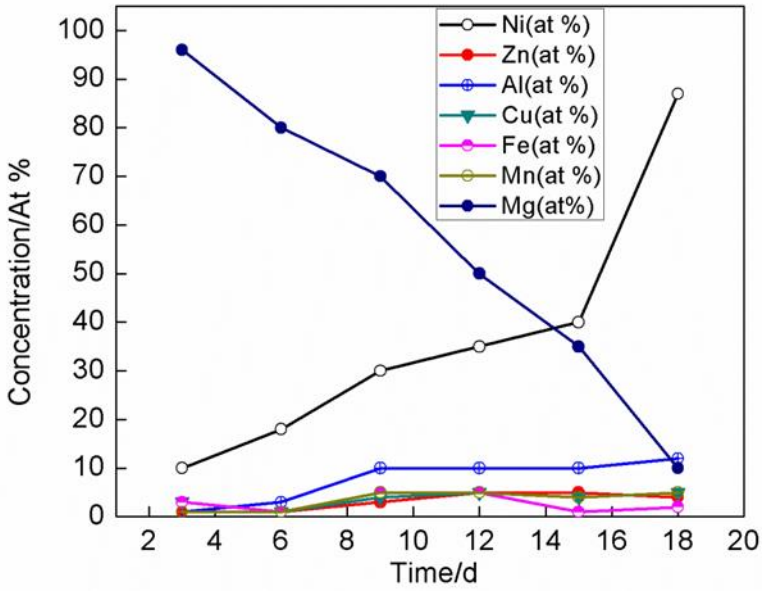

Figure B2.2: Growth of corrosion products on sample immersed in Electrolyte #1 obtained from SEM-EDS analysis.

Al content in the corrosion products also increased after immersion for 18days in Electrolyte #1. This most likely occurred due to its dissociation from the Al-Mn precipitate in the matrix due to corrosion. Therefore, diffusion of Al in the corrosion products resulted in the increase of Al content in it.